Electronic grain boundary properties in polycrystalline $Cu(In,Ga)Se_2$ semiconductors for thin film solar cells

Dissertation
zur Erlangung des akademischen Grades
Doktor der Naturwissenschaften
(Dr. rer. nat.)

von
Robert Baier

eingereicht im Fachbereich Physik der
Freien Universität Berlin

angefertigt am
Helmholtz-Zentrum Berlin für Materialien und Energie,
Institut für heterogene Materialsysteme

Mai 2012

Arbeit eingereicht am: 09.05.2012
Tag der Disputation: 25.06.2012
1. Gutachter: Prof. Dr. Martha Ch. Lux-Steiner
2. Gutachter: Prof. Dr. Jose Ignacio Pascual

Zusammenfassung

Auf polykristallinen Cu(In,Ga)Se_2 (CIGSe) Dünnschichten basierende Solarzellen erreichen den höchsten Wirkungsgrad aller Dünnschichtsollarzellen [1]. Dieser Rekordwirkungsgrad wird, zumindest teilweise, gutartigen Korngrenzeneigenschaften in CIGSe Dünnschichten zugeschrieben. Die physikalischen Grundlagen dieses Phänomens sind jedoch, trotzt großer Anstrengungen, nicht ausreichend verstanden.
Im Rahmen dieser Arbeit wurden die elektronischen Eigenschaften der Korngrenzen in CIGSe Dünnschichten eingehend untersucht. Mittels Kelvinsondenkraftmikroskopie (KPFM) wurden die elektronischen Eigenschaften der Korngrenzen in Abhängigkeit des Ga-Gehalts ausgewertet. Fünf CIGSe Dünnschichten mit unterschiedlichem Ga-Gehalt wurden mittels ähnlicher Dreistufenkoverdampfungsprozesse hergestellt. Unbehandelte als auch chemisch behandelte (KCN-geätzte) CIGSe Dünnschichten wurden analysiert. Die chemische Behandlung diente hierbei der Entfernung von Oberflächenoxiden. Kein Unterschied in den elektronischen Korngrenzeneigenschaften vor und nach der chemischen Behandlung wurde festgestellt, weswegen geschlussfolgert wird dass eine moderate Oberflächenoxidation[1] die elektronischen Eigenschaften der Korngrenzen nicht verändert. Insgesamt wurden deutliche Schwankungen der elektronischen Potentialbarrieren an Korngrenzen beobachtet. Unter Berücksichtigung des Mittelungseffekts der Austrittsarbeit, welcher an Potentialschwankungen im Nanometerbereich in KPFM-Messungen auftritt und welcher im Rahmen dieser Arbeit quantifiziert wurde, wurden sowohl positive als auch negative Barrieren zwischen ≈ -350mV und $\approx +450$mV aufgefunden. Zusätzlich wurden Variationen der Defektdichte an Korngrenzen zwischen $\approx 3.1 \times 10^{11}$cm^{-2} und $\approx 2.1 \times 10^{12}$cm^{-2} detektiert. Es wurde kein Zusammenhang zwischen den elektronischen Eigenschaften der Korngrenzen und dem Ga-Gehalt festgestellt. Somit ist es nicht möglich, den Abfall der Solarzelleneffizienz, welcher für CIGSe Dünnschichtsolarzellen mit hohem Ga-Gehalt beobachtet wird, auf eine Veränderung der elektronischen Korngrenzeneigenschaften zurückzuführen.
KPFM und Rückstreuelektronenbeugung wurden erstmalig kombiniert, um sich ergänzende Informationen über strukturelle und elektronische Eigenschaften einzelner Korngrenzen in CIGSe Dünnschichten zu gewinnen. Mittels dieser Informationen konnte der Zusammenhang zwischen Symmetrie und Potentialbarriere von Korngrenzen untersucht werden. Es wurde gezeigt, dass hochsymmetrische $\Sigma 3$ Korngrenzen mit geringerer Wahrscheinlichkeit eine Potentialbarriere besitzen als niedersymmetrische nicht-$\Sigma 3$ Korngrenzen. Die Annahme einer allgemeinen Symmetrieabhängigkeit der elektronischen Korngrenzeneigenschaften, d.h. ein Zusammenhang zwischen der Symmetrie einer Korngrenze und der dazugehörigen Potentialbarriere, welcher auch für niedrigsymmetrische Korngrenzen gültig ist, könnte helfen, die großen Schwankungen der Potentialbarrieren an Korngrenzen in polykristallinem CIGSe zu erklären.

[1]Expositionszeit der Dünnschichten in Umgebungsluft $<\approx 24$h.

Abstract

Solar cells based on polycrystalline $Cu(In,Ga)Se_2$ (CIGSe) thin film absorbers reach the highest energy conversion efficiency among all thin film solar cells [1]. The record efficiency is at least partly attributed to benign electronic properties of grain boundaries (GBs) in the CIGSe layers. However, despite a high amount of research on this phenomenon the underlying physics is not sufficiently understood.
This thesis presents an elaborate study on the electronic properties of GBs in CIGSe thin films. Kelvin probe force microscopy (KPFM) was employed to investigate the electronic properties of GBs in dependence of the Ga-content. Five CIGSe thin films with various Ga-contents were grown by means of similar three stage co-evaporation processes. Both *as grown* as well as *chemically treated* (KCN etched) thin films were analyzed. The chemical treatment was employed to remove surface oxides. No difference in electronic GB properties was found with or without the chemical treatment. Therefore, we conclude that a moderate surface oxidation[2] does not alter the electronic properties of GBs. In general, one can observe significant variations of electronic potential barriers at GBs. Under consideration of the averaging effect of the work function signal of nanoscale potential distributions in KPFM measurements which was quantified in the course of this thesis both positive and negative potential barriers in a range between ≈ -350mV and $\approx +450$mV were detected. Additionally, variations in the defect densities at GBs between $\approx 3.1 \times 10^{11}\text{cm}^{-2}$ and $\approx 2.1 \times 10^{12}\text{cm}^{-2}$ were found. However, no correlation between the electronic properties of GBs and the Ga-content of CIGSe thin films was discovered. Consequently, one cannot explain the drop in device efficiency observed for CIGSe thin film solar cells with a high Ga-content by a change of the electronic properties of GBs.
Combined KPFM and electron backscatter diffraction measurements were employed for the first time on CIGSe thin films to gather complementary information about both the structural and electronic properties of individual GBs. With the help of this information it was possible to investigate the interrelationship between the symmetry and the electronic potential barrier of GBs. We could reveal that highly symmetric $\Sigma 3$ GBs have a lower probability to possess a charged potential barrier than lower symmetric non-$\Sigma 3$ GBs. The assumption of a general symmetry-dependence of the electronic properties of GBs in CIGSe, i.e. a correlation between the particular symmetry of a GB and its potential barrier that is also valid for GBs with symmetries lower than $\Sigma 3$, could help to explain the large variations of potential barriers observed at GBs in polycrystalline CIGSe thin films.

[2]Exposure time of the thin films to ambient air $<\approx 24$h.

Contents

Zusammenfassung iii

Abstract v

1 Introduction 1

2 The material system of $Cu(In,Ga)Se_2$ 5
2.1 Material and interface properties of $Cu(In,Ga)Se_2$ . . . 5
2.1.1 Structural properties . . . 5
2.1.2 Electronic properties . . . 6
2.1.3 Surface properties . . . 8
2.2 $Cu(In,Ga)Se_2$ for thin film solar cells . . . 9
2.2.1 $Cu(In,Ga)Se_2$ thin film solar cells . . . 9
2.2.2 Fabrication of $Cu(In,Ga)Se_2$ thin films . . . 11
2.2.3 Chemical surface conditioning . . . 13

3 Grain boundaries in $Cu(In,Ga)Se_2$ 15
3.1 General properties of grain boundaries . . . 15
3.2 Electronic properties of grain boundaries in $Cu(In,Ga)Se_2$ . . . 17
3.2.1 Various models of the electronic properties of grain boundaries . . . 17
3.2.2 Status quo of grain boundary research . . . 22

4 Experimental methods of characterization 25
4.1 Kelvin probe force microscopy (KPFM) . . . 25
4.1.1 Atomic Force Microscopy (AFM) . . . 25
4.1.2 From AFM to KPFM . . . 28
4.1.3 Experimental details . . . 32
4.1.4 Simulation of the tip-sample interaction in KPFM . . . 35
4.2 Scanning electron microscopy (SEM) . . . 37
4.2.1 SEM topography imaging . . . 37
4.2.2 Electron backscatter diffraction (EBSD) . . . 38

5 Kelvin probe force microscopy at nanoscale potential distributions (NPDs) 41
5.1 Kelvin probe force spectroscopy (KPFS) . . . 43
5.1.1 KPFS experiments at nanoscale potential distributions . . . 44
5.1.2 KPFS simulations at nanoscale potential distributions . . . 49
5.2 The impact of electronic inhomogeneities on KPFS experiments . . . 50

5.3 The averaging effect at nanoscale potential distributions . . . 53
5.3.1 The influence of tip geometry . . . 53
5.3.2 The influence of NPD width . . . 54
5.3.3 The influence of tip-sample distance . . . 56
5.3.4 The influence of surface topography . . . 58
5.4 Conclusions . . . 60

6 Electronic grain boundary properties in Cu(In,Ga)Se_2 with various Ga-contents 61
6.1 Cu(In,Ga)Se_2 thin films with various Ga-contents . . . 63
6.2 Topography-based localization of grain boundaries . . . 68
6.3 Analysis of electronic grain boundary properties . . . 69
6.4 Electronic potential barriers at grain boundaries . . . 71
6.4.1 The influence of surface condition . . . 71
6.4.2 Absolute dimensions of the potential barriers . . . 73
6.4.3 Doping densities and defect densities . . . 75
6.4.4 Potential barriers at grain boundaries and solar cell performance . . . 78
6.5 Conclusions . . . 80

7 Symmetry-dependence of electronic grain boundary properties in Cu(In,Ga)Se_2 81
7.1 Complementary information about structural and electronic properties . . . 82
7.2 The localization of grain boundaries in Kelvin probe force microscopy . . . 84
7.3 Electronic potential barriers at grain boundaries . . . 87
7.4 Conclusions . . . 89

8 Conclusions 91

A Appendix 93
A.1 KPFM and KPFS at NPDs: A comparison of methods . . . 93
A.2 KPFS experimental parameters . . . 96
A.3 KPFS simulation parameters . . . 97
A.4 NPD width dependent averaging in KPFM: Fit function . . . 97
A.5 Measurement inaccuracy in the determination of potential barriers . . . 98
A.6 Localization of an identical surface position in KPFM and the SEM . . . 100

List of acronyms and abbreviations 103

Bibliography 107

List of publications and conferences 117

Curriculum vitae 121

Acknowledgments 123

Erklärung 125

Chapter 1

Introduction

Quotes of Dr. Angela Merkel:

- **27.11.2006:** *"Ich werde es immer für unsinnig halten, technisch sichere Kernkraftwerke, die kein CO_2 emittieren, abzuschalten."*

  "I will always consider it nonsensical to shut down technically safe nuclear power plants which do not emit any CO_2."

- **15.6.2009:** *"Wenn ich sehe, wie viele Kernkraftwerke weltweit gebaut werden, dann wäre es wirklich jammerschade, sollten wir aus diesem Bereich aussteigen."*

  "If I look at how many nuclear power plants are being built worldwide, it would be a great pity if we were to opt out of this area"

- **14.3.2011:** *"Wenn wir von der Kernenergie als Brückentechnologie sprechen, dann bedeutet das nichts anderes, als dass wir aus der Nutzung der Kernenergie aussteigen möchten."*

  "If we talk about nuclear power as a bridging technology, this means nothing other than that we want to opt out of the use of nuclear power."

- **9.6.2011** *"In Fukushima haben wir zur Kenntnis nehmen müssen, dass selbst in einem Hochtechnologieland wie Japan die Risiken der Kernenergie nicht sicher beherrscht werden können."* Zur Energiewende: *"Für dieses gemeinsame Projekt werbe ich mit aller Kraft und mit aller Überzeugung."*

  "With Fukushima we had to take note of the fact that, even in a high-tech country like Japan, the risks of nuclear energy are not controllable." Referring to the energy change: *"I promote this collective project with all my power and belief."*

The above quotes [2, 3] of the German Federal Chancellor demonstrate how the German energy politics have changed within the last year. Triggered by the Fukushima nuclear disaster (11.3.2012), for the first time in the history of the Federal Republic of Germany there is a vast consensus across all major political parties that the energy change, i.e. the transition of the energy supply from fossil fuels to green fuels, is one of the major challenges facing German energy politics.

In the *"Energiekonzept 2050"* the Renewable Energy Research Association[1], encouraged by the German Federal Government, presented an energy strategy for the year 2050, based on the exclusive use of renewable energies [4]. According to the *Energiekonzept 2050*, the future generation of electricity lies with wind energy and photovoltaics. One major challenge is to reduce the costs of green electricity to a level comparable to that of fossil electricity (i.e. electricity generated by nuclear and coal-burning power plants). To achieve this goal, it is necessary to both develop cheaper methods of manufacturing and increase the efficiency of used technologies (in particular of photovoltaics).

One promising approach that can help to reduce the costs of photovoltaic energy is the so called "thin film" photovoltaics. In contrast to wafer-based solar cells, which are the most common solar cells as of now, thin film solar cells do not depend on high purity absorber materials, whose production requires a high energy input. Rather, it is possible to produce thin film absorber materials by means of quick and energy-saving deposition techniques. Additionally, thin film absorbers are about a hundred times thinner than wafer-based photovoltaic absorbers. This allows for a further reduction of production costs.
The thin film technology that reaches the highest energy conversion efficiency is based on polycrystalline $Cu(In,Ga)Se_2$ (CIGSe) absorber layers [5]. On a laboratory scale CIGSe thin film solar cells reach efficiencies beyond 20% [1]. Industrially produced CIGSe solar cells achieve module efficiencies above 15% [1, 6]. These record efficiencies are at least partly attributed to benign electronic properties of grain boundaries (GBs) in the polycrystalline CIGSe layers. In general, GBs are regarded as detrimental for solar cell performance, as they exhibit a high density of both structural and electronic defects, and can act as recombination centers [7, 8]. Nevertheless, CIGSe thin film solar cells outperform their monocrystalline counterparts[2].
Despite a high amount of research on this phenomenon the physical fundamentals underlying the electronic properties of GBs in CIGSe remain at the heart of controversial discussions [9–14]. Understanding the GB properties is regarded as a means to increasing the efficiency of CIGSe thin film solar cells.

This thesis presents a detailed investigation on the electronic properties of GBs in CIGSe thin films. Kelvin probe force microscopy (KPFM) is mainly employed to gather spatially resolved information about individual GBs on a microscopic scale. One focus of this work is on understanding the effect of the Ga-content of CIGSe thin films on the electronic properties of GBs. A second emphasis is on understanding the correlation between the symmetry and the electronic properties of GBs.

The thesis is outlined as follows:

- **Chapter 2** provides a general overview of the material system of GIGSe, and gives an introduction to the concept of thin film solar cells based on polycrystalline CIGSe absorber layers.

- **Chapter 3** deals particularly with the properties of GBs. The concept of the coincidence site lattice is introduced, which allows for a classification of GBs based

[1] ForschungsVerbund Erneuerbare Energien (FVEE); *www.fvee.de.*

[2] It should be noted that the development of monocrystalline CIGSe solar cells is not carried out with high efforts, due to a lack of industrial interest in monocrystalline CIGSe solar cell devices.

on their symmetry. Subsequently, the chapter summarizes the most prominent models to explain the benign behavior of GBs in CIGSe, and gives an overview of previous investigations dealing with the issue of GBs in CIGSe.

- **Chapter 4** introduces the experimental methods applied in the framework of this thesis in detail. The chapter begins with an explanation of the principle of KPFM, going on to discuss two different experimental methods based on scanning electron microscopy (SEM), SEM topography imaging and electron backscatter diffraction (EBSD).
- **Chapter 5** deals with KPFM experiments at nanoscale potential distributions (e.g. grain boundaries). It demonstrates how quantitative information about potential variations on a nanometer scale can be gathered based on KPFM measurements.
- **Chapter 6** investigates the electronic properties of GBs in CIGSe thin films in dependence of the Ga-content. It reveals that one cannot explain the drop in device efficiency observed for CIGSe thin film solar cells with a high Ga-content by a change of the electronic properties of GBs.
- **Chapter 7** deals with combined measurements of the structural and electronic properties of individual GBs in CIGSe thin films. By means of complementary KPFM and EBSD experiments it will disclose a correlation between the symmetry and the potential barrier of GBs.
- **Chapter 8** provides a summary of the results obtained in this thesis.

Chapter 2

The material system of Cu(In,Ga)Se_2

This chapter provides an overview of the material system of Cu(In,Ga)Se_2 (GIGSe). It begins with an introduction of the structural and electronic properties. The particular characteristics of the CIGSe surface are emphasized as well. Subsequently, the chapter will discuss the concept of thin film solar cells based on polycrystalline CIGSe absorber layers, and the fabrication process of such absorbers. Additionally, it will look at a method of chemical surface conditioning to remove oxides from CIGSe thin films.

2.1 Material and interface properties of Cu(In,Ga)Se_2

Cu(In,Ga)Se_2 (CIGSe) is a quaternary compound semiconductor which belongs to the family of the I-III-VI_2 chalcopyrites [15]. It can be obtained by intermixing the ternary compounds of $CuInSe_2$ and $CuGaSe_2$. To indicate the ratio of group-III elements (In, Ga) in the CIGSe compound the notion $CuIn_{1-x}Ga_xSe_2$ is common, where x = Ga/(In+Ga) represents the Ga-content of the material.

2.1.1 Structural properties

Cu(In,Ga)Se_2 (CIGSe) crystallizes in a tetragonal chalcopyrite space lattice (space group: $I\bar{4}2d$), as illustrated in Fig. 2.1 (a). Its lattice structure can be derived from the cubic lattice structure of the group-IV semiconductors by substitution of elements so as to maintain the electron-to-atom ratio[1] equal to 4 (see Fig. 2.1 (b)). Each group-I and group-III atom is coordinated to 4 group-VI atoms in a tetrahedral way, while each group-VI atom is coordinated to two Group-I atoms and and two group-III atoms in a tetrahedral, ordered manner. The tetrahedral coordination implies a primarily covalent bonding with prevailing sp^3 hybridization. However, some ionic bonding character is present as well [15]. Therefore, the group-I and group-III metals are frequently denoted as cations, whereas the group-VI Se atoms are denoted as anions.

[1]The Grimm-Sommerfeld rule states that chemical compounds which mainly exhibit covalent bonding have similar optoelectronic properties, if the average electron-to-atom ratio is maintained.

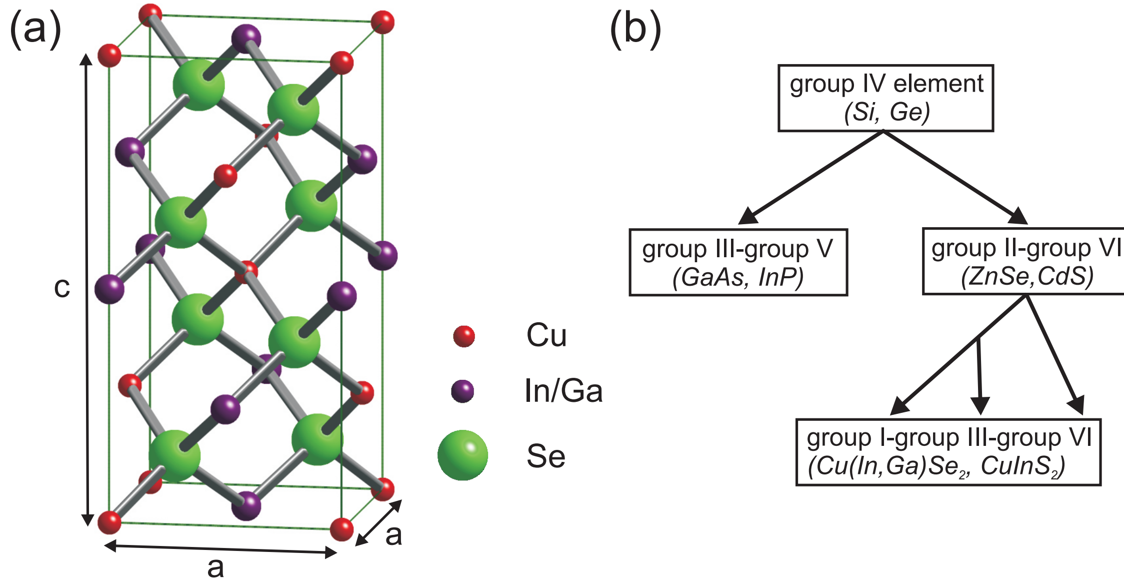

Figure 2.1: *(a) Unit cell of the CIGSe space lattice (from [18]). The lattice constants a and c of the unit cell are indicated by black arrows. (b) The lattice structure of CIGSe can be derived from the cubic lattice structure of the group-IV semiconductors with the help of the Grimm-Sommerfeld rule.*

Due to the ordered presence of both the group-I and group-III cations, the CIGSe space lattice represents a superlattice of the zinkblende structure with a unit cell volume about twice the size of the zincblende structure. The different bonding lengths between the various cations and anions cause a tetragonal distortion of the lattice structure [15, 16]. The quantity $2 - c/a$ is a measure of its magnitude, where 2 represents the ratio of the lattice constants a and c in case of the undisturbed crystal structure. The tetragonal distortion linearly depends on the Ga-content x, whereat c/a is larger than 2 for $x < 0.23$ and smaller than 2 for $x > 0.23$ [17]. As it is discussed in more detail in Sec. 6.1, the tetragonal distortion affects the grain size in polycrystalline CIGSe thin films.

2.1.2 Electronic properties

Band gap energy

$Cu(In,Ga)Se_2$ (CIGSe) is a semiconductor with a direct band gap at the high symmetry (Γ_{hs})-point [19–21]. The relatively low band gap energy of CIGSe compared to the analog II-VI semiconductors (see Fig. 2.1 (b))[2] results from a hybridization of Cu d-orbitals and Se p-orbitals in the valence band [15, 22–24].

Due to the interaction with the crystal-field and spin-orbit coupling, the valance band is split up into three energetic levels [15, 25, 26]. The transition energy from the highest valence band level to the conduction band minimum is referred to as band gap energy E_G

[2]The band gap of I-III-VI semiconductors is up to 1.6eV smaller than that of the II-VI analogs [15]. This is unusual considering the Grimm-Sommerfeld rule.

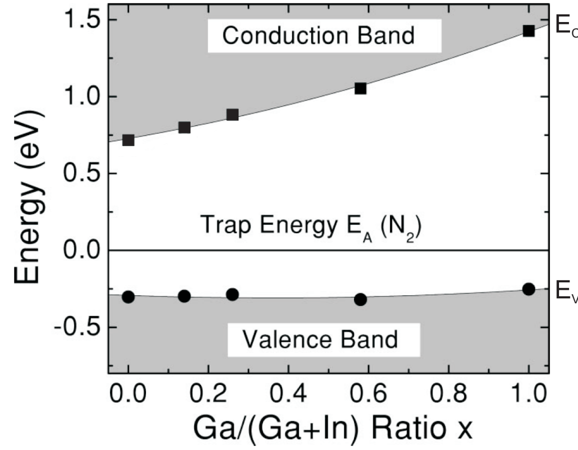

Figure 2.2: *Valence band energy E_V and conduction band energy E_C of CIGSe in dependence of the Ga-content x. The energy level of a bulk acceptor state (N_2) which has a constant energy with respect to the vacuum level is used as energetic reference level. From [30].*

in the following. The optical band gap energy of $CuInSe_2$ is $\approx$ 1.04eV [15]. By means of a gradual substitution of In atoms with Ga atoms the band gap can be increased to up to $\approx$ 1.68eV, which is the optical band gap energy of $CuGaSe_2$ [15]. The band gap energies of the quaternary $CuIn_{1-x}Ga_xSe_2$ compounds can be calculated with the help of an empirical “bowing equation” [27, 28]:

$$E_G(x) = (1-x)E_G(CuInSe_2) + xE_G(CuGaSe_2) - bx(1-x), \tag{2.1}$$

where $b = 0.15 - 0.24$ [27, 29] is the so called “optical bowing coefficient”.

The increase in band gap energy from $CuInSe_2$ to $CuGaSe_2$ mainly originates from an increase of the energy position of the conduction band minimum E_C with increasing Ga-content x. In contrast, the energy position of the valance band maximum E_V stays almost constant with increasing Ga-content, due to the fact that it is mainly governed by Cu d orbitals and Se p orbitals [27, 28].
In Fig. 2.2 the valence band energy E_V and the conduction band energy E_C are depicted in dependence of the Ga-content x. Turcu et al. [30] used the energy level of a bulk acceptor state which has a constant energy with respect to the vacuum level as energy reference.

Intrinsic Defects

$Cu(In,Ga)Se_2$ (CIGSe) is typically a p-type semiconductor with free hole densities in the range of $\approx 10^{16}\text{cm}^{-3} - 10^{18}\text{cm}^{-3}$ at room temperature [15, 31–33]. The doping is governed by intrinsic defects. In Tab. 2.1 an overview of the point defects that appear in CIGSe is displayed. As can be noticed, Cu vacancies (V_{Cu}) have the smallest formation energy of all point defects. Consequently, they are the dominant defect in CIGSe; their acceptor-like nature is the reason for the p-type character of CIGSe.

Table 2.1: *The twelve possible point defects in the ternary compounds $CuInSe_2$ and $CuGaSe_2$. The type indicates the electronic character of a defect (A=acceptor, D=donor). The typical formation enthalpies ΔH of the neutral defects were obtained from: [a] [28], [b] [34], [c] [35], [d] [36].*

Point defect	Vacancy			Interstitial			Antisite					
Notion	V_{Cu}	V_{III}	V_{Se}	Cu_i	III_i	Se_i	Cu_{III}	III_{Cu}	Cu_{Se}	Se_{Cu}	III_{Se}	Se_{III}
Type	A	A	D	D	D	A	A	D	A	D	A	D
$\mathbf{\Delta H}^{CISe}$ [eV]	0.60^a	3.04^a	3.00^b	2.88^a	9.1^d	22.4^d	1.54^a	3.34^a	5.4^c	6.0^c	5.0^c	5.2^c
$\mathbf{\Delta H}^{CGSe}$ [eV]	0.66^a	2.83^a	xxx	3.38^a	xxx	xxx	1.41^a	4.22^a	xxx	xxx	xxx	xxx

One distinct feature of Cu vacancies is the decrease of their formation enthalpy with increasing Fermi energy E_F. If the Fermi level is at a position roughly at mid-band gap, the formation energy of V_{Cu} even becomes negative, and Cu vacancies emerge spontaneously [37, 38]. This compensation mechanism significantly complicates n-type doping of CIGSe semiconductors, and even prohibits it for high Ga-contents [39, 40]. With respect to solar cell production this finding implicates that it is almost impossible to build solar cells based on a CIGSe homojunction.

2.1.3 Surface properties

The electronic properties of surfaces are generally different from the electronic properties of the bulk of a material. This results from the fact that the periodicity of the bulk crystal structure is interrupted at a surface. To minimize the free energy a variety of effects, for example dangling bonds and reconstructions, can emerge on a surface.

For zincblende semiconductors non-polar surfaces, i.e. surfaces with an identical number of cations and anions, are energetically most favorable and emerge in thermodynamic equilibrium (e.g. the (110) surface for GaAs). The charge neutralization of polar surfaces via the creation of surface reconstructions is energetically costly [41].
In contrast, it was observed that Cu(In,Ga)Se_2 (CIGSe) surfaces spontaneously facet into (112)-cation plus $(\overline{112})$-anion terminated polar surface orientations, even if grown epitaxially on non-polar GaAs(110) substrates [42]. The charge neutrality of the polar surface facets is obtained via the formation of reconstruction patterns including Cu vacancy rows (cation terminated (112) facet) and III-on-Cu antisites (anion terminated $(\overline{112})$ facet) [41, 43, 44]. The formation of polar surface facets is energetically more favorable for CIGSe than a non-polar surfaces configuration, due to the low formation energy of Cu vacancies V_{Cu} (see Tab. 2.1).

Various facet orientations (especially (112) and $(\overline{112})$) can be found on the surface of CIGSe thin films. They all exhibit different electronic properties. In particular, each facet orientation possesses a distinct work function value, due to a specific surface dipole characteristics [43]. For example, the work function of anion-terminated $(\overline{112})$ facets was found to be about 200meV higher than that of cation-terminated (112) facets in Kelvin probe force microscopy experiments, as can be seen in Fig. 2.3 [45]. The reason for this is the higher Pauling electronegativity of anions in comparison to cations.

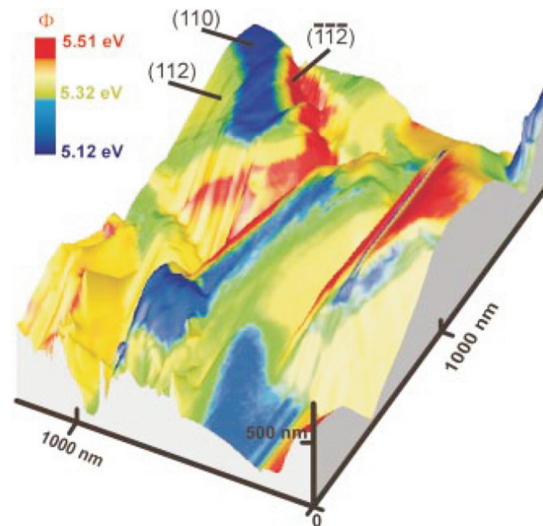

Figure 2.3: *Kelvin probe force microscopy (see Sec. 4.1) image of a $CuGaSe_2$ thin film grown on a Mo/glass substrate. The three dimensional image merges the surface topography (as 3D effect) and the work function (as color scale). The orientations of various surface facets are indicated in the image. From [45].*

2.2 Cu(In,Ga)Se_2 for thin film solar cells

The direct band gap, the adjustable band gap energy E_G between 1.0eV and 1.7eV (see Sec. 2.1.2), and the high optical absorption (α >10^5cm^{-1}, [46]) make polycrystalline Cu(In,Ga)Se_2 (CIGSe) a popular material used as absorber layer in thin film solar cells. In fact, thin film solar cells based on CIGSe absorber layers reach the highest energy conversion efficiencies of all thin film devices [5]. At a laboratory scale record efficiencies above 20% have been achieved [1].

This section introduces the concept of solar cells based on CIGSe absorbers employed at the Helmholtz Zentrum Berlin. It additionally presents experimental results of a chemical conditioning of CIGSe surfaces.

2.2.1 Cu(In,Ga)Se_2 thin film solar cells

Fig. 2.4 (a) shows a schematic of a thin film solar cell based on a Cu(In,Ga)Se_2 (CIGSe) absorber layer ("CIGSe solar cell"). The typical manufacturing process of such a solar cell is as follows. On top of an about 2mm thick soda-lime glass substrate a molybdenum back contact of about 500nm thickness is deposited by means of sputter deposition. The p-type CIGSe absorber layer is deposited on top of the back contact by means of a complex physical vapor deposition co-evaporation process (see Sec. 2.2.2). Its thickness of about 2μm is about a hundred times thinner than the light absorbing material in solar cells based on crystalline silicon; this is why CIGSe solar cells are referred to as "thin film solar cells". In the scanning electron micrograph in Fig. 2.4 (b) one can clearly recognize the granular structure of the polycrystalline CIGSe material. The average grain size of about 1μm (see Fig. 6.4 (a)) is smaller than the thickness of the CIGSe layer. It is believed

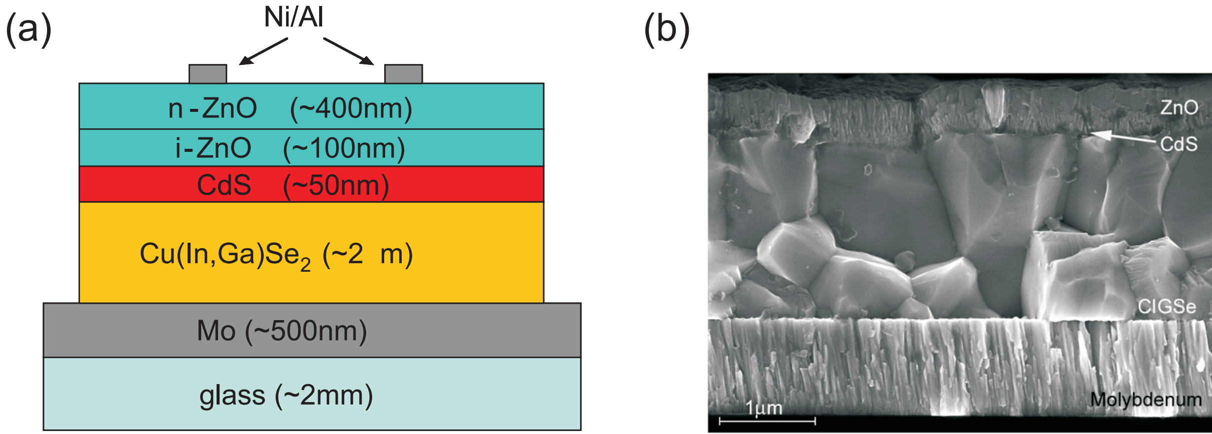

Figure 2.4: *(a) Schematic and (b) scanning electron micrograph of the cross section (from [47]) of a CIGSe thin film solar cell. The stack consists of a soda-lime glass substrate, a molybdenum back contact, a p-type CIGSe absorber layer, a n-type CdS buffer layer, an i-ZnO/n-ZnO:Al double window layer, and Ni/Al front contacts.*

that the grain boundaries in CIGSe possess special electronic properties that allow for the excellent efficiencies of CIGSe solar cells (see Chap. 3). On top of the CIGSe layer a thin n-type CdS buffer layer ($\approx$ 50nm) is deposited by means of chemical bath deposition. Its main function is to passivate interface defects and to provide a good band alignment within the solar cell. It is argued that an interdiffusion of Cd atoms from the buffer layer to the CIGSe absorber causes a type inversion on the surface of the latter [42, 44]. A ZnO double window layer consisting of an about 400nm thick layer of n-type ZnO:Al on top of an about 100nm thick layer of intrinsic ZnO is sputter-deposited on top of the buffer layer. It forms the heterojunction together with the p-type absorber layer. A Ni/Al grid is mounted on top of the window layer and serves as front contact of the CIGSe solar cell.

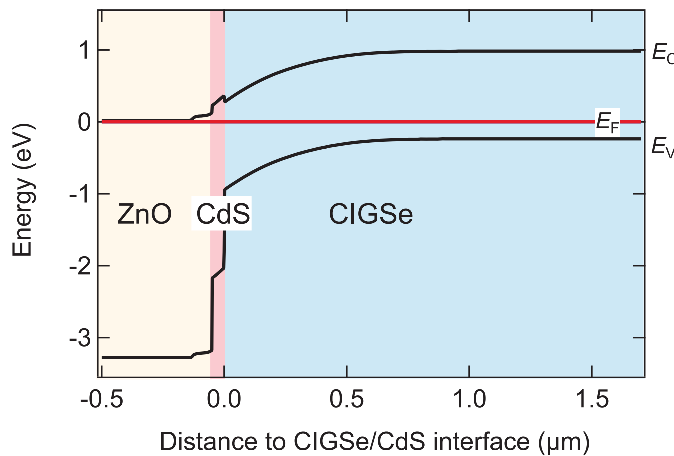

Figure 2.5: *Schematic of the electronic band diagram of a $CuIn_{0.67}Ga_{0.33}Se_2$ thin film solar cell including the valence band maximum E_V, the Fermi energy E_F, and the conduction band minimum E_C. Used band gap energies: E_G(ZnO)=3.3eV, E_G(CdS)=2.4eV, E_G(CIGSe)=1.22eV. From [48].*

Fig. 2.5 shows a schematic band diagram of a CIGSe solar cell. Both the ZnO window layer and the CdS buffer layer exhibit rather large band gap energies of ≈3.3eV and 2.4eV, respectively. Most of the light which shines on the CIGSe solar cell is therefore transmitted to the CIGSe layer, where it is absorbed via the excitation of electron-hole pairs. Due to the lower doping density of the *p*-type absorber layer compared to the *n*-type window layer, the space charge region mostly extends into the absorber, where it supports the charge separation of the electron hole pairs.

2.2.2 Fabrication of $Cu(In,Ga)Se_2$ thin films

Phase diagram

In order to be able to fabricate $Cu(In,Ga)Se_2$ (CIGSe) thin films, detailed knowledge about the growth mechanisms of the material is required. In Fig. 2.6 the equilibrium phase diagram of $CuInSe_2$ along the pseudo-binary cut $In_2Se_3-Cu_2Se$ is displayed between 15 at.% and 30 at.% Cu. Although the growth process is not an equilibrium process, the equilibrium phase diagram can provide valuable information in order to understand the growth mechanisms of CIGSe.

One can notice in Fig. 2.6 that for temperatures of up to ≈ 800°C a wide range of Cu concentrations between ≈ 23 at.%−25 at.% exists in which $CuInSe_2$ occurs as single phase (α-phase). Since 25 at.% represents the stoichiometric Cu concentration for $CuInSe_2$, this means that one can grow significantly Cu-poor $CuInSe_2$ films without obtaining any additional secondary phase. A Cu-poor composition of CIGSe implies the formation of

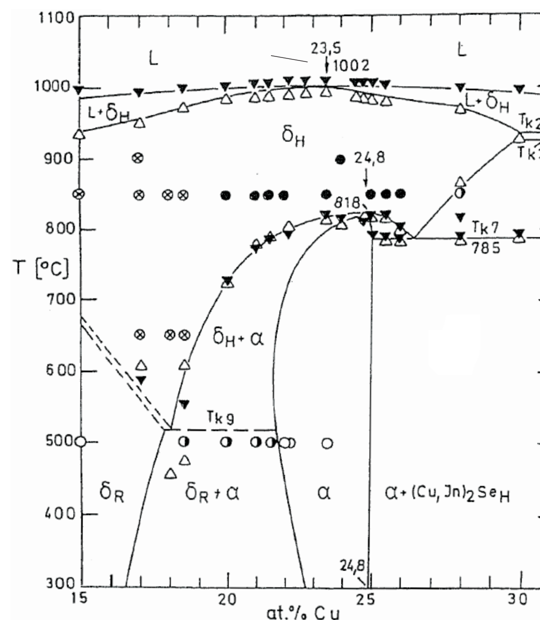

Figure 2.6: *Phase diagram of $CuInSe_2$ along the pseudo-binary cut $In_2Se_3-Cu_2Se$ between 15 at.% and 30 at.% Cu. The chalcopyrite-type $CuInSe_2$ phase and the compound $CuIn_3Se_5$ are indicated by the greek letters α and δ, respectively. From [49].*

defect states to compensate for the non-stoichiometric composition (see Tab. 2.1).
For Cu concentrations between ≈ 16 at.%−23 at.% the $CuInSe_2$ phase coexists with a $CuIn_3Se_5$ phase (δ-phase). $CuIn_3Se_5$ crystallizes in a similar lattice structure as $CuInSe_2$. However, it possesses a defined number of Cu vacancies V_{Cu} and antisite defects In_{Cu} [37]. For Cu concentrations below ≈ 16 at.% the $CuIn_3Se_5$ phase exists as single phase.
In contrast to Cu-poor growth conditions, the growth mechanism of $CuInSe_2$ is not as tolerant with respect to Cu-rich growth conditions. Already at Cu concentrations just above ≈ 25 at.% a secondary phase of $(Cu,In)_2Se$ emerges besides the $CuInSe_2$ phase. The coexistence of the two phases is observed for a wide range of Cu concentrations up to ≈ 66 at.%; around this Cu concentration the Cu_2Se phase occurs (not shown) [49].

3-stage process

Cu(In,Ga)Se_2 (CIGSe) solar cells reaching the highest energy conversion efficiencies on a laboratory scale are based on CIGSe absorber layers deposited by means of a complex physical vapor deposition (PVD) co-evaporation process [1]. This growth process consists of three sequential stages in which the chemical elements are evaporated with varying deposition rates and at varying substrate temperatures T_{Sub} [47, 50–53]; this is why this process is referred to as "3-stage process".

In Fig. 2.7 a schematic illustration of the 3-stage process is depicted. The different stages are indicated in the upper scale of the graphics and can be distinguished considering the deposition rates of the chemical elements.

- **Stage 1:** Ga-Se and In-Se are alternately co-evaporated at a substrate temperature of about 330°C. The composition of the "layered" (Ga-In-Ga-In)Se precursor determines the final Ga-content of the CIGSe thin films [53].

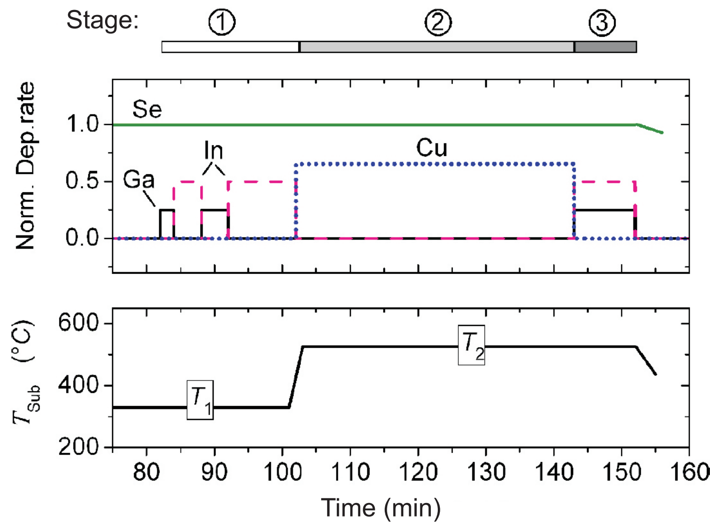

Figure 2.7: *Schematic illustration of the 3-stage process. In the upper row the deposition rate of the single elements during the co-evaporation is displayed (normalized to the Se deposition rate). In the lower row the corresponding substrate temperatures (T_{Sub}) are shown. From [54].*

- **Stage 2:** Cu and Se are co-evaporated at a substrate temperature of about 525°C. The increased substrate temperature results in an alloying of the chemical elements and the formation of the chalcopyrite phase. Stage 2 generally aims for a Cu/(In+Ga)-ratio of 1.15 at the endpoint, to obtain a large grain size [51, 53].
- **Stage 3:** Ga, In, and Se are co-evaporated at a substrate temperature of about 525°C (same substrate temperature as in stage 2), until the desired composition of the CIGSe thin film (Cu/(In+Ga)$\approx 0.84 - 0.88$) [53] is obtained. Subsequently, a cool down procedure is set off.

During the 3-stage process the growth parameters of the thin films (composition, thickness, roughness, etc.) are monitored with the help of laser light scattering and pyrometry, in order to assure a constantly high absorber quality [55].

2.2.3 Chemical surface conditioning

All $Cu(In,Ga)Se_2$ (CIGSe) thin films studied within this thesis were grown by means of a 3-stage co-evaporation process (see Sec. 2.2.2). After their fabrication the CIGSe samples were stored in an inert gas atmosphere. However, during the transport to the inert gas environment the samples were exposed to ambient air. It is well known from the literature that in particular In and Ga are prone to surface oxidation [56–58]. Hence, a surface oxidation of the CIGSe thin films seems likely.
In the course of this work Kelvin probe force microscopy (KPFM; see Sec. 4.1) is employed to investigate the electronic properties of CIGSe thin films. KPFM is a very surface sensitive tool which acquires its information from the first few atomic layers. To avoid an influence of surface oxidation on the experimental results, a method of surface conditioning is desirable that efficiently removes oxides and creates a defined surface with respect to the chemical composition.

A popular technique in surface science to remove oxides is Ar-ion sputtering. However, it has been shown that this method preferentially removes Se from CIGSe thin films [59], and therefore alters the chemical composition of the surface. Additionally, the formation of metallic Cu and In in connection with the Ar-ion sputtering has been observed for chalcopyrite materials [59].
Another approach to avoid surface oxidation in the first place is to Se-cap a CIGSe sample directly after its fabrication. The Se layer protects the surface from oxidation during the transport through ambient air and can be easily removed inside the vacuum chamber by annealing [60]. The downside of this method is that the vaporization of Se can significantly contaminate the vacuum chamber.

Potassium cyanide (KCN) etching

Within this thesis a potassium cyanide (KCN) etching (2min, 0.15M aqueous solution) was employed to remove oxides from CIGSe surfaces. Subsequent to the chemical treatment the samples were rinsed with deionized water to remove possible remains of K from the

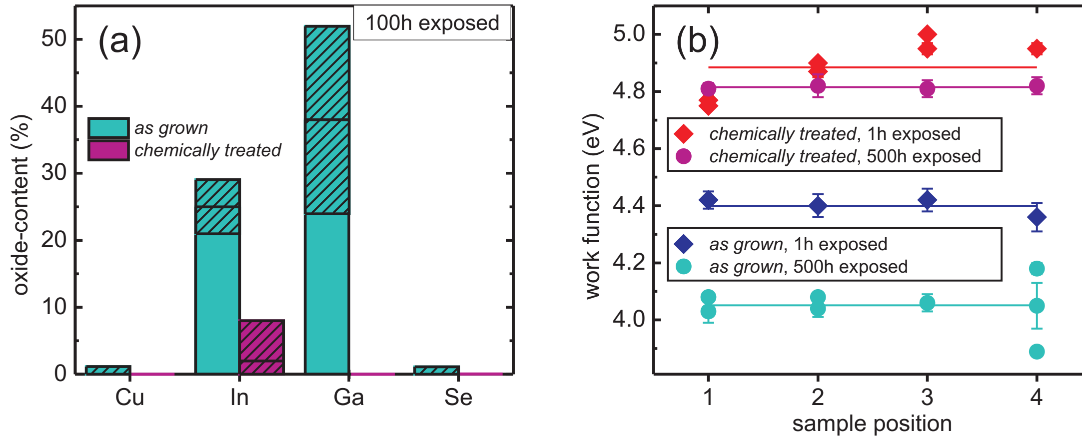

Figure 2.8: *(a) XPS-determined surface oxide content of the individual elements of a* $CuIn_{0.71}Ga_{0.29}Se_2$ *thin film after 100h exposure to ambient air prior (as grown) and after (chemically treated) the chemical treatment. The hatched areas indicate the error of the measurement. (b) Average work function of the same CIGSe thin film after 1h/500h exposure to ambient air as grown and chemically treated (determined on 4 macroscopically different sample positions by means of KPFM). From [58].*

surface [61]. The samples were kept in a deionized water environment during the transport to vacuum conditions to avoid any re-oxidation.

In Fig. 2.8 the effect of the KCN treatment on CIGSe thin films is demonstrated. Fig. 2.8 (a) displays results [58] of a X-ray photoelectron spectroscopy (XPS) analysis of the chemical composition of a CIGSe thin film prior to and after the KCN treatment. One can notice that after 100h exposure to ambient air both In and Ga exhibit a significant level of oxidation, while Cu and Se only show little surface oxidation. The KCN treatment removes almost all oxides from the surface. This finding is in good agreement with results reported in literature [62].
In Fig. 2.8 (b) the effect of the KCN treatment on KPFM measurements of the CIGSe thin films is displayed. A significant decrease in work function with increasing exposure time to ambient air was detected (blue symbols), indicating an increasing level of surface oxidation. Nevertheless, after the chemical treatment (red symbols) both samples (1h/500h exposure time) yield similar work function values around 4.8eV.
The results shown in Fig. 2.8 demonstrate that the KCN treatment efficiently removes oxides from the surface of CIGSe thin films. It creates a defined and reproducible surface condition, independent of the level of prior surface oxidation. Hence, KCN etching is an adequate tool to remove surface oxides from CIGSe thin films prior to KPFM experiments.

Chapter 3

Grain boundaries in $Cu(In,Ga)Se_2$

For many semiconductors materials like Si [63–65] or GaAs [66–68] it has been proven that the presence of grain boundaries (GBs) is detrimental with respect to the conductivity of the material, i.e. the performance of corresponding solar cells. In contrast, solar cells based on polycrystalline $Cu(In,Ga)Se_2$ (CIGSe) absorber layers (see Sec. 2.2.1) reach excellent conversion efficiencies despite the presence of a multitudinous number of GBs. Therefore, this record performance is at least partly attributed to special electronic properties of GBs in CIGSe thin films.

This chapter gives a general introduction into the subject of GBs. It will introduce the concept of the coincidence site lattice, which allows for a classification of GBs based on their symmetry. Subsequently, the chapter will focus on the electronic properties of GBs in CIGSe thin films. It will summarize the most prominent models to explain their benign behavior and give an overview of previous investigations dealing with GBs in CIGSe.

3.1 General properties of grain boundaries

During the formation of a solid by nucleation and growth small crystallites are randomly orientated throughout the solidifying phase. These crystalline grains continuously grow until they converge with neighboring grains. The location of encounter of two grains is called grain boundary (GB). Due to the resulting mismatch in atomic structure, a high density of structural and electronic defects like lattice distortions or dangling bonds is present at GBs [69].
In general, neighboring grains exhibit different orientations in polycrystalline materials. Therefore, various arrangements of the lattice structures of neighboring grains exist at GBs; these arrangements are called GB "orientations". The determination of the atomic orientation of a GB is a rather complex challenge. In general, a GB has five degrees of freedom[1]. Three rotation angles for the transformation of the lattice structure between the two grains and two degrees of freedom that define the orientation of the GB plane with respect to the lattice structure. Due to the symmetry of the crystal lattice, there is a large

[1]Note that two parameters are sufficient to define the GB plane since the length of the normal vector (h, k, l) usually used to define lattice planes is not of interest in this particular case. Consequently, two parameters (e.g. two angles between a unit vector and the coordinate axes) are sufficient.

number (infinite in many cases) of coordinate transformations which create the same GB orientation. The unambiguous definition of a GB orientation by means of a coordinate transformation is therefore not straight forward, and out of the scope of this thesis. For detailed information about this issue the lecture notes of H. Föll are recommended [70].

Coincidence site lattice

It turns out that GBs have a particularly small energy, i.e. they frequently occur in crystals, if the lattice orientations of two neighboring grains form so called "coincidence site lattices" (CSL) [70–72]. A CSL can be obtained by virtually extending the crystal lattice of one of the grains into the lattice structure of the other grain, as shown in Fig. 3.1 (a). The coinciding lattice points of both crystals form a periodic superstructure, the CSL. Many coincidence relations exist between the lattice structures of two grains. They can be unambiguously distinguished with the help of the following definition:

$$\Sigma = \frac{\text{Unit cell volume of the coincidence site lattice}}{\text{Unit cell volume of the individual crystal lattice}}. \tag{3.1}$$

One can mathematically show that the values of Σ are always odd [70]. As a Σ value of 1 denotes a perfect crystal structure, a Σ value of 3 consequently represents grain boundaries with the highest symmetry relationship between the neighboring grains. The so called "twin boundaries" are a special type of $\Sigma 3$ GBs, in which the lattice structures of the adjacent grains exhibit a mirror symmetry with respect to each other (see Fig. 3.1 (b)). Due to their low GB energy, $\Sigma 3$ twin boundaries are the most frequent type of GBs in materials like Si [70] or $Cu(In,Ga)Se_2$ [73, 74]. Following $\Sigma 3$ GBs, $\Sigma 5$ GBs possess the highest symmetry. The atomic structure of a $\Sigma 5$ GB can be seen in Fig. 3.1 (a).

Throughout this thesis the symmetry of GBs is denoted by means of the Σ value introduced in Eq. (3.1). One should note that this value, strictly speaking, only describes the orientation of the adjacent grains with respect to each other. It does not include any information about the orientation of the GB plane.

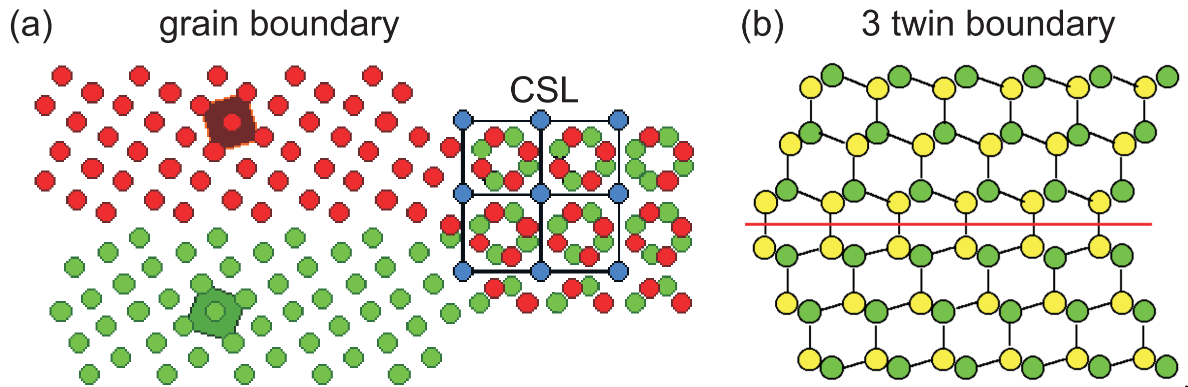

Figure 3.1: *(a) Two dimensional cubic lattice structure of adjacent grains forming a $\Sigma 5$ GB. (b) $\langle 110 \rangle$ projection of the diamond lattice structure exposing a $\Sigma 3$ twin boundary. In (a) the coincidence site lattice superstructure is indicated by blue dots. From [70].*

3.2 Electronic properties of grain boundaries in Cu(In,Ga)Se_2

Understanding the physics underlying the electronic properties of grain boundaries (GBs) in Cu(In,Ga)Se_2 (CIGSe) thin films is regarded as a means to developing more efficient CIGSe based solar cells. However, despite a high amount of research on this phenomenon it remains at the heart of controversial discussions in the science community [9–14]. This section introduces the four most prominent models to explain the benign properties of GBs in CIGSe, namely the *atomic relaxation model*, the *structural barrier model*, the *electronic barrier model*, and *the electronic + tunneling barrier model*. Subsequently, it discusses these models under consideration of various publications from the literature.

3.2.1 Various models of the electronic properties of grain boundaries

3.2.1.1 Atomic relaxation model

The *atomic relaxation model* was introduced by Yan et al. [11, 75]. By means of first principle density functional theory calculations they investigated the density of states at two Σ3 grain boundaries (GBs) in Cu(In,Ga)Se_2 (CIGSe). Both GBs possessed the same atomic structure (which they adopted from GBs in the cubic zinkblende material CdTe) with dislocation cores located at the GBs. A different configuration of dangling bonds, wrong bonds, and wrong bonding angles was present at the two GBs.
Yan's calculations revealed that in contrast to CdTe, where dislocation cores at GBs create deep level defects [76, 77], the formation of such defect states is not observed at GBs in CIGSe. The result was found to be independent of the exact bonding configuration. It is attributed to a strong repulsion between Se atoms resulting in a large atomic relaxation in the GB region [11]. Because of this atomic relaxation the defect levels move into the valence band and do not create deep level defects inside the band gap. Hence, GBs in

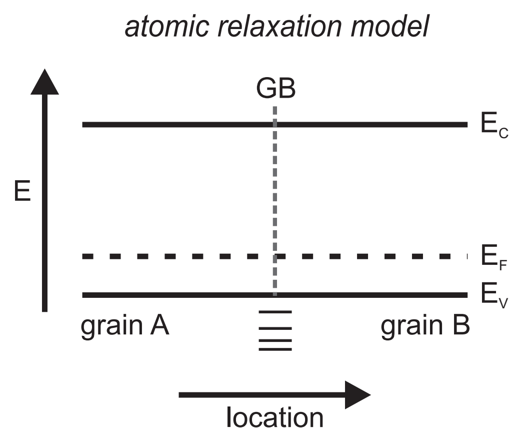

Figure 3.2: *Schematic of the electronic band diagram in the vicinity of GBs in CIGSe thin films, according to the atomic relaxation model. Defect states (arbitrary) at the GB are indicated by a sequence of small dashes.*

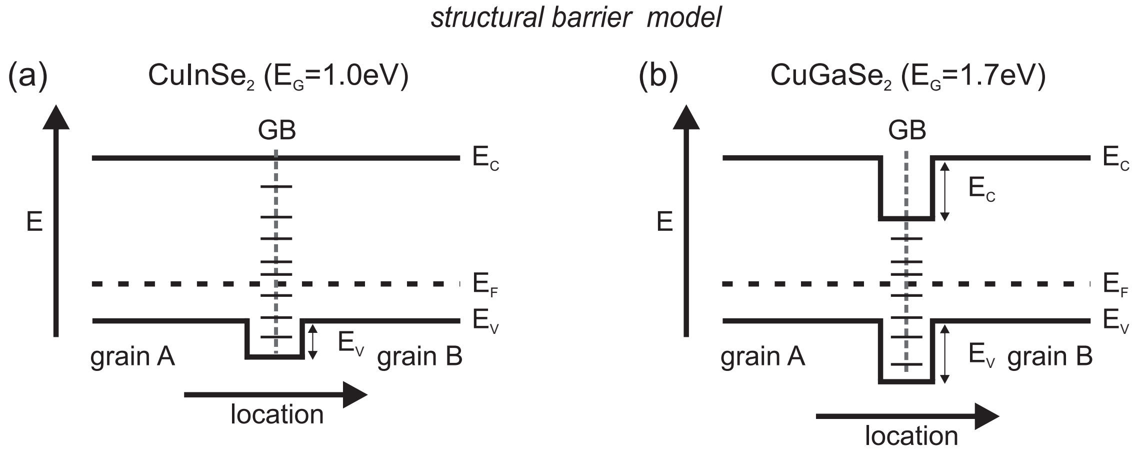

Figure 3.3: *Schematics of the electronic band diagram in the vicinity of (112) GBs in (a) CuInSe$_2$ and (b) CuGaSe$_2$ thin films, according to the structural barrier model [9, 78]. Defect states (arbitrary) at the GBs are indicated by a sequence of small dashes.*

CIGSe thin films exhibit an electronic band structure similar to the grain interior (see Fig. 3.2) and do not act as recombination centers.

3.2.1.2 Structural barrier model

The *structural barrier model* was introduced by Persson et al. [9, 78]. By means of first principle density functional theory they calculated the electronic band structure across grain boundaries (GBs) in Cu(In,Ga)Se$_2$ (CIGSe). For their calculations they assumed GBs to be "internal surfaces", i.e. they used the atomic structures of the (112) and $(\overline{112})$ surface facets (see Sec. 2.1.3) to model GBs. In the case of cation terminated (112) GBs they revealed a significant valence band offset ΔE_V of ≈ 0.2eV and ≈ 0.5eV for CuInSe$_2$ and CuGaSe$_2$, respectively (see Fig. 3.3). It is caused by a reduced repulsion between Cu-d and Se-p states at GBs, due to the formation of Cu vacancies at the (112) facets. Additionally, they detected a significant conduction band offset $\Delta E_C \approx 0.5$eV at GBs of CuGaSe$_2$, while they only observed a negligible ΔE_C at GBs of CuInSe$_2$. The width of all calculated band offsets is only a few atomic layers.
In case of anion terminated $(\overline{112})$ GBs neither a valence band offset nor a conduction band offset is present at GBs for both CuInSe$_2$ and CuGaSe$_2$. This results from a different charge compensation mechanism at the polar $(\overline{112})$ facets, which does not involve the formation of Cu vacancies (see Sec. 2.1.3).

The valence band offset at GBs represents an energy barrier that impedes holes from diffusion into the GB region. This diminishes electron-hole recombination at GBs and creates pathways for fast electron transport. A conduction band offset additionally attracts electrons to the GBs, hence causing a charge separation at the GB interface. This additionally reduces recombination at GBs.
Based on their results Persson et al. [78] concluded that it is in favor of solar cell performance to minimize the appearance of $(\overline{112})$ GBs in CIGSe thin films. In contrast to (112) GBs, $(\overline{112})$ GBs do not possess any electronic band offset and are consequently not beneficial for solar cell performance.

3.2.1.3 Electronic barrier model

The *electronic barrier model* is based on considerations from Kamins and Seto [63, 79] to explain the electronic properties of *p*-type polycrystalline silicon films. It was later adopted for II-VI semiconductors [80, 81] and chalcopyrite materials [31, 82–84]. The prevailing thought is that there is a large number of charged defect states at GBs because of the atomic disordering (see Sec. 3.1). The excess concentration of charge at a GB changes the electronic band structure and causes a band bending towards the GBs, i.e. a potential barrier. Thereby, the characteristics of the band bending depends on the sign of the net charge which is trapped at a GB.

- **Positive charge trapped at a GB (depletion):** If positive charge is trapped at a GB, free holes (CIGSe is a *p*-type semiconductor) are repelled from the near GB region. Ionized acceptors (negatively charged) are left, which form a hole-depleted space charge region (SCR) that compensates the positive charge at the GB. A downward band banding towards the GB is induced (see Fig. 3.4 (a)). The potential distribution across the SCR can be calculated based on the Poisson equation:

$$\epsilon\epsilon_0 \frac{\partial^2 V_{GB}(l)}{\partial l^2} = -\rho(l) = -eP_{net}, \tag{3.2}$$

  where ϵ is the dielectric permeability of the CIGSe material, ϵ_0 is the dielectric constant, $V_{GB}(l)$ is the potential distribution across the GB, ρ is the charge density of the CIGSe material, e is the elemental charge, and P_{net} is the net doping density of the *p*-type CIGSe material. Two-time integration of Eq. (3.2) under consideration of suited boundary conditions[2] yields an expression for the potential distribution, i.e. the band bending, across the GB [85, 86]:

$$V_{GB}(l) = \frac{eP_{net}}{2\epsilon\epsilon_0}(|l| - w)^2. \tag{3.3}$$

  Here, $|l|$ is defined between 0 and w, where $l = 0$ is the location of the GB, and w is the width of the SCR (see Fig. 3.4 (a)) which extends to both sides of the GB.

- **Negative charge trapped at a GB (accumulation):** If negative charge is trapped at a GB, free holes (CIGSe is a *p*-type semiconductor) are accumulated in the near GB region and compensate the trapped charge. An upward band banding towards the GB is induced (see Fig. 3.4 (b)). Considering only the majority carriers (holes), assuming quasi-neutrality[3] ($\Delta V_{GB} = V_{GB}(l = 0) - V_{GB}(l = \infty) << \frac{k_B T}{e}$), and a Maxwell-Boltzmann distribution for the energy of free holes one can calculate the potential distribution in the vicinity of the GB [85]:

$$V_{GB}(l) = V_{GB}(l = 0) \cdot \mathrm{e}^{-\frac{|l|}{L_{Db}}}, \tag{3.4}$$

[2] electric field $\mathbf{E}(l = w) = 0$, potential barrier $V_{GB}(l = w) = 0$

[3] Note that the assumption of quasi-neutrality, strictly speaking, does not hold for potential barriers observed at GBs in CIGSe. k_B is the Boltzmann constant, and T is the absolute temperature.

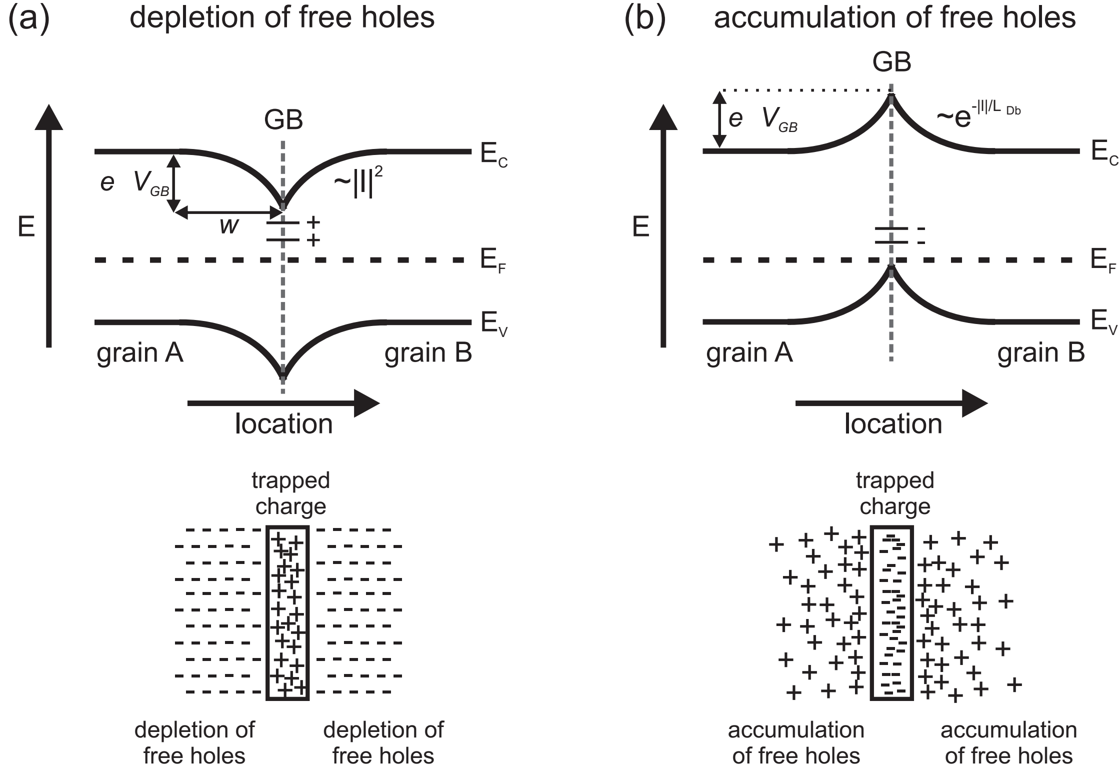

Figure 3.4: *Schematics of the electronic band diagram in the vicinity of GBs in CIGSe thin films for (a) positive charge trapped at a GB (depletion) and (b) negative charge trapped at a GB (accumulation), according to the electronic barrier model [63, 79]. Defect states (arbitrary) at the GB are indicated by a sequence of small dashes. Below the band diagrams 2 dimensional schematics of the specific charge compensation mechanisms in the case of a p-type semiconductor (i.e. CIGSe) are shown. From [87].*

where $L_{Db} = \sqrt{\frac{\epsilon\epsilon_0 k_B T}{e^2 P_{net}}}$ is the Debye-length, and $l = 0$ is the location of the GB.

Since the potential distribution in the case of depletion exhibits a quadratic dependence, while the potential distribution in the case of accumulation can be approximated by an exponential function, one would assume smaller widths of the potential barriers in the latter case. To verify this assumption the widths of typical potential barriers ΔV_{GB} for both the depletion case (Fig. 3.4 (a)) and the accumulation case (Fig. 3.4 (b)) were calculated. Typical values of ϵ, P_{net}, and ΔV_{GB} found in CIGSe thin films were used for the calculations. An experimental noise level[4] of 10mV was assumed, i.e. it was calculated at which distance from the center of the GB a potential barrier decays to 10mV. The results of the calculations are shown in Tab. 3.1.

It turns out that for a band bending of 100mV the potential barrier in the case of depletion is actually slightly smaller than in the case of accumulation. However,

[4]Note that it is necessary to assume an experimental noise level in order to define the width of a potential barrier in the case of accumulation, as Eq. (3.4) only decays to 0 for $l \to \pm\infty$.

Table 3.1: *Widths of negative (depletion) and positive (accumulation) potential barriers ΔV_{GB} at GBs for various values of ΔV_{GB}. The widths were calculated based on Eq. (3.3) and Eq. (3.4) respectively, considering an experimental noise level of 10mV. Typical values of $P_{net} = 5 \times 10^{16} cm^{-3}$ (see Sec. 6.4.3) and $\epsilon = 11$ [88] were used for the calculations.*

ΔV_{GB} (mV)	**Width of potential barriers (nm)**	
	Depletion	**Accumulation**
100	35	39
200	55	51
400	85	63

with increasing band bending the exponential decay of the accumulation scenario results in a narrower potential barrier than the depletion case.
Nevertheless, the barrier widths for both scenarios are generally similar for typical ΔV_{GB} expected at GBs of CIGSe thin films. Consequently, no significant difference in the width of potential barriers should be detected experimentally between the depletion case and the accumulation case.

In the framework of the *electronic barrier model* it is believed that a downward band bending towards GBs, i.e. the depletion case, is beneficial for solar cell performance, as holes are repelled from the near GB region and reflected towards the grain interior. In contrast, electrons are attracted to such GBs, which consequently provide a hole depleted conduction pathway through the CIGSe material [83, 84]. This reduces recombination at GBs.

3.2.1.4 Electronic + tunneling barrier model

Simplified, the *electronic + tunneling barrier model* represents a combination of the *structural barrier model* and the *electronic barrier model*. It was proposed separately by Azulay

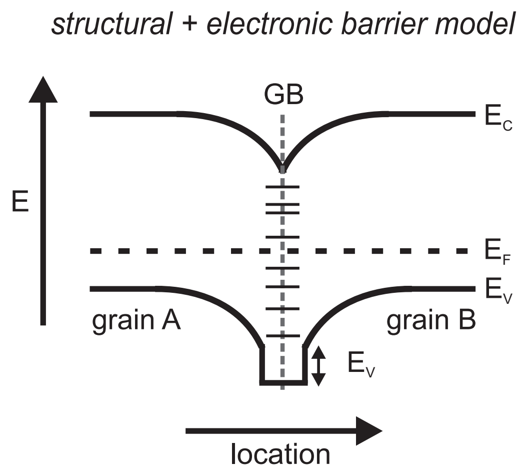

Figure 3.5: *Schematics of the electronic band diagram in the vicinity of GBs in CIGSe thin films, according to the structural + electronic barrier model [13, 89]. Defect states (arbitrary) at the GB are indicated by a sequence of small dashes.*

et al. [89] and Hafemeister et al. [13] to explain experimental results obtained by means of conductive atomic force microscopy and combined Kelvin probe force microscopy/Hall measurements, respectively. The model postulates the presence of a potential barrier for holes at GBs in CIGSe that is a few nm wide and several hundred mV deep, in addition to a downward band bending (depletion) of about 100mV. A schematic of the associated energetic band diagram can be seen in Fig. 3.5.
Hafemeister et al. [13] pointed out that tunneling across the narrow hole barrier must be present, in order to explain the temperature dependence of the Hall resistance across GBs in CIGSe. Such a tunneling mechanism is not explicitly mentioned in the original *structural barrier model*.
It is expected in the framework of the *electronic + tunneling barrier model* that the probability density function of holes is considerably lowered at GBs, which should reduce the recombination activity of GBs.

3.2.2 Status quo of grain boundary research

A variety of theoretical approaches, simulation methods, and experimental techniques have been employed in the past to improve the understanding of the electronic properties of grain boundaries (GBs) in $Cu(In,Ga)Se_2$ (CIGSe) thin films. The obtained results are discussed controversially, and some of them are even contradicting. This section will provide a short overview of results, thus giving the reader an idea of the status quo of research on GBs in CIGSe. Note that these results only represent a small fraction of all research performed on this topic. For a more elaborate introduction the review articles of Rau [12] and Siebentritt [90] are recommended.

By means of combined Kelvin probe force microscopy (KPFM) and Hall measurements Siebentritt et al. [91] found evidence for a neutral barrier to majority carrier (hole) transport across a $\Sigma 3$ GB in $CuGaSe_2$. Such a barrier is predicted by the *structural barrier model* (see Sec. 3.2.1). However, Siebentritt et al. only observed a valence band offset ΔE_V of $\approx$ 30meV, while theoretically an offset of about 500meV was predicted by Persson et al. [78].
Hafemeister at al. [13] reconsidered this problem by means of temperature dependent Hall resistance measurements. They revealed the necessity of a small neutral hole barrier of $\approx$ 170meV in addition to the 30meV valence band offset observed by Siebentritt et al. in order to explain their experimental results by quantum mechanical tunneling through the barrier.
Taretto et al. [92–94], Gloeckler et al. [95], and Metzger et al. [96] studied the effect of such a valence band offset ΔE_V by means of two dimensional device simulations. They found an improvement of solar cell performance with increasing ΔE_V. According to the authors, a ΔE_V of at least 300meV is required in order to reach device efficiencies above 19%. However, even with such a high valence band offset the achieved cell efficiencies never exceeded the efficiencies of cells without GB defects. Based on the simulation results Rau et al. [12] concluded that an internal valence band offset is unlikely to be the exclusive reason for the low electronic activity of GBs in CIGSe thin films.
Additionally, Yan et al. [97] pointed out that not all GBs in CIGSe thin films contain Cu vacancy rows. By means of transmission electron microscopy high resolution z-contrast

imaging and nanoprobe X-ray energy-dispersive spectroscopy they did not observe a Cu-depletion at (112) GBs in CIGSe. However, such a Cu-depletion is the essential assumption of the *structural barrier model*. Without a Cu-depletion a valence band offset does not emerge at (112) GBs in CIGSe [97]. Yan et al. therefore questioned the validity of the *structural barrier model*.

Instead, Yan et al. [11, 75] proposed their own model to explain the benign electronic properties of GBs in CIGSe, the *atomic relaxation model* (see Sec. 3.2.1). Mönig et al. [14] indeed succeeded to find experimental evidence for this model. By means of scanning tunneling spectroscopy they detected a reduced density of deep level defects at GBs in CIGSe. Their results pointed to an increased density of defect levels in the lower conduction band at GBs.

One weakness of all theory-based models to explain the electronic properties of GBs is that they rely on a certain symmetry of GBs. However, GBs in polycrystalline CIGSe thin films exhibit various symmetry relationships [73, 74]. It is known that the symmetry of GBs influences the electronic properties. By means of electron beam induced current measurements differences in carrier recombination have been observed between high symmetry $\Sigma 3$ GBs and lower symmetry non-$\Sigma 3$ GBs [98, 99]. In KPFM studies a $\Sigma 3$ GB in epitaxially grown $CuGaSe_2$ was found to be charge neutral [91], while a $\Sigma 9$ GB of the same material exhibited a charged potential barrier of ≈ 90mV [13].

A band bending towards GBs, as proposed in the *electronic barrier model* by Kamins [63] and Seto [79] (see Sec. 3.2.1), has been observed in a multitude of studies. While downward band bending towards GBs (depletion) was reported more frequently [10, 11, 13, 83, 84, 89, 100–104], several studies found evidence for upward band bending towards GBs (accumulation) as well [58, 98, 102].
By means of KPFM Sadewasser et al. reported on a downward band bending of $\approx 100-200$meV at GBs in $CuGaSe_2$ [100]. With the same experimental technique, Jiang et al. [84] studied the band bending at GBs of CIGSe in dependence of the Ga-content. For Ga-contents below $x \approx 0.3$ they found a downward band bending of ≈ 150meV towards GBs, while they did not observe any band bending for higher Ga-contents. Based on the *electronic barrier model* they concluded on a direct connection between their finding and the performance of CIGSe based solar cells.
Applying electro-assisted scanning tunneling microscopy Romero et al. [105] studied the electron transport across GBs in CIGSe as a function of the Ga-content. They detected a transport barrier across GBs for CIGSe samples with high Ga-content, while they did not observe such a barrier for samples with low Ga-content.
The effect of a band bending towards GBs on solar cell performance was investigated by means of two dimensional numerical device simulations. Taretto et al. [92–94] revealed that the introduction of downward band bending towards GBs leads to a decline of solar cell efficiency in the case of high quality CIGSe absorber layers. This finding is independent of the precise position of defect states inside the electronic band gap. If type inversion is present at GBs, a significant increase in short circuit current J_{sc} of solar cells is observed. However, cell efficiencies do not increase, due to an increased recombination which affects the open circuit voltage V_{oc} of solar cells negatively.
Similar results were obtained by Glöckler et al. [95]. Additionally, they investigated the effect of upward band bending towards GBs on the solar cell efficiency. They revealed a small beneficial effect of upward band bending on device efficiency, due to a partial

mitigation of recombination at GBs. However, for high quality CIGSe material this effect is almost negligible.

Chapter 4

Experimental methods of characterization

This chapter introduces the experimental methods applied in the framework of this thesis in detail. It begins with an explanation of the principle of Kelvin probe force microscopy (KPFM), which is the main characterization method employed in the framework of this thesis. KPFM is used to gather information about the electronic properties of grain boundaries (GBs) in polycrystalline $Cu(In,Ga)Se_2$ (CIGSe) thin films with a high spatial and energy resolution.
The second part of the chapter presents two different methods based on scanning electron microscopy (SEM). The first method, the so called "SEM topography imaging", is used several times throughout this thesis to record 2D surface topography images with a spatial resolution down to the nanometer range. The second method, electron backscatter diffraction (EBSD), is applied in Chap. 7 to gather information about structural properties of GBs in polycrystalline CIGSe thin films.

4.1 Kelvin probe force microscopy (KPFM)

Kelvin probe force microscopy (KPFM) enables the simultaneous mapping of a sample's surface topography and work function with a high spatial and energy resolution down to the nanometer (nm) and millielectronvolt (meV) range, respectively. It is based on atomic force microscopy, which was invented by Binning et al. in 1986 [106]. Since its invention in 1991 [107, 108] KPFM was steadily improved by various working groups [109–111]. By now, KPFM is a very popular tool in nanoscience, finding applications on a broad variety of material systems such as semiconductors [13, 112, 113], insulators [114–116], and organic molecules [117–119].

4.1.1 Atomic Force Microscopy (AFM)

The invention of the scanning tunneling microscope (STM) in 1982 [120, 121] revolutionized surface science, as for the first time it became possible to image surfaces with atomic

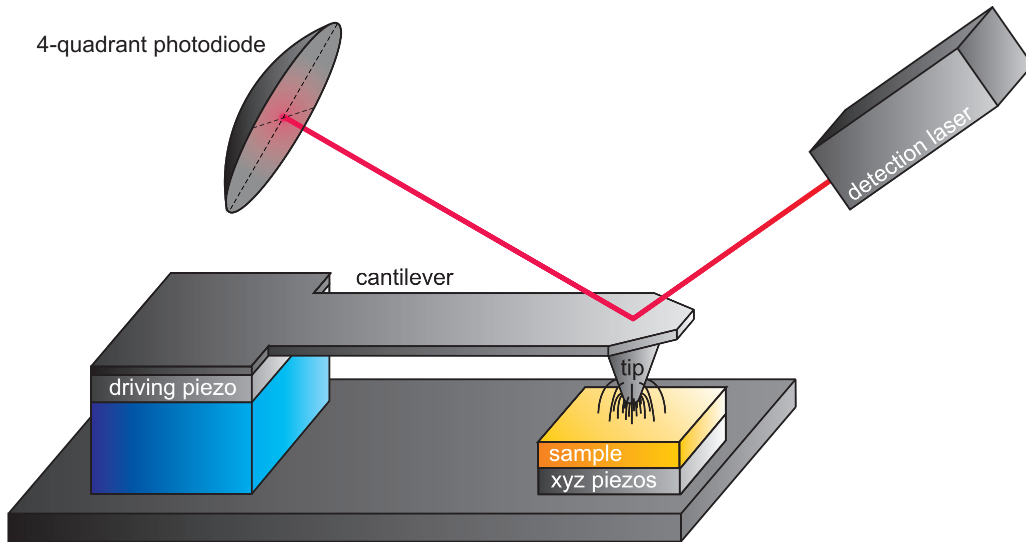

Figure 4.1: *Schematic of a typical setup of an atomic force microscope.*

resolution [122]. The STMs impact was so tremendous that only four years after its invention the 1986 Nobel Prize in physics was awarded to the inventors [123]. However, the scope of STM is limited to conductive materials, as the tunneling current between a tip and a sample is employed as imaging signal. To overcome this material gap and with the goal to "show atomic resolution also on non-conducting surfaces [124]" the atomic force microscope (AFM) was developed in 1986 [106, 125]. By means of AFM it soon became possible to map surface topographies of both conductors [126] and insulators [127] with atomic resolution.

The principle of AFM is based on a force-interaction between a sharp AFM-tip and the surface of a sample. Fig. 4.1 shows a schematic of a typical AFM-setup. The AFM-tip is mounted to the end of a flexible cantilever. If the tip scans the sample surface, the cantilever deflects due to the force-interaction between tip and sample. This deflection is monitored by a 4-quadrant photodiode, which detects the reflection of a laser beam from the backside of the cantilever. A *xyz* piezo, on which the sample is mounted, accounts for the highly precise motion of the sample during the scan. If required, a driving piezo induces an oscillation to the cantilever.

In general, there are two different modes of operation in AFM; the *contact* mode, and the *non-contact* mode:

- **Contact mode:** In *contact (c)*-mode AFM-tip and sample are in direct contact. While the tip scans across a surface the static deflection of the cantilever, which corresponds directly to the surface topography, is detected by the photodiode. Thereby, an image of the surface topography is reconstructed.

- **Non-contact mode:** The *non-contact (nc)*-mode is a dynamic mode of operation. The driving-piezo mechanically excites the cantilever to an oscillation at its fundamental resonance frequency f_0. The resonance frequency f_0 is determined by the spring constant k of the cantilever and its effective mass m^*, which contains the geometry information:

$$f_0 = \frac{1}{2\pi}\sqrt{\frac{k}{m^*}}. \tag{4.1}$$

An external force F_{ex} between tip and sample causes, in a first-order approximation for small oscillation amplitudes, a change in the spring constant of the cantilever:

$$k' = k - \frac{\partial F_{ex}}{\partial z}, \tag{4.2}$$

where $\frac{\partial F_{ex}}{\partial z}$ is the force gradient between tip and sample. This force interaction changes the resonance frequency of the cantilever to:

$$f_0' = f_0\sqrt{1 - \frac{1}{k}\frac{\partial F_{ex}}{\partial z}}. \tag{4.3}$$

If $\frac{\partial F_{ex}}{\partial z}$ is small compared to the spring constant k, one can Taylor expand Eq. (4.3) as:

$$f_0' \approx f_0(1 - \frac{1}{2k}\frac{\partial F_{ex}}{\partial z}). \tag{4.4}$$

Consequently, one obtains a shift Δf of the resonance frequency of the cantilever, which is induced by the force interaction between tip and sample:

$$\Delta f = f_0' - f_0 \approx -f_0\frac{1}{2k}\frac{\partial F_{ex}}{\partial z}. \tag{4.5}$$

There are two popular modes of operation, which can be employed to maintain a constant tip-sample distance in *nc*-AFM; the "amplitude modulated" mode, and the "frequency modulated" mode:

- **Amplitude modulated mode:** In the amplitude modulated (AM)-mode variations of the oscillation amplitude, due to the tip-sample interaction, are monitored to maintain a constant tip-sample distance [128]. The oscillation amplitude is sensitive to the force F_{ex} itself. One drawback of the AM-mode is that it cannot be operated in UHV [129]. Therefore, it is mostly applied in air-based AFM-setups, which do not aim for highest resolution.
- **Frequency modulated mode:** In the frequency modulated (FM)-mode the frequency shift Δf is maintained at a predefined setpoint during the measurement. Consequently, the trajectory of the tip corresponds to a surface of constant force gradient (see Eq. (4.5)) and reconstructs the surface topography. The FM-mode allows for a high sensitivity, as it can be operated under UHV-conditions [129].

Depending on the tip-sample distance, different forces interact between tip and sample. For large tip-sample distances $>\approx$ 1nm attractive ($\frac{\partial F_{ex}}{\partial z} > 0$), long range forces

like the van-der-Waals forces, the electrostatic force, and the magnetic force[1] are dominant and result in a negative Δf. For smaller tip-sample distances attractive short range forces, which originate from chemical bondings, are present as well. In case of extremely small tip-sample distances well below 1nm the frequency shift Δf becomes positive. In this regime the wave functions of tip- and sample-atoms overlap, and repulsive forces caused by Pauli-repulsion are dominant [130].
Since the information about the topography of a surface is mainly contained in the van-der-Waals and atomic forces, electrostatic forces need to be nullified prior to *nc*-AFM measurements, as they could falsify the experimental result [131].

4.1.2 From AFM to KPFM

Kelvin probe force microscopy (KPFM) is based on *non contact (nc)*- atomic force microscopy (AFM) operated in the frequency modulated (FM)-mode (see Sec. 4.1.1). While in *nc*-AFM the electrostatic forces are nullified statically prior to a measurement, in KPFM the electrostatic forces are nullified dynamically during the measurement. This dynamic nullification implicates two principle advantages of KPFM over regular *nc*-AFM. Firstly, it always guaranties a correct topography measurement even in case of electronically inhomogeneous samples, as the electrostatic forces are always compensated correctly. This can not be assured in *nc*-AFM measurements. There, a superposition of van-der-Waals forces and residual electrostatic forces might falsify the topography measurements in case of inhomogeneous surfaces [131]. Secondly, one gains additional information about the electronic properties of a sample by means of KPFM. Since the electrostatic forces are nullified individually for each tip-position on the surface, a laterally resolved image of the work function is obtained simultaneously to the topography image.

The first part of this section introduces the general Kelvin principle to determine the work function. The second part of the section then deals with the implementation of this principle to AFM.

4.1.2.1 Kelvin principle to determine work functions

The Kelvin principle is a comparative method to determine the work function (Φ) of a metallic sample. It was introduced for the first time in 1898 by Lord Kelvin [133]. In Fig. 4.2 the basic mode of operation of the Kelvin principle is explained.
Fig. 4.2 (a) shows a schematic band diagram of two metals with different work functions $\Phi_{1/2}$. The metals are not in contact, their vacuum-levels are equal. If both metals are now brought into contact, electrons flow from the metal with the lower work function to the metal with the higher work function, until the Fermi-levels of both metals are aligned. Due to this charge transfer, a contact potential difference V_{CPD} between the two metals develops, as can be seen in Fig. 4.2 (b). This contact potential difference is proportional to the work function difference $\Delta\Phi$ between both metals:

[1]Since magnetic materials have not been used throughout the thesis, magnetic forces are not considered in the following.

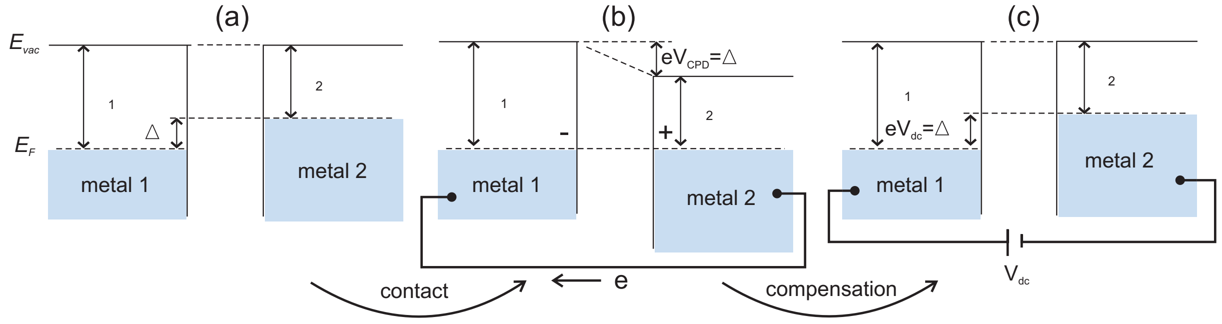

Figure 4.2: *Schematics of the electronic band structure of two metals with different work functions $\Phi_{1/2}$ (modified from [58, 132]). (a) The metals are not in contact, their vacuum-levels E_{vac} are equal. (b) If the metals are electronically connected, their Fermi-levels E_F align and the contact potential difference V_{CPD} arises between the metals. (c) This potential difference can be compensated by an external voltage V_{dc}.*

$$V_{CPD} = \frac{1}{e}(\Phi_2 - \Phi_1) = \frac{\Delta\Phi}{e}. \tag{4.6}$$

By applying an external voltage V_{dc} between the metals that matches V_{CPD} it is possible to compensate the contact potential difference. This scenario is illustrated in Fig. 4.2 (c). Consequently, one can obtain the work function of one of the metals, if the work function of the other metal is known.

4.1.2.2 The implementation of the Kelvin principle to AFM

If one considers the KPFM tip-sample system as a capacitor, the resulting electrostatic force caused by a potential difference V_{TS} between tip and sample is given by:

$$F_{el} = -\frac{1}{2}\frac{\partial C}{\partial z}V_{TS}^2, \tag{4.7}$$

where $\frac{\partial C}{\partial z}$ is the capacitance gradient, which contains the distance dependence of the electrostatic force.

In general, different work functions of tip and sample result in a contact potential difference V_{CPD}, as described in Sec. 4.1.2.1. In order to compensate this contact potential difference an external voltage is applied between tip and sample. It is composed of an *ac*- and a *dc*-part. The *ac*-part V_{ac} enables the dynamic detection of the electrostatic force, as explained below. The *dc*-part V_{dc} is used to nullify the contact potential difference between tip and sample (see Fig. 4.2 (c)).
Hence, the complete potential difference between tip and sample can be written as:

$$V_{TS}(t) = V_{dc} - V_{CPD} + V_{ac}sin(\omega t), \tag{4.8}$$

where ω is the angular frequency of the *ac*-voltage oscillation.

If Eq. (4.8) is inserted in Eq. (4.7), one obtains the resulting electrostatic force between tip and sample, which is split up into three parts:

$$F_{el} = F_{dc} + F_{\omega} + F_{2\omega}, \tag{4.9}$$

where:

$$F_{dc} = -\frac{\partial C}{\partial z}\left[\frac{1}{2}(V_{dc} - V_{CPD})^2 + \frac{V_{ac}^2}{4}\right], \tag{4.10}$$

$$F_{\omega} = -\frac{\partial C}{\partial z}(V_{dc} - V_{CPD})V_{ac}sin(\omega t), \tag{4.11}$$

$$F_{2\omega} = +\frac{\partial C}{\partial z}\frac{V_{ac}^2}{4}cos(2\omega t). \tag{4.12}$$

While the first part, F_{dc}, is frequency independent, the two other parts, F_{ω} and $F_{2\omega}$, oscillate with frequencies proportional to ω.
In case of a correct compensation of the contact potential difference between tip and sample ($V_{dc} = V_{CPD}$) the force component F_{ω} vanishes. The frequency independent part F_{dc} is then proportional to V_{ac}^2, and causes a small, permanent shift in the resonance frequency f_0'. The third part of the force, $F_{2\omega}$, depends on the capacitance gradient $\frac{\partial C}{\partial z}$, and can be used for capacitance spectroscopy [134].

There are two popular modes of operation, which can be employed for the detection of the contact potential difference; frequency modulated KPFM, and amplitude modulated KPFM [135]:

- **Frequency modulated KPFM:** Frequency modulated (FM)-KPFM [110] is based on the fact that the frequency dependent force component F_{ω} induces an oscillation to the frequency shift Δf, as can be seen from Eq. (4.5). This oscillation is detected by a lock-in amplifier and nullified by applying an appropriate voltage $V_{dc} = V_{CPD}$ (see Eq. (4.11)). Strictly speaking, the FM-KPFM detection is not sensitive to the electrostatic force itself, but to its force gradient $\frac{\partial F_{el}}{\partial z}$, as can also be seen in Eq. (4.5). As the force gradient has a stronger distance dependence than the force, averaging effects, e.g. of the tip, have a smaller effect on FM-KPFM measurements compared to force-sensitive detection methods [136].

- **Amplitude modulated KPFM:** In the force sensitive amplitude modulated (AM)-KPFM [109] the cantilever oscillation, which is induced by F_{ω}, is directly detected by a lock-in-amplifier. The oscillation, which is directly proportional to F_{ω}, is then nullified by adjusting V_{dc} to V_{CPD} (see Eq. (4.11)).
  The sensitivity of AM-KPFM can be significantly increased, if the *ac*-oscillation frequency ω is tuned to the 2nd resonance frequency f_2 of the cantilever. In this so called "resonance-enhanced" AM-KPFM it is possible to apply low *ac*-voltages around 100mV between tip and sample[2]. The use of such low voltages avoids a

[2]For FM-KPFM *ac*-voltages between 2V-5V are regularly used.

bending of the electronic band structure of a sample towards the surface. Generally, band bending can be easily induced through the tip of the cantilever, in particular on semiconductor surfaces, as the electric field at sharp features, i.e. the tip, is very high. It is necessary to avoid an induced surface band bending during KPFM measurements, as it could falsify the experimental results [111, 137].

As the emphasis of this thesis is to study the electronic properties of semiconductor materials, all KPFM experiments reported in this thesis were performed applying the "resonance enhanced" AM-KPFM mode.

4.1.2.3 Work function images

Both modes, FM-KPFM and AM-KPFM, provide spatially resolved images of the contact potential difference between tip and sample surface. In order to convert these images to work function images via Eq. (4.6), the work function of the used tip must be known. It is determined by means of calibration measurements on a surface with a known work function.
For all experiments reported in this thesis a highly oriented pyrolytic graphite (HOPG) sample was used for tip-calibration. The work function of the HOPG surface itself was determined by extensive calibration measurements on various metal surfaces.

In Fig. 4.3 typical KPFM images of topography and work function of an untreated polycrystalline Cu(In,Ga)Se_2 thin film are shown. Such images are discussed in more detail in Chaps. 5-7. At this point the images only serve as examples to illustrate the different color codes which are used throughout the thesis to distinguish topography and work function images:

- **Topography images:** The z-scale of topography images is depicted using a color code ranging from black to red to white (see Fig. 4.3 (a)).
- **Work function images:** The z-scale of work function images is depicted using a color code ranging from black to green to white (see Fig. 4.3 (b)).

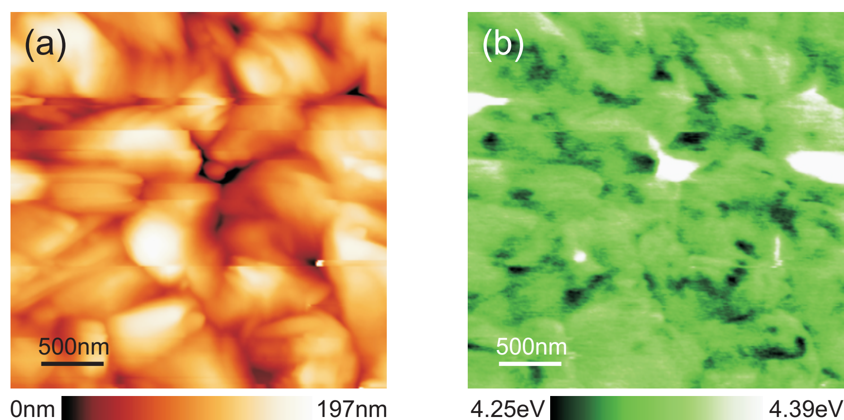

Figure 4.3: *Typical KPFM images of (a) topography and (b) work function of an untreated, polycrystalline $CuIn_{0.67}Ga_{0.33}Se_2$ thin film.*

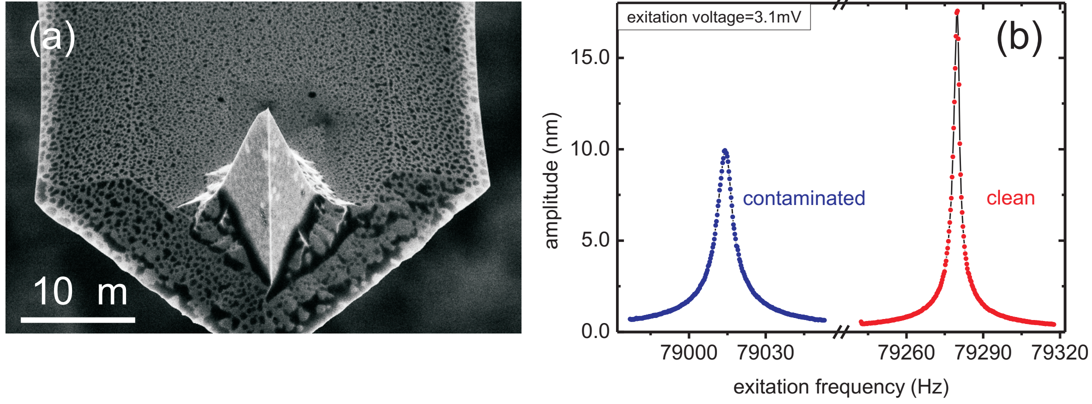

Figure 4.4: *(a) Scanning electron micrograph of a typical Pt-Ir coated Si cantilever used for the KPFM measurements. (b) Fundamental resonance peaks of an identical cantilever before (blue) and after annealing (red). The resonance peak of the annealed cantilever is shifted by about +280Hz, due to the removal of contaminations. Additionally, its resonance peak is sharper, and the amplitudete-to-exitation ratio is improved.*

4.1.3 Experimental details

4.1.3.1 KPFM system

All Kelvin probe force microscopy (KPFM) measurements were performed inside a commercial ultra high vacuum (UHV) system from Omicron NanoTechnology GmbH (*www.omicron.de*). The base pressure of the system was $p_b < 10^{-10}$mbar, which ensured unaltered sample surfaces and cantilever-tips during a series of measurements. For pressure-control Bayard-Alpert ionization-gauges from Pfeiffer Vacuum technology were used (*www.pfeiffer-vacuum.de*). The KPFM itself is based on a commercial Omicron UHV atomic force microscope (AFM), which was modified in order to conduct KPFM measurements on semiconductor surfaces. Details about the modifications can be found in publications from Sommerhalter [111, 138] and Glatzel [139]. For the operation of the KPFM a combination of home-built and commercial electronics was used. A commercial AFM control system from Nanonis (*www.specs-zurich.com*) was utilized for the topography measurement. For the dynamic nullification of the electrostatic forces a homebuilt Kelvin-controller was employed. The Nanonis software package was used to control the entire KPFM system. For evaluation and post-processing of KPFM images the WSxM-software package was employed [140]. Pt-Ir coated Si cantilevers from Nanoworld (EFM-PPP, *www.nanoworld.com*) with typical fundamental resonance frequencies f_0 around 75kHz were used for all experiments. Fig. 4.4 (a) shows a typical scanning electron micrograph of such a cantilever. After introduction to UHV, all cantilevers were annealed at $\approx$ 130°C to remove residual contaminations. This is important, as a contamination of the cantilever-tip may lead to a reduced sensitivity during the measurements, as shown in Fig. 4.4 (b).

Fig. 4.5 shows a schematic of the used UHV-KPFM setup. For topography-detection FM-AFM is utilized. All measurements reported in this thesis were performed in the attractive force regime, i.e. with negative frequency shifts Δf (see Sec. 4.1.1). For detection of the

Figure 4.5: *Schematic of the UHV-KPFM setup used for all experiments (modified from [58, 139]). Topography images are obtained by FM-AFM (highlighted in gray). CPD images are obtained by "resonance enhanced" AM-KPFM (highlighted in blue).*

contact potential difference (CPD) between tip and sample "resonance-enhanced" AM-KPFM at the 2nd resonance frequency f_2 of the cantilever is applied (see Sec. 4.1.2.2). The cantilever oscillation is detected by an infrared laser (λ=980nm, E_{ph}=1.26eV) and a four-quadrant photodiode with a cut-off frequency of 500kHz. Band-pass filters are applied to separate the topography-detection at f_0 from the CPD-detection at f_2. The topography detection unit keeps the frequency shift of the cantilever at a constant Δf setpoint during a measurement, which allows reconstruction of the surface topography. For the CPD-detection the Kelvin controller dynamically adjusts the sample voltage V_{dc} during the scan to nullify the cantilever oscillation at f_2. In this way laterally resolved images of the CPD between tip and sample are obtained, simultaneously to topography images (see Sec. 4.1.2.2). The CPD images can be converted to work function images by means of calibration measurements on highly oriented pyrolytic graphite (see Sec. 4.1.2.3).

4.1.3.2 Determination of discrete work function values from KPFM images

Kelvin probe force microscopy (KPFM) provides spatially resolved images of the work function distribution of a sample surface. For a quantitative analysis of the work function

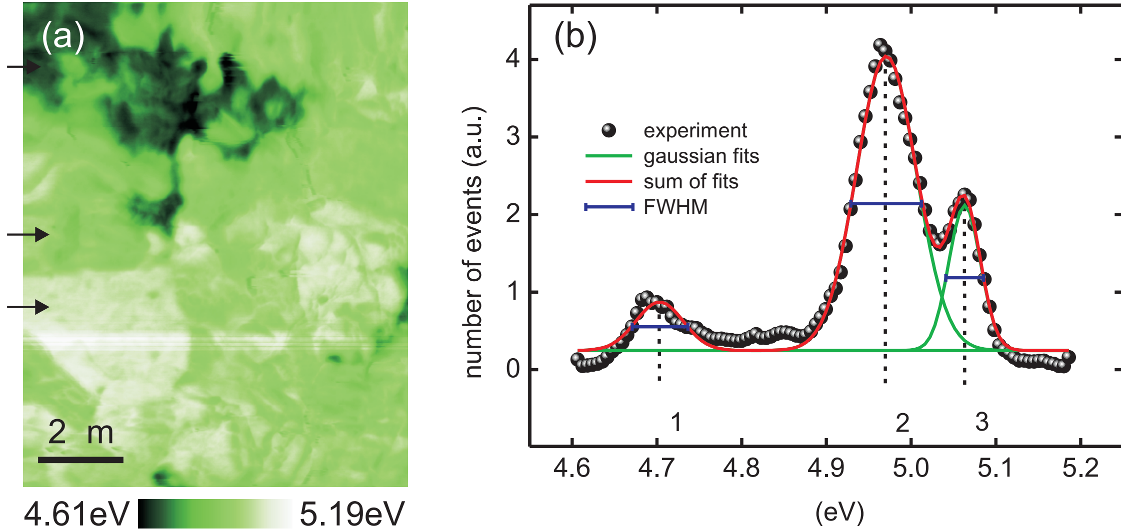

Figure 4.6: *(a) KPFM work function image of a $CuInSe_2$ thin film. (b) Histogram of the work function image from (a), fitted with a superimposition of three Gaussian distributions. From the Gaussian distributions one can obtain:*
$\Phi_1 = (4.70 \pm 0.03)eV$, $\Phi_2 = (4.97 \pm 0.04)eV$, *and* $\Phi_3 = (5.06 \pm 0.02)eV$.

distribution the histogram of a work function image can be utilized. This procedure is now discussed for the example shown in Fig. 4.6.
Fig. 4.6 (a) displays the work function image of a $CuInSe_2$ (CIGSe) thin film[3], in which three different work function domains can be distinguished. The white (Φ_3) and green (Φ_2) areas correspond to different surface facets on the CIGSe surface (see Sec. 2.1.2), while the origin of dark domain in the upper left corner (Φ_1) is not understood (see Sec. 6.1).
Fig. 4.6 (b) shows the histogram of the work function image in Fig. 4.6 (a). Three distinct peaks are visible. They correspond to the three different work function domains Φ_{1-3}. In order to extract the discrete work function values of the domains from the histogram, the histogram is fitted with three Gaussian distributions. The maximum of each Gaussian distribution represents the work function value of one of the discrete domains. The full width half maximum (FWHM) of each distribution can be regarded as a measure for the variation of the work function within the specific domain. With this procedure one obtains the work function values of the three domains in Fig. 4.6 (a) as:

$$\Phi_1 = (4.70 \pm 0.03)\text{eV},$$

$$\Phi_2 = (4.97 \pm 0.04)\text{eV},$$

$$\Phi_3 = (5.06 \pm 0.02)\text{eV}.$$

Here, one should emphasize again that the given $\pm$ values represent actual variations in the measurements (FWHM of Gaussian distribution), and not a measurement inaccuracy.

In the course of this thesis the Gaussian distribution with the highest number of events is used for the determination of the average work function of a surface.

[3]This image will be discussed in more detail in Sec. 7.

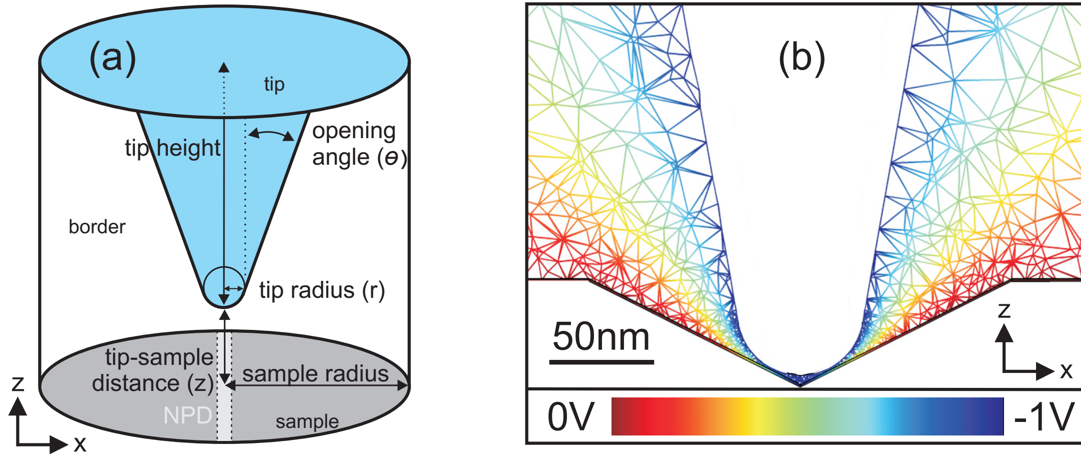

Figure 4.7: *(a) Input geometry used for the FEM simulations. The nanoscale potential distribution (NPD) along the y-axis was implemented for the simulations shown in Chap. 5 (see Sec. 5.1.2). (b) Cross section through a 3D FEM simulation displaying the electrostatic potential distribution between tip and sample in case of a nanoscale potential distribution, which is located at the center of a valley-like topography (200nm wide, 50nm deep). For simulation parameters see Tab. A.1.*

4.1.4 Simulation of the tip-sample interaction in KPFM

By means of a simulation-tool, which reproduces the tip-sample interaction in Kelvin probe force microscopy (KPFM), it becomes possible to systematically and independently study the influence of various KPFM parameters (e.g. tip geometry, potential distribution on the surface) on the measurement results. It is generally tedious to access similar information experimentally. Consequently, KPFM simulations provide a powerful means to improve the general understanding of the physics behind KPFM, and allow for a better interpretation of experimental KPFM results.
The KPFM simulation, which is introduced in this section, reproduces the force interaction between tip and sample in AM-KPFM (see Sec. 4.1.2.2). It was developed by Caspar Leendertz in the framework of his diploma thesis [141, 142], and modified in the framework of this thesis in order to reproduce Kelvin probe force spectroscopy experiments, as described in Chap. 5.

In AM-KPFM a minimization of the electrostatic force between tip and sample is utilized for the determination of the contact potential difference (CPD). Consequently, the challenge of this simulation is to determine the electrostatic force between tip and sample, and from this the CPD.
At first, the electrostatic potential distribution $\phi(x, y, z)$ between tip and sample is determined. For this purpose a commercial finite element method (FEM) program which can solve the Laplace equation

$$\Delta\phi(x, y, z) = 0 \tag{4.13}$$

for a given 3D geometry is employed.

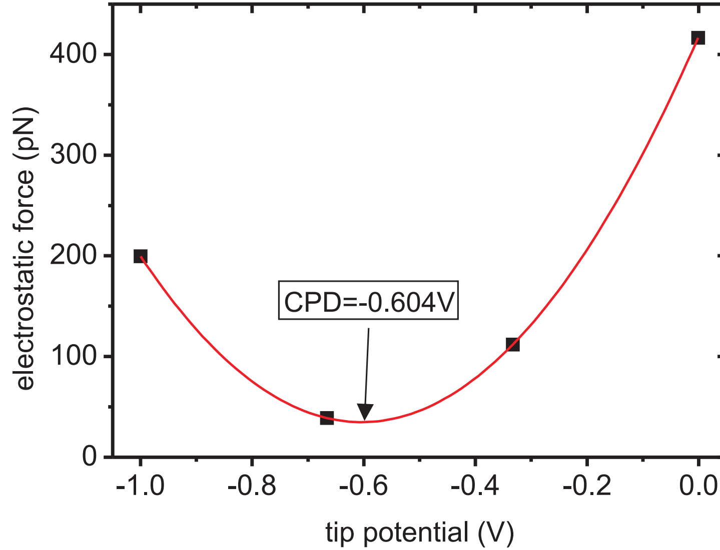

Figure 4.8: *The quadratic dependence between tip potential and electrostatic force (see Eq. (4.7)) in case of the geometry shown in Fig. 4.7 (b). The tip potential, which corresponds to the minimum of the parabola, matches the CPD between tip and sample. For simulation parameters see Tab. A.1.*

A schematic of the 3D geometry, which is implemented in the KPFM simulation, is depicted in Fig. 4.7 (a). The tip is modeled as a metallic cone with a spheric tip-apex. The height of the tip was kept constant at 13μm for all simulations, while the tip's opening angle θ and the radius r of the tip-apex were variable parameters. At its upper end the tip is connected to a circular metallic plate with a constant radius of 12.5μm. The sample is located at a variable tip-sample distance z away from the tip-apex. It is also modeled as a circular metallic plate with a constant radius of 12.5μm, oriented parallel to the plate which confines the tip.
Boundary conditions for the tip potential, the sample potential, and the border of the implemented geometry were predefined, in order to be able to solve the Laplace equation:

$$\begin{aligned} \Gamma_{tip}: &\quad \phi = \phi_{tip}, \\ \Gamma_{sample}: &\quad \phi = \phi_{sample}(x,y), \\ \Gamma_{border}: &\quad \mathbf{n}\cdot\nabla\phi = 0, \end{aligned}$$

where $\mathbf{n}$ is the normal vector of the border-area.

As solution for the Laplace-equation (Eq. (4.13)) one obtains the 3D distribution of the electrostatic potential between tip and sample. An exemplary cross section through such a potential distribution is shown in Fig. 4.7 (b).
From the electrostatic potential distribution the electric field distribution $\mathbf{E}(x,y,z)$ between tip and sample is calculated via Eq. (4.14).

$$\mathbf{E}(x,y,z) = -\nabla\phi(x,y,z). \tag{4.14}$$

The electrostatic force F_{el} between tip and sample can be calculated directly from $\mathbf{E}$:

$$F_{el} = \frac{\epsilon_0}{2} \int_{\Gamma_{tip}} ds \, |\mathbf{E}| \, E_z, \tag{4.15}$$

where E_z is the z-component of the electric field $\mathbf{E}$.

In order to determine the contact potential difference between tip and sample, the force F_{el} is calculated for various tip potentials ϕ_{tip}. Since there is a quadratic dependence between the potential difference between tip and sample and the resulting electrostatic force (see Eq. (4.7)), the obtained data points can be fitted with a parabola. In Fig. 4.8 this is shown exemplarily for the geometry seen in Fig. 4.7 (b). The minimum of the parabola matches the contact potential difference, as this tip-potential minimizes the force between tip and sample.

4.2 Scanning electron microscopy (SEM)

In scanning electron microscopy (SEM) a focused electron beam is employed to gather a variety of information about a sample of interest. The electron beam is usually created by a field emission gun and accelerated towards the sample by an electric field. Typical electron energies are in the range of several keV, depending on the specific application. A series of electromagnetic lenses is employed to focus the electron beam to probe-diameters of < 1nm. A scanning coil accounts for the lateral motion of the electron beam across the sample, and thereby enables SEM imaging.
In general, one can distinguish two fundamental methods of data acquisition in SEM. The first method is based on the utilization of secondary electrons to collect information about a sample, while the second method employs backscattered electrons to gather information. Due to the different properties of secondary and backscattered electrons, a large variety of information is accessible by means of SEM.
In the following, we will only briefly discuss the SEM methods which are relevant for this thesis. For a comprehensive introduction to the broad field of scanning electron microscopy the textbooks of Reimer [143] and Abou-Ras et al. [144] are recommended.

4.2.1 SEM topography imaging

Scanning electron microscopy (SEM) topography imaging provides a means to obtain 2D topography images of various objects (e.g. surface structures, KPFM tips, etc.) with a resolution down to the nm range. Unlike atomic force microscopy imaging (see Sec. 4.1.1), SEM topography imaging does not utilize a cantilever to collect its information, but it rather employs secondary electrons (SEs) for the imaging process [144]. This allows for the study of objects with rough surface topographies, on which scanning probe microscopy techniques are only hard to apply[4]. Additionally, SEM topography imaging facilitates a large flexibility in image size, ranging from the nanometer scale up to several 100s of μm.

[4]Mainly due to limitations in range and speed of the z-piezo.

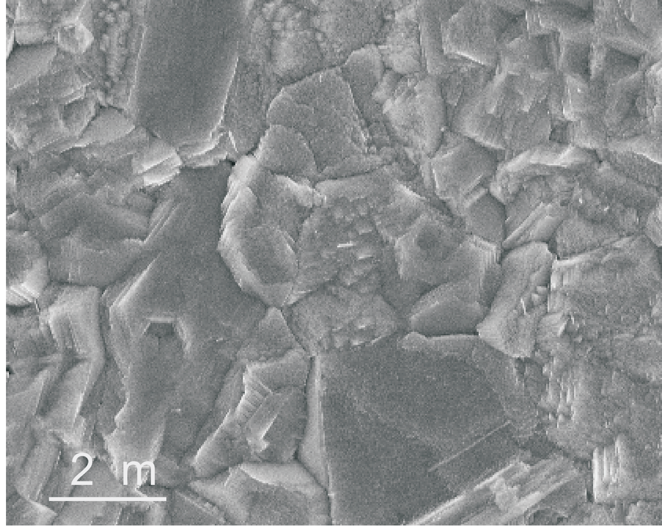

Figure 4.9: *SEM micrograph of a polycrystalline $CuInSe_2$ thin film. This image will be discussed in more detail in Sec. 7.*

SEs are created inside a sample by the incident electron beam of the SEM. SEs which emerge from the sample are collected by a positively biased collector grid located in the vicinity of the sample. Subsequently, they are accelerated on a scintillator layer in front of a photomultiplier for detection.
Due to their low energies (E_{SE} <50eV), SEs have a small exit depth of only a few nanometers. This high surface sensitivity, combined with the fact that the SE yield depends on the orientation of a given surface element, makes SEs an ideal tool for 2D topography imaging.

The information gathered by means of SEM topography imaging is usually illustrated with the help of a gray scale image, the so called SEM "micrograph". In Fig. 4.9 a typical SEM micrograph of a polycrystalline $CuInSe_2$ (CIGSe) thin film is depicted as example. One can clearly notice a granular structure typical for CIGSe thin films. Additionally, different surface facets can be distinguished in the image as well.

4.2.2 Electron backscatter diffraction (EBSD)

Electron backscatter diffraction (EBSD) employs backscattered electrons (BSEs) to determine the crystal symmetry and orientation in a polycrystalline thin film of interest [144].
BSEs (E_{BSE} > 50eV) are emitted in all directions, if the electron beam of the scanning electron microscope (SEM) hits the sample. Some of the BSEs fulfill the Bragg-condition

$$n\lambda = 2d_p sin(\eta) \tag{4.16}$$

for a specific set of atomic lattice planes in the crystals. Here, n is an integer, λ is the wavelength of the incident electron beam, d_p is the spacing between the planes in the atomic lattice, and η is the Bragg angle. These electrons are diffracted towards a planar

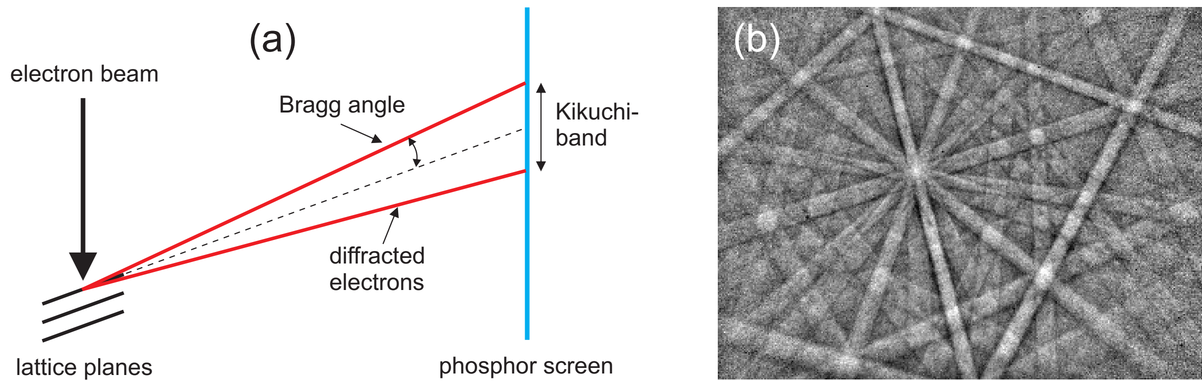

Figure 4.10: *(a) Schematic illustration of the formation of Kikuchi-bands in EBSD (modified from [145]). (b) Kikuchi-pattern obtained on a polycrystalline CIGSe thin film [146].*

detector, where they form a so called "Kikuchi"-band, as illustrated in Fig. 4.10 (a). BSEs are diffracted by many different sets of atomic planes within a thin film, which results in a variety of Kikuchi-bands. The entirety of these bands creates a characteristic diffraction pattern, the so called Kikuchi-pattern, which acts as a "finger print" for the local orientation distribution of a thin film. An exemplary Kikuchi-pattern of a $Cu(In,Ga)Se_2$ (CIGSe) thin film is shown in Fig. 4.10 (b). By comparison of the experimentally obtained Kikuchi-pattern with theoretically calculated Kikuchi-patterns from a database it is possible to determine the crystal orientations of the various grains inside a thin film with respect to a reference coordinate system with a lateral resolution down to the nm range. Based on the information about the orientation of the individual grains, one can additionally gain insights about the symmetry of the grain boundaries (GBs) between these grains. By means of EBSD it is possible to distinguish between highly symmetric $\Sigma3$ GBs and lower symmetric non-$\Sigma3$ GBs (see Sec. 3.1).

The information gathered by means of EBSD is usually illustrated with the help of "EBDS orientation distribution maps" and "EBSD pattern quality maps":

- **EBSD orientation distribution map:** An EBSD orientation distribution map illustrates the crystalline orientation of the various grains inside a polycrystalline thin film with the help of a color code.
- **EBSD pattern quality map:** An EBSD pattern quality map is a gray-scale image, in which the sharpness of the diffraction bands in the corresponding Kikuchi-pattern is illustrated in real-space. GBs can be noticed in pattern quality maps as dark lines, since the EBSD pattern of two grains superimpose at a GB. This results in zero resolution and therefore very low gray values [144].
  In all EBSD pattern quality maps depicted in this thesis $\Sigma3$ GBs (see Sec. 3.1) are highlighted by solid red lines.

Chapter 5

Kelvin probe force microscopy at nanoscale potential distributions

All atomic force microscopy (AFM) methods use the tip at the end of a cantilever as sensor to obtain spatially resolved information about the properties of a surface (see Sec. 4.1). Consequently, the maximum lateral resolution in such measurements is mainly determined by the dimension of that segment of the tip which contributes significantly to the total interaction signal between tip and sample. For example, to achieve true atomic resolution in AFM it is necessary that the foremost atom of the tip-apex contributes significantly to the total imaging signal [147]. If a larger tip-segment contributes strongly to the imaging signal, the spatial information from the individual surface atoms is averaged out, and the atomic resolution is lost.
Kelvin probe force microscopy (KPFM) measurements of electrostatic potential distributions that are confined to the nanometer range ("nanoscale potential distributions") are subject to a similar averaging effect [136, 142, 148–151]. The comparably large tip-

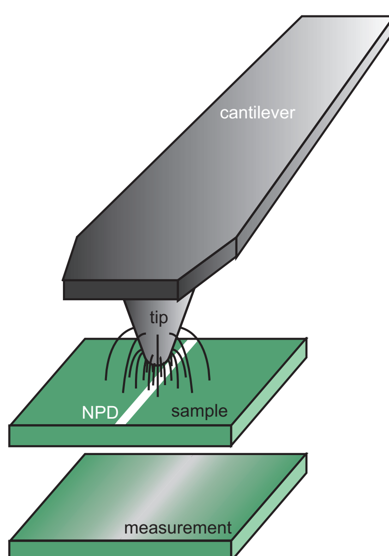

Figure 5.1: *Schematic of a KPFM measurement at a nanoscale potential distribution illustrating the averaging effect of the work function signal.*

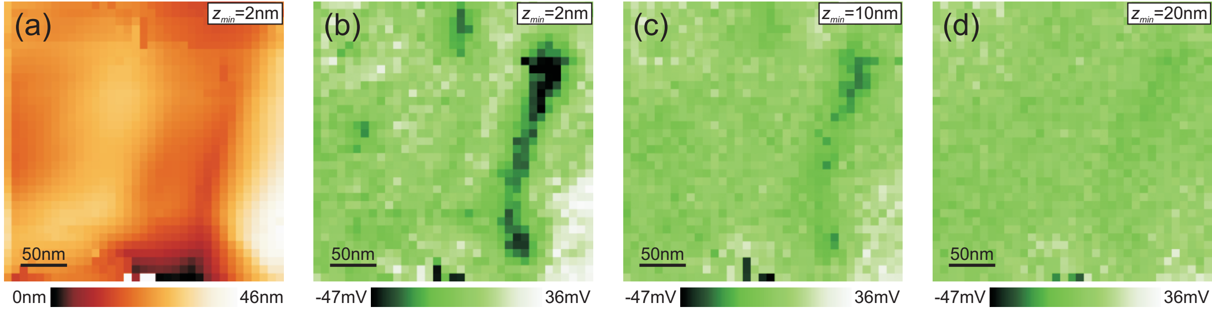

Figure 5.2: *300nm × 300nm KPFS images (35pts×35pts grid) of topography and contact potential difference (CPD) at a grain boundary of a* $CuIn_{0.7}Ga_{0.3}Se_2$ *thin film. (a) Topography image at a tip-sample distance* z_{min}*=2nm. Simultaneously recorded contact potential difference image at (b)* z_{min}*=2nm, (c)* z_{min}*=10nm, and (d)* z_{min}*=20nm. A "plane"-filter was applied to all CPD images for better comparison.*

sample distance in cantilever-based KPFM (several nanometers) in combination with the long range nature of the electrostatic forces result in a rather large tip-segment contributing to the KPFM imaging signal. Consequently, even if the tip is located directly above the center of a nanoscale potential distribution (NPD), the KPFM imaging signal is not solely obtained from inside the NPD, but also from the adjacent surface area. This "averaging effect", which is illustrated in Fig. 5.1, causes a decrease of the NPD work function signal detected in KPFM.

The focus of this thesis is to study the electronic properties of grain boundaries (GBs) in polycrystalline Cu(In,Ga)Se_2 (CIGSe) thin films. GBs in these materials frequently show different electronic properties in comparison to the grains, whereat such variations are confined to the nanometer range [10, 100]. Consequently, KPFM studies on the electronic properties of GBs in CIGSe are also subject to the averaging effect of the KPFM imaging signal.
In Fig. 5.2 Kelvin probe force spectroscopy (KPFS) images[1] illustrate the dimension of the averaging effect in the case of an electronically active GB in CIGSe. Fig. 5.2 (a) shows the topography image obtained at a tip-sample distance z_{min}=2nm. In the image one can detect a valley-like texture. This is a typical topography feature of a transition between two grains in CIGSe, i.e. a GB. Figs. 5.2 (b)−(d) display the contact potential difference (CPD) images of the identical location, obtained at different tip-sample distances z_{min} of 2nm, 10nm, and 20nm. From these images it becomes obvious that the averaging effect strongly influences the KPFM imaging signal in dependence of the tip-sample distance. While for a tip-sample distance of 2nm the electronic contrast of the NPD at the GB (lower work function than surrounding area) can be clearly distinguished, the NPD contrast is already significantly averaged out at z_{min}=10nm. At a tip-sample distance of 20nm the NPD can not be identified anymore in the CPD image[2].
As can be seen from Fig. 5.2, work function signals of nanoscale potential distributions de-

[1] 1225 KPFS spectra were taken on a 35pts×35pts grid around the GB of interest. Images were reconstructed from the entirety of the single spectra (see Sec. 5.1 for details about KPFS).
[2] Note that the NPD can still be identified in the image at z_{min}=20nm, if the CPD range is adjusted appropriately.

tected in KPFM measurements are subject to a significant averaging effect. Consequently, for any quantitative comparison of KPFM results obtained at NPDs to results from other experimental techniques or theory an estimate of the magnitude of the averaging effect is required.

This chapter investigates the averaging effect of the work function signal of nanoscale potential distributions in Kelvin probe force microscopy by means of Kelvin probe force spectroscopy experiments and finite element method simulations. It provides detailed descriptions of both the experimental and the simulation routines. Furthermore, it analyzes how inhomogeneities in the work function distribution of both the KPFM-tip and the sample surface influence KPFS measurements. An experimental approach is developed which avoids any effect of such inhomogeneities on the experimental results. With this approach the averaging effect of work function signals of nanoscale potential distributions in Kelvin probe force microscopy is studied quantitatively in dependence of the geometry parameters of the experimental setup (i.e. tip geometry, the width of a nanoscale potential distribution, tip-sample distance, and surface topography), to provide a means to estimate the magnitude of the averaging effect for given experimental setups.

5.1 Kelvin probe force spectroscopy (KPFS)

The averaging effect of nanoscale potential distributions in Kelvin probe force microscopy (KPFM) was experimentally studied by means of Kelvin probe force spectroscopy (KPFS). Both methods, KPFM and KPFS, are different modes of operation within the same experimental setup (see Sec. 4.1.3.1). They rely on the same physical principles (see Sec. 4.1), and gather identical information[3].
Whereas in KPFM the tip is scanned across a sample surface at a constant tip-sample distance in order to record images of surface topography and work function distribution, in KPFS the sample is retracted from the tip in z-direction with the x-y coordinates of the sample kept constant. While the sample is retracted, the various parameters of a KPFM measurement (frequency shift Δf, contact potential difference between tip and sample, excitation voltage of the driving piezo, oscillation amplitude of the cantilever, etc.) can be monitored.

This section describes the experimental routine of KPFS experiments at nanoscale potential distributions in detail. It introduces the applied approach to model such experiments with finite element method simulations. Furthermore, it discusses why Kelvin probe force spectroscopy is better suited for the purpose of this study than regular Kelvin probe force microscopy.

[3] An elaborate comparison of KPFM and KPFS experiments at nanoscale potential distributions can be found in Sec. A.1.

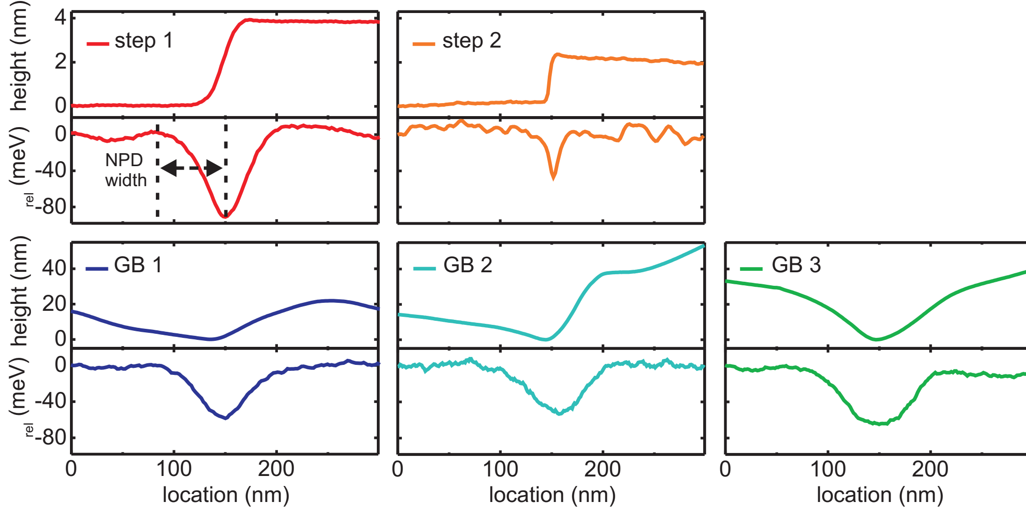

Figure 5.3: *KPFM line profiles of topography and relative work function (Φ_{rel}) across the various NPDs studied, taken at the tip-sample distances z_{min} stated in Tab. 5.1. All work function line profiles were shifted in such a way that Φ_{rel} outside the NPD is at 0.*

5.1.1 KPFS experiments at nanoscale potential distributions

Sample details

All experiments reported within this chapter were performed on two different material systems; monocrystalline ultra high vacuum (UHV)-cleaved p-type GaAs(110), and polycrystalline $CuIn_{0.7}Ga_{0.3}Se_2$ (CIGSe) thin films. The GaAs(110) surface exposes many surface steps ($\approx$1 step/μm^2 in our experiments), due to the cleavage. At the step-edges positive charges accumulate and lower the work function [113]. Grain boundaries (GBs) of CIGSe, on the other hand, frequently show different electronic properties as the bulk of the material, presumably due to the presence of localized, charged surface states [10, 100]. The frequent appearance of nanoscale potential distributions (NPDs) on both material systems makes them ideal model systems for our study.

Table 5.1: *Overview of various properties of the different NPDs investigated within this chapter. Both the NPD work function signal ($\Delta\Phi = \Phi_{NPD} - \Phi_{Background}$) and the NPD width ($w$) were determined from Fig. 5.3. The tip sample distances z_{min} and z_{eff} were obtained based on z-spectroscopy experiments, as described in the next section.*

Acronym:	**step 1**	**step 2**	**GB 1**	**GB 2**	**GB 3**
Material:	GaAs(110)	GaAs(110)	CIGSe	CIGSe	CIGSe
Type:	p-type	p-type	p-type	p-type	p-type
Topography:	step-like	step-like	valley-like	valley-like	valley-like
$\Delta\Phi$ (meV):	-90±5	-47±5	-58±5	-53±5	-65±5
w (nm):	65±5	20±5	65±5	60±5	65±5
z_{min} (nm):	2.7±0.2	0.9±0.2	2.2±0.2	2.2±0.2	4.7±0.2
z_{eff} (nm):	7.7±0.2	5.9±0.2	7.2±0.2	7.2±0.2	9.7±0.2

In total, 5 different NPDs were investigated in the course of this study. Two NPDs at step-edges of differently doped p-type GaAs(110) (from now on called "*step 1*", and "*step 2*"), and three different, electronically active GBs in CIGSe (from now on called "*GB1*", "*GB 2", and "GB 3")*. Kelvin probe force microscopy (KPFM) line profiles of both topography and work function across the various NPDs are displayed in Fig. 5.3. In Tab. 5.1 an overview of various properties of the NPDs is provided.

The tip-sample distances z_{min} and z_{eff}

In Kelvin probe force microscopy (KPFM) and Kelvin probe force spectroscopy (KPFS) experiments the tip-sample distance is controlled with the help of the frequency shift Δf of the cantilever (see Sec. 4.1.1). During a KPFM measurement Δf is kept at a predefined setpoint to maintain a constant tip-sample distance. In a KPFS experiment, on the other hand, the smallest tip-sample distance, from which the z-sweep starts, is defined by a Δf setpoint. In order to convert the frequency shifts Δf to absolute tip sample distances a calibration measurement is required.

- $\mathbf{z_{min}}$: The minimum tip-sample distance z_{min} is the smallest distance between tip and sample during an oscillation period of the cantilever at a predefined frequency shift Δf. The absolute value of z_{min} can be determined by means of z-spectroscopy. In z-spectroscopy the tip-sample distance is, starting from z_{min}, successively decreased. With decreasing tip-sample distance the force interaction between tip and sample increases. This leads to a decrease of Δf, as can be seen in Fig. 5.4 (a). The zero-point of the minimum tip-sample distance is determined by the onset of a strong damping signal, which originates from an energy dissipation caused by the occurrence of short-range atomic forces between tip and sample (see Sec. 4.1.1). The damping induces a decrease in cantilever oscillation amplitude and an increase in cantilever excitation voltage, as can be noticed in Fig. 5.4 (b) and (c).
  Based on the zero-point of the minimum tip-sample distance it is possible to calibrate the arbitrary scale z_{rel} of the z-piezo to an absolute scale, which corresponds to z_{min}. From a calibrated z_{min} vs. Δf curve one can read off the minimum tip-sample distance z_{min} for any given frequency shift Δf. In Fig. 5.4 (a), for example, a frequency shift of -15Hz corresponds to a minimum tip-sample distance z_{min} of 2.7nm.

- $\mathbf{z_{eff}}$: The minimum tip-sample distance z_{min} is a function of the oscillation amplitude of the cantilever. In order to enable a comparison among various KPFM experiments and to theory independent of the used oscillation amplitude the effective tip-sample distance z_{eff} is employed. It is defined as the tip-sample distance at which the same KPFM-results are obtained as at z_{min}, but with a hypothetical cantilever oscillation amplitude of 0nm.
  In Refs. [141, 152] the concept of the effective tip-sample distance is described in more detail, and values of z_{eff} are provided for various z_{min}.

Within this chapter purely experimental data is plotted against z_{min}, if not stated otherwise. If a combination of experimental and simulation data is used in a graphics, it is

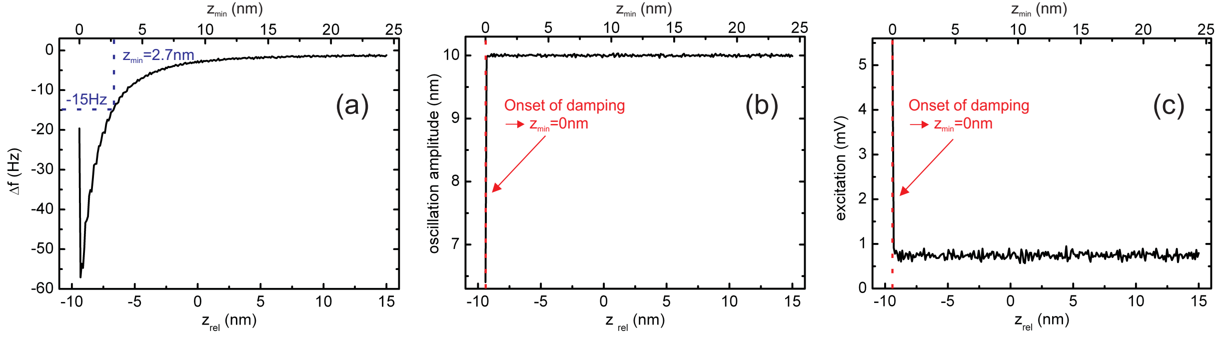

Figure 5.4: *z-spectroscopy to determine an absolute tip-sample distance. (a) Tip-sample distance vs. frequency shift Δf. The minimum tip-sample distance $z_{min}(-15Hz)$ is indicated by a blue, dashed line. (b) Tip-sample distance vs. oscillation amplitude of the cantilever. (c) Tip-sample distance vs. excitation voltage of the driving piezo. In all graphics the lower x-axis displays the relative z-scale z_{rel} of the tip-sample distance, with an arbitrary reference point $z_{rel}(-3Hz) = 0$. The upper x-axis displays the absolute z-scale z_{min}, for which the onset of damping due to short range atomic forces is the reference point (indicated in (b) and (c) by red, dashed lines).*

plotted against z_{eff} to enable comparison between experiments and simulations[4].

One should note that the procedure of converting the z-axis of a KPFS experiment from z_{min} to z_{eff} causes an inaccuracy in z_{eff} for large tip-sample distances, as the effective tip-sample distance slightly depends on z_{min}, which is not considered in the conversion[5]. However, with respect to the course of all experimental KPFS spectra recorded within this study (constant for large tip-sample distances), no effect of this inaccuracy on the experimental results is expected.

KPFS to study the averaging effect

To study the averaging effect of work function signals of nanoscale potential distributions (NPD), Kelvin probe force spectroscopy (KPFS) offers several advantages over the regular Kelvin probe force microscopy (KPFM) technique while gathering identical information (see Sec. A.1).
First, the range of tip-sample distances accessible by KPFS exceeds the one accessible by KPFM by far. This originates from the fact that for KPFS experiments the tip-sample distance is controlled by the expansion of the z-piezo[6]. Only for the smallest tip-sample distance of a spectroscopy, the tip-sample distance is determined by the frequency shift Δf of the cantilever. Starting at this minimum tip-sample distance z_{min} the sample is continuously retracted from the tip by the z-piezo. Consequently, the range of tip-sample distances accessible by KPFS is identical to that of the z-piezo. For the used KPFM

[4] A constant cantilever oscillation amplitude of 10nm was used for all experiments, while no cantilever oscillation was considered in the simulations (i.e. $z_{min} = z_{eff}$ in case of the simulations).

[5] For the conversion to z_{eff} a constant offset, which is based on z_{min}, is added to the KPFS tip-sample distance data.

[6] In general, more than one piezo is involved in moving the sample. For clarity, only the direction of the resulting motion is denoted.

setup (see Sec. 4.1.3.1) it is 2μm.
In KPFM measurements, on the other hand, the tip-sample distance is always controlled by the frequency shift Δf (see Sec. 4.1.1). The range of accessible tip-sample distances is therefore limited to distances, for which it is possible to maintain a constant z_{min} via Δf. As can be seen in Fig. 5.4 (a), the characteristics of the z_{min} vs. Δf curve displays only a very moderate slope for larger tip-sample distances. This generates an uncertainty in the determination of the tip-sample distance via Δf, which eventually limits the range of tip-sample distances accessible by KPFM. With our KPFM setup, depending on the properties of the used cantilever, maximum tip-sample distances around 15nm$-$30nm are accessible.

A second advantage of KPFS over KPFM, which comes side by side with the first one, is the easier and more precise determination of the absolute tip-sample distance. In KPFM the absolute tip-sample distance has to be determined individually for every single Δf setpoint, while in KPFS the absolute tip-sample distance only needs to be determined once (for the minimum tip-sample distance z_{min}) based on the frequency shift Δf. For all other tip-sample distances the absolute z-distance is simply determined by adding the relative expansion of the calibrated z-piezo during the sweep to the minimum tip-sample distance z_{min}. This procedure facilitates a quicker measurement and a higher density of data points in z-direction compared to KPFM.
Additionally, the determination of absolute tip-sample distances is very precise in KPFS, as for small tip-sample distances the slope of the z_{min} vs. Δf curve is rather steep. This enables an accurate determination of z_{min}. At $\Delta f = -15$Hz in Fig. 5.4 (a), for example, the tip-sample distance can be determined with an inaccuracy of $\approx$ 0.2nm. Since the expansion of the z-piezo is also highly accurate, each tip-sample distance can be determined with high precision in KPFS experiments.

Experimental routine

In order to study a nanoscale potential distribution (NPD) by means of Kelvin probe force spectroscopy (KPFS), the area around the NPD is first imaged by regular Kelvin probe force microscopy (KPFM). The same Δf setpoint that is later used for the KPFS measurements is employed. The orientation of the KPFM scan is adjusted in such a way that the direction of the fast scan axis (x-axis) of the KPFM is perpendicular to the orientation of the NPD, as can be seen exemplary in Fig. 5.5 (a). After several KPFM images are taken at this position and the drift of the x-y-z-piezos is minimized, a pathway is defined along which KPFS spectra[7] will be recorded. A schematic pathway is indicated in Fig. 5.5 (a) by blue crosses. $80 - 120$ spectra are normally recorded along such a pathway, to ensure a high density of spectra at the center of the NPD of interest.
The parameters which were used for all KPFS measurements within this thesis can be found in Sec. A.2.

Since all spectra along a pathway are recorded one after the other, one needs to assure that the single spectra do not affect each other. The most critical aspect is an influence of z-piezo creep on the spectra. It could be induced by the permanently changing direction of motion of the z-piezo during the KPFS experiment. Fig. 5.5 (b) shows two KPFS

[7]KPFS spectra: KPFS contact potential difference (CPD) spectra or KPFM work function (Φ) spectra.

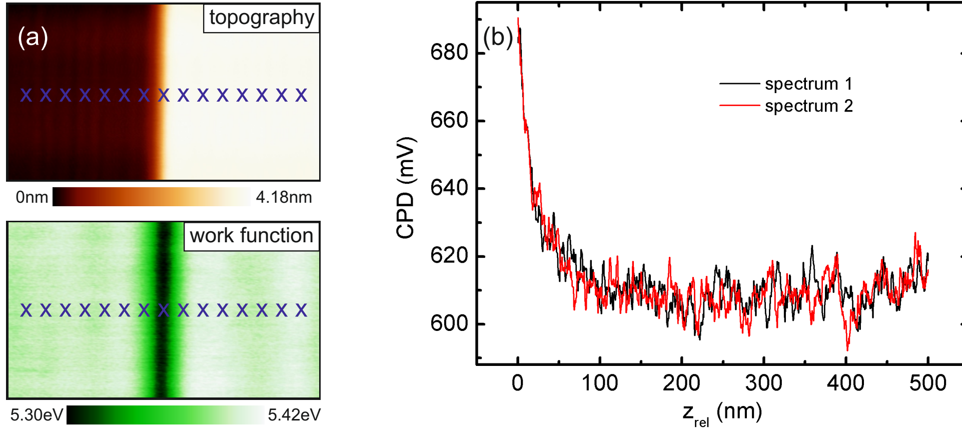

Figure 5.5: *(a) 500nm×5nm KPFM images of topography and work function, recorded at the GaAs(110) surface step 1. The work function image yields an NPD directly at the step-edge. The blue crosses indicate a schematic pathway for a KPFS study of the NPD. (b) Two KPFS contact potential difference (CPD) spectra, taken one after the other at the same position on the GaAs(110) surface of step 2. No influence of piezo-creep can be noticed, as both spectra are nearly identical.*

spectra, recorded one after the other at the same surface position on the GaAs(110) surface of *step 2*. While spectrum 1 was recorded after the tip had been stabilized at z_{min} for several minutes, spectrum 2 was recorded immediately after spectrum 1 had finished. Nevertheless, the distance dependence of the contact potential difference (CPD) in both spectra is nearly identical. Consequently, one can exclude an influence of z-piezo creep on the KPFS experiments.

For the analysis of KPFS experiments at NPDs four KPFS spectra from similar sample positions (at NPD/away from NPD) were averaged to reduce the noise level. KPFS spectra taken at the center of a NPD were identified by comparison to the KPFM images from the same area, which were taken prior to the KPFS experiments. Since these KPFM images were taken at the same Δf setpoint as the KPFS spectra, one can identify the KPFS spectra at the NPD, as they yield, for the minimum tip-sample distance, the same work function as the KPFM measurements at the NPD.
This procedure is explained exemplary in Fig. 5.6. In Fig. 5.6 (a) KPFM line profiles across *step 1* are displayed. The KPFM images corresponding to these line profiles are shown as insets. The work function line profile reveal a work function of 5.31eV at the center of the NPD, and an average work function value of 5.40eV in the surrounding area. These values are in good agreement with the KPFS experiments at the NPD shown in Fig. 5.6 (b). The blue spectrum taken at the center of the NPD at *step 1* also yields a work function of 5.31eV for its minimum tip-sample distance. With increasing tip-sample distance the work function increases up to 5.40eV, where it saturates. This behavior of the spectrum is a clear evidence for a distance dependent averaging effect of the work function signal from the NPD. In contrast, the red spectrum, which was taken about 150nm laterally away from the NPD in the so called “background”, displays a constant work function of 5.40eV, independent of the tip-sample distance. The constant course of the background-spectrum suggests that the distance dependence of the spectrum at the NPD is solely caused by averaging.

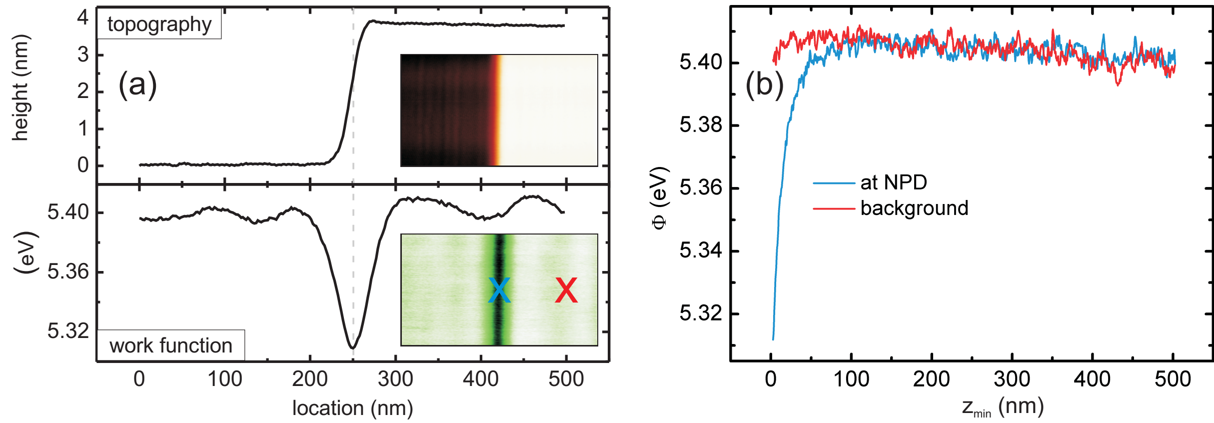

Figure 5.6: *(a) KPFM line profiles (10 lines averaged) of topography and work function (Φ) across the GaAs(110) surface step 1, taken at a tip-sample distance $z_{min} = 2.7nm$. 500nm×5nm images of the corresponding surface area are shown as insets. (b) KPFS work function spectra taken at step 1, starting at a tip-sample distance $z_{min} = 2.7nm$. The blue spectrum was taken at the center of the NPD, while the red spectrum was taken in the background, as indicated in the insets of (a) by blue and red crosses.*

In order to extract the pure work function signal of a NPD from KPFS measurements, the background spectrum was subtracted from the spectrum taken at the center of a NPD. For the example discussed in Fig. 5.6 (b) this may seem superfluous, as the background spectrum is nearly constant. But in general one can not expect a constant background spectrum in KPFS experiments, as inhomogeneities of both KPFM-tip and sample surface can induce fluctuations to KPFS spectra. In this case, which is discussed in detail in Sec. 5.2, it is mandatory to subtract the background spectrum from the one taken at the center of a NPD, to avoid an influence of inhomogeneities on the experimental result.

5.1.2 KPFS simulations at nanoscale potential distributions

The averaging effect of nanoscale potential distributions (NPDs) through the tip of the cantilever of a Kelvin probe force microscope was also studied by means of finite element method simulations. The principles of the applied simulations are described in Sec. 4.1.4.

To model the Kelvin probe force spectroscopy experiments described above, the simulations were performed in a way as similar as possible to the experimental routine. NPDs were implemented in the simulation as space charge region-like potential dips (see Fig. 5.7 (a)). Their widths were adjusted to match the experimental data. Two spectra were determined for every simulation; one spectrum directly at the center of the NPD, and a second one 300nm laterally away from the NPD in the background. Both spectra were, identical to the experimental routine, subtracted from each other in order to obtain the pure distance dependence of contact potential difference signal of the NPD.
In Fig. 5.7 (b) two simulated KPFS spectra, taken at the center of a NPD and in its background, are shown as example. The resulting “difference spectrum”[8] obtained from

[8]KPFS difference spectrum = KPFS spectrum at NPD− KPFS spectrum from background.

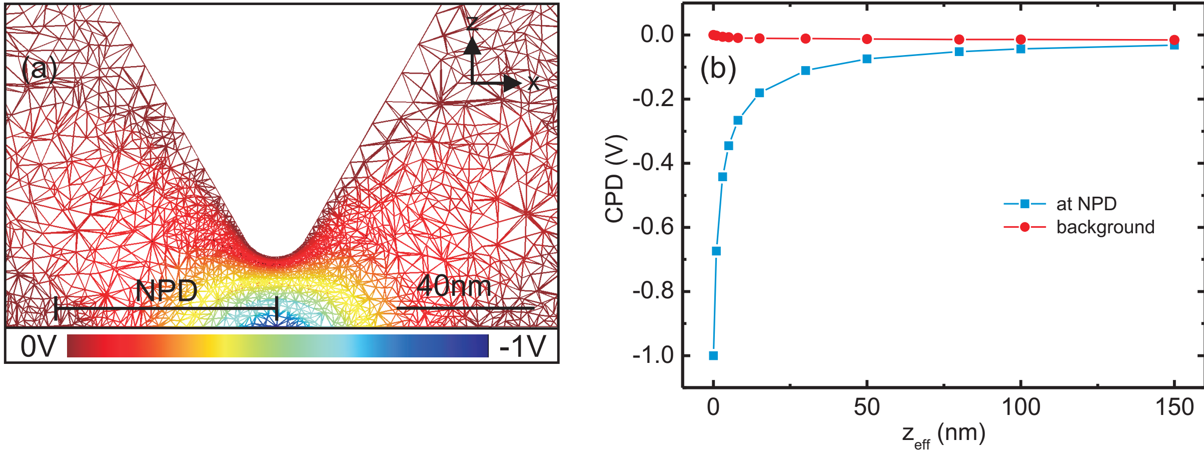

Figure 5.7: *(a) Cross-section of the potential distribution between tip and sample, as determined by means of FEM simulations. The implemented NPD (w=65nm) along the x-axis is clearly visible. (b) Simulated KPFS contact potential difference (CPD) spectra, taken at a NPD (blue squares) and in its background (red dots). For simulation parameters see Tab. A.1.*

the two spectra can bee seen in Fig. 5.13.

5.2 The impact of electronic inhomogeneities on KPFS experiments

In Fig. 5.6 (b) two Kelvin probe force spectroscopy (KPFS) spectra, taken at the center of a nanoscale potential distribution (NPD) and in its background, are displayed. For small tip-sample distances the spectrum at the NPD yields the low work function value of the NPD, while for larger tip-sample distances the work function increases until it saturates at the value of the constant, distance-independent background spectrum. This ideal course of the spectra is similar to that of the simulations in Fig. 5.7 (b). Nevertheless, one can not generally expect such ideal experimental spectra. Electronic inhomogeneities of the used tip can induce fluctuations in the KPFS spectra, as for different tip-sample distances different areas of the tip contribute to the imaging signal. Additionally, inhomogeneities in the work function distribution of the sample surface can cause fluctuations in the KPFS spectra as well, as the surface area averaged by the tip also changes with tip-sample distance. However, inhomogeneities of the sample surface should mainly have an influence for small tip-sample distances, since (not too large) surface inhomogeneities are averaged out for large tip-sample distances, as can be seen in Fig. 5.2.

Fig. 5.8 (a) shows KPFS spectra taken in the background of the five NPDs studied within this chapter (see Tab. 5.1 and Fig. 5.3). The corresponding spectra from the centers of the NPDs are displayed in Fig. 5.8 (b). The spectra of *step 1* show an ideal behavior with tip-sample distance, as discussed above. However, the spectra obtained at all other NPDs show a less ideal behavior. This can be observed in particular in Fig. 5.8 (a). For

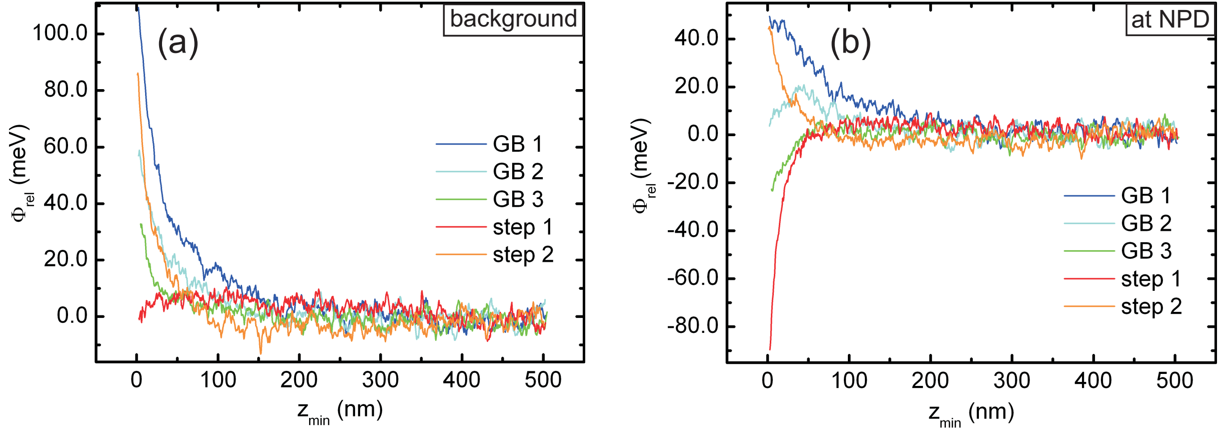

Figure 5.8: *Experimental KPFS spectra taken (a) in the background, and (b) at the center of the various NPDs from Tab. 5.1. All spectra were shifted in such a way that the relative work function signal (Φ_{rel}) for large tip-sample distances is at 0.*

tip-sample distances of up to about 150nm the background-spectra clearly yield deviation from the ideal (constant) behavior with tip-sample distance. With decreasing tip-sample distances the relative work functions (Φ_{rel}) of the spectra increase. This indicates a significant influence of inhomogeneities on the measurements. The influence of inhomogeneities can also be seen in the spectra taken at the NPDs in Fig. 5.8 (b). In the case of *GB 1* and *step 2* the work function behavior of the spectra is even inverted. While a decrease of Φ_{rel} is expected with decreasing tip-sample distance, due to the lower work function of the NPDs compared to the background, both spectra yield an increase of Φ_{rel} for small tip-sample distances. The reason for this inversion is a superposition of the detected imaging signal with fluctuations induced by electronic inhomogeneities.

The fluctuations in the spectra of Fig. 5.8 were mainly caused by an inhomogeneous work function distribution of the used tip. While the measurements at *step 1* were performed with the homogeneous tip 1 shown in Fig. 5.9 (a), all other experiments were conducted with tip 2 shown in the micrographs of Figs. 5.9 (b) and (c). The micrographs clearly reveal a contamination of tip 2. Right at the apex an elliptic particle is attached to the tip. It seems likely that this is a CIGSe particle, which got attached in the beginning of the experiments due to a tip-crash on the rather rough CIGSe material. This contamination can explain the fluctuations observed in the spectra of Fig. 5.8. For small tip-sample distances only the CIGSe particle at the apex of the tip interacted significantly with the surface, and the effective work function of the tip was that of the CIGSe particle. With increasing tip-sample distance a larger tip-segment consisting of both the CIGSe particle and the actual tip contributed to the imaging signal, which shifted the tip's effective work function towards that of the actual tip. This variation of the effective work function in dependence of the tip-sample distance induced fluctuations in the KPFS spectra, as observed in Fig. 5.8 (a) and (b).
Nevertheless, it should be mentioned again that inhomogeneities of the sample surface may have also contributed to the fluctuations in the spectra of Fig. 5.8, especially in case of the inhomogeneous CIGSe samples.

To avoid any influence of electronic inhomogeneities on the distance dependence of the

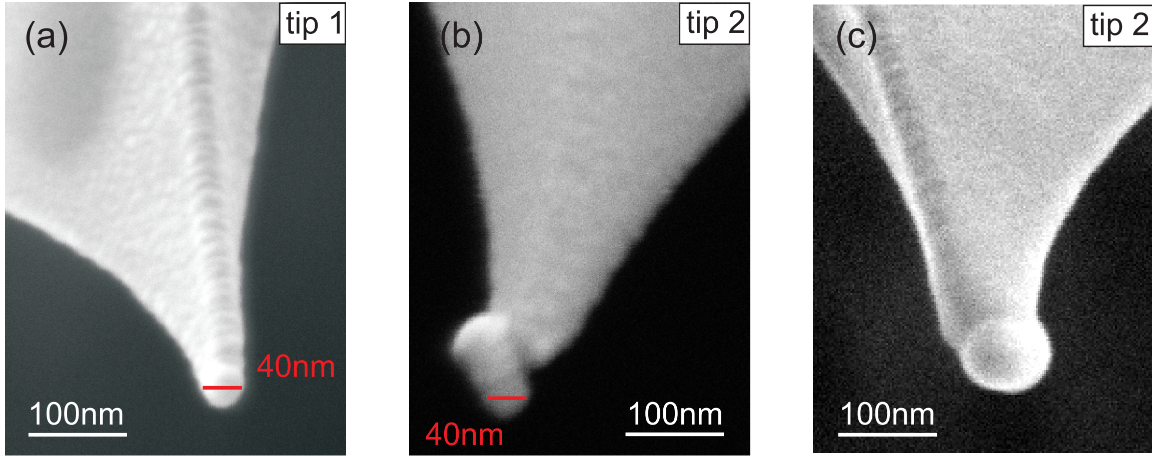

Figure 5.9: *Scanning electron micrographs of the Pt-Ir coated Si tips used in the KPFS experiments. (a) tip 1, and (b), (c) tip 2.*

NPD work function signal obtained by KPFS, it is mandatory to subtract the KPFS background spectrum from the corresponding KPFS spectrum at the center of the NPD. By means of the subtraction the fluctuations in the spectra are canceled out, and the so called "difference spectrum" yields the pure work function signal of the NPD. However, not any arbitrary background spectrum will result in a good and correct difference spectrum. In order to obtain a correct NPD work function signal, two main criteria have to be fulfilled by the background-spectrum:

1. The work function value at the minimum tip-sample distance z_{min} needs to agree with that of Kelvin probe force microscopy (KPFM) measurements in the background, which were performed at the same z_{min}.
2. The KPFS background spectrum has to coincide with the corresponding KPFS spectrum at the center of the NPD for large tip-sample distances.

While criterion 1 guaranties that KPFS experiments yield the correct NPD work function signals similar to KPFM measurements at the NPD, the second criterion ensures that a KPFS difference spectrum decreases to 0 for large tip-sample distances.
If both criteria are satisfied and a KPFS background spectrum is correctly subtracted from the corresponding spectrum at the center of a NPD, one obtains a correct distance dependence of the NPD work function signal independent of electronic inhomogeneities.

5.3 The averaging effect at nanoscale potential distributions

The magnitude of the averaging effect of work function signals of nanoscale potential distributions in Kelvin probe force microscopy experiments is governed by the geometry of the experimental setup. The particular parameters that define the geometry are: tip geometry, width of a nanoscale potential distribution (NPD width), tip-sample distance, and surface topography.
This section investigates the influence of all of these parameters on the averaging effect quantitatively by means of Kelvin probe force spectroscopy in experiment and simulation. The results of this section provide a means to estimate the magnitude of the averaging effect for given experimental setups.

5.3.1 The influence of tip geometry

At first, the influence of tip geometry on the averaging effect of work function signals of nanoscale potential distributions (NPDs) is investigated. For this purpose Kelvin probe force spectroscopy (KPFS) difference spectra were simulated for various tip geometries[9], while all other parameters of the simulation were kept constant.

From the simulation results shown in Fig. 5.10 one can clearly see that the tip geometry influences the averaging effect of NPD work function signals ($\Delta\Phi$). With decreasing radius of the tip-apex the sensitivity of a measurement decreases, and only a lower percentage of $\Delta\Phi$ is detected at an identical tip-sample distance. The tip's opening angle also influences the measurement sensitivity. Here, a smaller opening angle results in an increase in sensitivity. Consequently, a blunt tip with small opening angle is desirable for KPFM measurements at NPDs, as this tip geometry results in highest experimental sensitivity.
Nevertheless, the variations in measurement sensitivity seen in Fig. 5.10 are rather small compared to the noise level of typical KPFS experiments. For example, a significant change in the radius r of the tip-apex from 10nm to 30nm only causes variations in the NPD work function signal in the range of the experimental noise level, if the opening angle θ is kept constant (see Fig. 5.10). Vice versa, the same is true for a 10° variation of the opening angle θ. Within reasonable experimental dimensions only changes in both tip radius and opening angle can cause a significant change in measurement sensitivity, which can be unambiguously detected in experimental KPFS difference spectra.

Since all KPFS experiments within this chapter, and all KPFM experiments within this thesis, were performed using cantilevers from the same manufacturer with similar tip geometry (see Sec. 4.1.3.1), no significant effect of varying tip geometries on the experimental results is expected. Even tip-crashes or the contamination of a tip (e.g. in Fig. 5.9 (b) and (c)) should not alter the measurement sensitivity in such a way that it would be noticeable in the experiments.
Nevertheless, if various cantilevers with significantly different geometry are used in KPFM

[9]The tip geometry is defined by the radius r of the tip-apex, and the tip's opening angle θ (see Fig. 4.7 (a)).

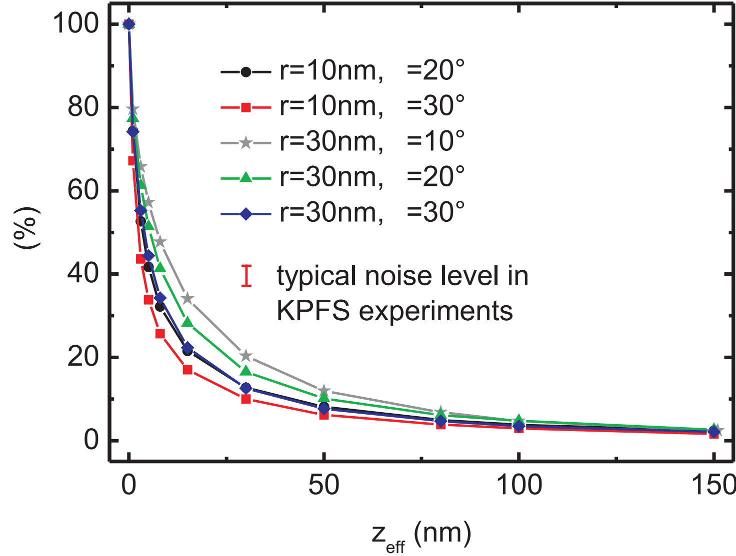

Figure 5.10: *Simulated KPFS difference spectra of the NPD work function signal ($\Delta\Phi$) for various tip geometries (defined by the radius r of the tip-apex, and the tip's opening angle θ). The typical noise level of KPFS experiments (obtained from Fig. 5.15) is indicated by a red error bar. For simulation parameters see Tab. A.1.*

experiments (e.g. cantilevers from different manufacturers), the experimental results obtained at NPDs can differ, depending on the used cantilevers.

5.3.2 The influence of the width of a nanoscale potential distribution

Nanoscale potential distributions (NPDs) have, per definition, a width confined to the nanometer range. The similar dimension of this width, compared to the other geometry parameters of the experimental setup (i.e. tip geometry, tip-sample distance, surface topography), is responsible for the averaging effect. While significantly wider potential variations are not affected by the averaging effect, as the complete Kelvin probe force microscopy (KPFM) imaging signal can be obtained from inside the potential variation (if the tip is located above the center of the potential variation), distinctively smaller potential variations are averaged out completely and not detected at all. Consequently, the question to study within this section is how changes in the width of a NPD within the nanometer range alter the averaging effect.

In Fig. 5.11 (a) two simulated Kelvin probe force spectroscopy (KPFS) difference spectra are shown, for different NPD widths of 20nm (black squares) and 65nm (red dots). All other parameters of the simulations were kept constant. From the difference spectra it is clearly seen that the detectable work function signal increases with NPD width. For example, at an effective tip-sample distance of 15nm only about 8% of the NPD work function signal ($\Delta\Phi$) is detected in case of the 20nm wide NPD, while for the 65nm wide NPD about 17% of the full signal is detected.
The influence of NPD width on the averaging effect becomes even more apparent from Fig. 5.11 (b). There, the simulated work function signal obtained at the center of a NPD at

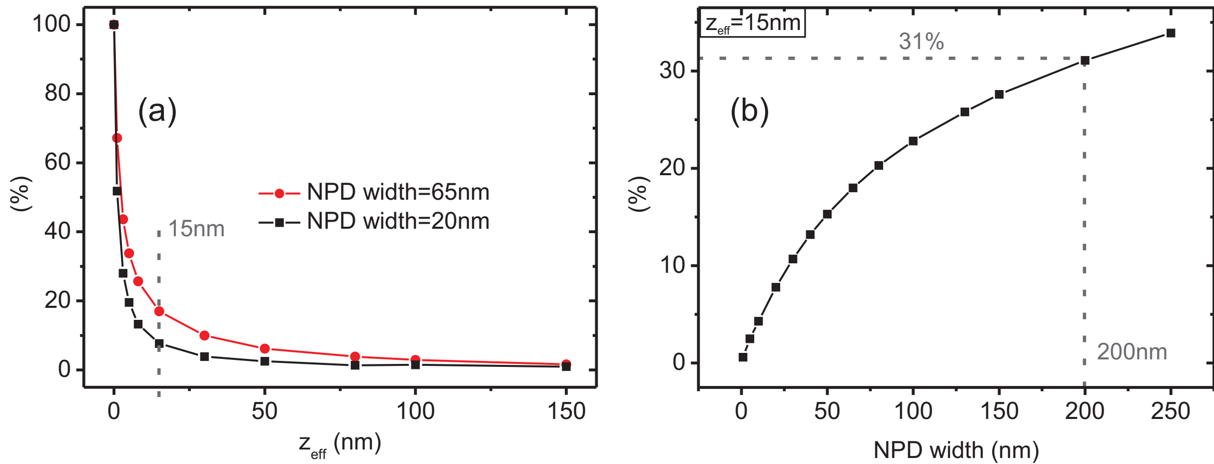

Figure 5.11: *(a) Simulated KPFS difference spectra of the NPD work function signal ($\Delta\Phi$) for NPD widths of 20nm (black squares) and 65nm (red dots). (b) Simulated work function signal obtained at the center of a NPD at z_{eff}=15nm in dependence of the NPD width. For simulation parameters see Tab. A.1.*

a fixed tip-sample distance of z_{eff} = 15nm is plotted as a function of the NPD width. One can unambiguously see an increase in detectable signal percentage with increasing NPD width. Moreover, Fig. 5.11 (b) reveals that even relatively large NPDs are still subject to a significant averaging effect. At the center of a 200nm wide NPD, for example, only 31% of the full signal is detected at a tip-sample distance of 15nm.

The influence of NPD width on the averaging effect was also studied experimentally. For this purpose the averaging effect at *step 1* and *step 2* was investigated by means of KPFS. Both steps exhibit NPDs with different widths of 65nm and 20nm respectively, as can be seen in Fig. 5.3 and Tab. 5.1. The difference in NPD width is caused by a different doping level of the GaAs(110) samples of *step 1* and *step 2*.
In Fig. 5.12 the KPFS difference spectra obtained at both steps are shown. Each of the spectra was normalized at its minimal effective tip-sample distance[10] (see Tab. 5.1), according to the absolute work function signal percentages obtained from the simulation data displayed in Fig. 5.11 (a). Additionally, both difference spectra were smoothed by a 20-point adjacent average for further signal improvement [153].
The same trend that was revealed with the help of the simulations shown in Fig. 5.11 (a) can be noticed from the experimental data in Fig. 5.12. The work function signal detected at the 65nm wide NPD at *step 1* decreases slower with increasing tip sample distance than that of the 20nm wide NPD at *step 2*. Consequently, an influence of NPD width on the averaging effect of the work function signal could also be confirmed experimentally.

Within this section the influence of NPD width on the averaging effect of nanoscale potential distributions in Kelvin probe force microscopy experiments was investigated. A clear effect of the NPD width on the averaging effect was revealed by means of KPFS simulations. It could be shown that with decreasing NPD width the fraction of the work function signal detected at a nanoscale potential distribution decreases as well. This

[10] To enable comparison with the simulation data, the experimental data were converted to the effective tip-sample distance z_{eff}.

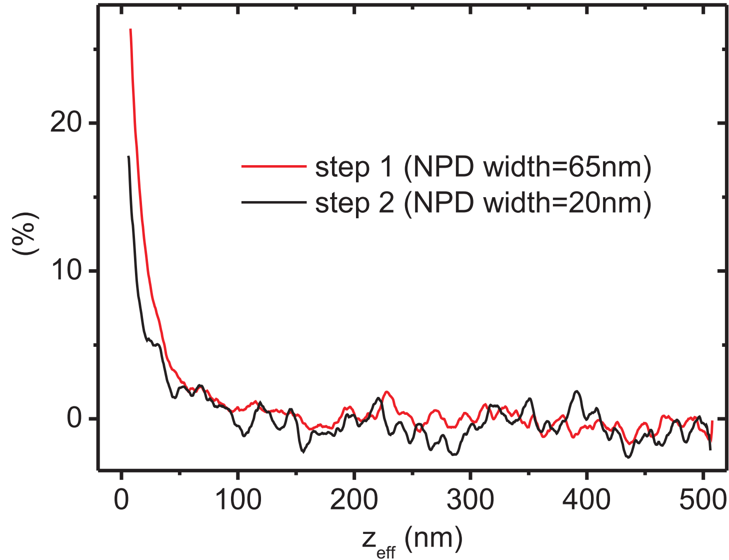

Figure 5.12: *Experimental KPFS difference spectra of the NPD work function signal ($\Delta\Phi$) taken at step 1 and step 2 (see Tab. 5.1). Both spectra were normalized at their minimal effective tip-sample distances (see Tab. 5.1), according to the absolute work function signal percentage obtained from the simulation data shown in Fig. 5.11 (a).*

finding was also confirmed experimentally.
In summary, the results of this section clearly demonstrate that one needs to consider the influence of NPD width on the averaging effect, if Kelvin probe force microscopy results obtained at nanoscale potential distributions are discussed quantitatively.

5.3.3 The influence of tip-sample distance

The influence of tip-sample distance on the averaging effect of work function signals of nanoscale potential distributions (NPDs) in Kelvin probe force microscopy (KPFM) was experimentally studied at *step 1* (see Fig. 5.3 and Tab. 5.1). In Fig. 5.13 the Kelvin probe force spectroscopy (KPFS) difference spectrum[11] obtained at *step 1* is shown as red, solid line. It was, like all experimental difference spectra displayed within this thesis, additionally smoothed by a 20-point adjacent average for further signal improvement [153].
For the smallest effective tip-sample distance of 7.7nm (see Tab. 5.1) the difference spectrum yields a NPD work function signal ($\Delta\Phi$) of -90meV, which is in good agreement with Kelvin probe force microscopy (KPFM) measurements at *step 1* depicted in Fig. 5.3 and Fig. 5.6 (a). With increasing tip-sample distance a strong decrease of the work function signal is observed.

In order to quantify the distance dependence of the work function signal, the experimental data of Fig. 5.13 was reproduced by means of KPFS simulations (see Sec. 5.1.2). The advantage of the KPFS simulations is that the absolute potential variation of the NPD is an input parameter. Consequently, it is possible to extrapolate the absolute work function

[11] The two spectra (NPD/background) from which the difference spectrum was deducted are shown in Fig. 5.6 (b).

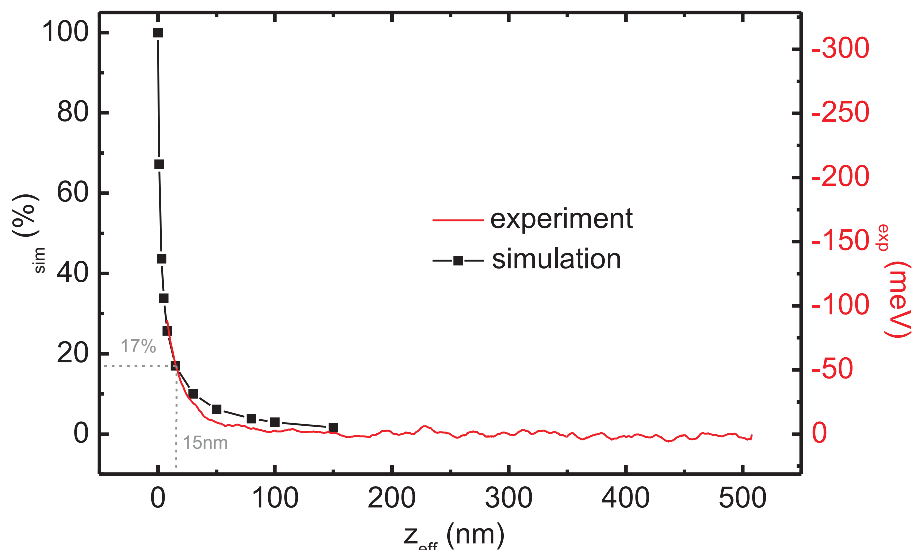

Figure 5.13: *KPFS difference spectra of the NPD work function signal ($\Delta\Phi$) obtained at step 1 (see Tab. 5.1). The red line displays the experimental data. The simulation data, which was fitted to the experiment, is displayed as black line (squares). For simulation parameters see Tab. A.1.*

variation (i.e. at $z_{eff} = 0$) of the experiment by fitting the simulation to the experimental data.
For this purpose simulation parameters as close as possible to the experimental setup were chosen. The simulation's input data for the tip geometry was determined based on scanning electron micrographs of the tip used in the experiment (shown in Fig. 5.9 (a)). However, an optimization of the obtained geometry data was necessary, as the simulation assumes a cone-shaped, symmetric tip (see Fig. 4.7 (a)), while the tip used in the experiment was pyramidal and non-symmetric. The NPD width of the potential dip was determined from the KPFM measurement at *step 1* displayed in Fig. 5.3. It is reasonable to use this information, since it was previously shown that the NPD width is hardly affected by the averaging effect [142]. The topography step of about 4nm was neglected in the simulations, as prior simulations did not show any impact of small step-like topographies on KPFM measurements [152].
In order to fit the simulation to the experimental data, a scaling factor s between the simulation's y-axis ($\Delta\Phi_{sim}(\%)$) and the experimental y-axis ($\Delta\Phi_{exp}(\text{meV})$) was used (see Fig. 5.13), which is defined via: $\Delta\Phi_{exp}(\text{meV}) = s \cdot \Delta\Phi_{sim}(\%)$. A least-squares fit was applied to determine the optimum value of s.

The black line (squares) in Fig. 5.13 shows the simulated difference spectrum[12] fitted to the experiment with the help of the procedure described above. Based on the excellent agreement between the simulation and the experimental data, the absolute value of the experimental work function variation at *step 1* can be determined as 320meV±70meV. The inaccuracy of the result was calculated via error propagation considering the inaccuracy of the experimental and simulation data [154].

[12] The two spectra (NPD/background) from which the difference spectrum was deducted are shown in Fig. 5.7.

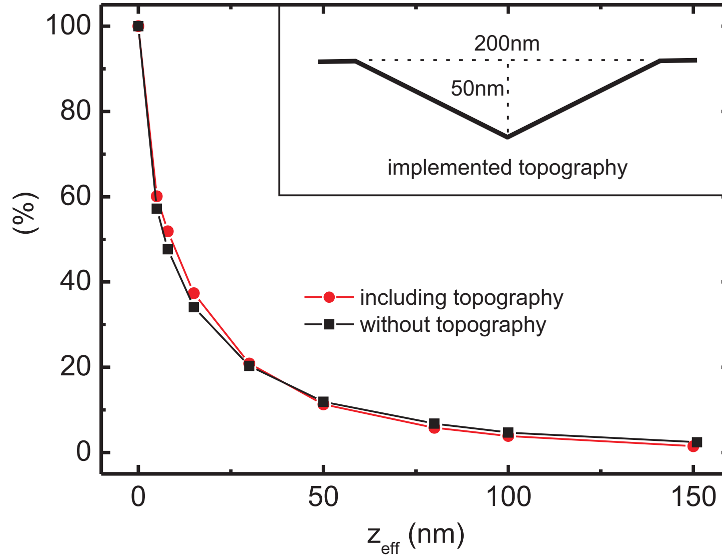

Figure 5.14: *Simulated KPFS difference spectra of the NPD work function signal ($\Delta\Phi$). In the case of the black spectrum (squares) no surface topography was implemented in the simulation. For the red spectrum (dots) a valley-like topography (see inset) was included in the simulations. For simulation parameters see Tab. A.1.*

A strong distance dependence of the work function signal can be noticed from Fig. 5.13. At an effective tip-sample distance of 15nm, which is a typical working-distance for cantilever based KPFM-imaging[13], only about 17% of the full NPD-signal is detectable. Furthermore, the distance dependence curve displays a steep slope in the working regime of KPFM up to $\approx$ 30nm. This illustrates that the magnitude of work function signals of NPDs detected by KPFM is very sensitive with respect to the tip-sample distance.

In summary, the results presented in this section demonstrate that Kelvin probe force microscopy experiments at nanoscale potential distributions are strongly distance-dependent. It is mandatory to consider this distance dependence of the work function signal, if Kelvin probe force microscopy results obtained at nanoscale potential distributions are discussed quantitatively.

5.3.4 The influence of surface topography

While surface steps on GaAs(110) only show a negligible surface topography [152], grain boundaries (GBs) in Cu(In,Ga)Se_2 thin films typically display a significant, valley-like topography (see Fig. 5.3). One could imagine an influence of this topography on the averaging effect of nanoscale potential distributions (NPDs) in Kelvin probe force microscopy (KPFM), as a strong interaction between the tip and the sides of the valleys might reduce or enhance the averaging effect, for example.
To investigate the possible influence of surface topography, Kelvin probe fore spectroscopy (KPFS) simulations were employed (see Sec. 5.1.2). In Fig. 5.14 two simulated KPFS difference spectra are shown. In case of the black spectrum (squares) no surface topography

[13]The KPFM experiments on CIGSe thin films shown in Chap. 6 and 7 were performed at z_{eff} = 15nm.

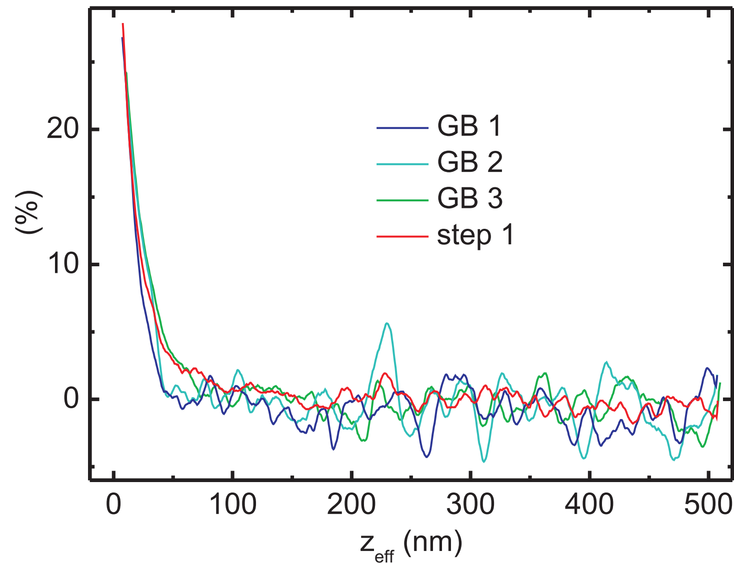

Figure 5.15: *Experimental KPFS difference spectra of the NPD work function signal ($\Delta\Phi$) taken at GB 1-GB 3, and step 1 (see Tab. 5.1). All spectra were normalized at the smallest common tip-sample distance z_{eff}=9.7nm, according to the absolute NPD work function signal percentage from Fig. 5.13.*

was implemented in the simulations, while for the red spectrum (dots) a valley-like surface topography of 200nm width and 50nm depth was included (see inset of Fig. 5.14). Nevertheless, the course of both difference spectra is nearly identical. No significant difference between the two spectra is visible for any tip-sample distance. Consequently, the results of the simulation do not suggest any significant influence of a valley-like surface topography on the averaging effect of NPD work function signals ($\Delta\Phi$) in KPFM measurements.

The influence of surface topography on the averaging effect was also investigated experimentally. For this purpose the averaging effect of the NPD work function signal at *GB 1*, *GB 2*, and *GB 3* was studied by means of KPFS. All grain boundaries exhibit valley-like surface topographies (see Fig. 5.3). In Fig. 5.15 the difference spectra[14] taken at the NPDs of the various GBs are displayed. In addition, the difference spectrum taken at the NPD of *step 1* is also shown, as a reference spectrum with negligible surface topography. All spectra were normalized at the smallest common tip-sample distance z_{eff}=9.7nm, according to the absolute NPD work function signal percentage obtained from Fig. 5.13, to enable direct comparison. A 20-point adjacent average was applied to each of the difference spectra for further signal improvement [153].
No influence of surface topography on the averaging effect can be seen in Fig. 5.15. All spectra show a similar distance dependence, independent of the topography. Especially for smaller tip-sample distances of up to $\approx$ 30nm, which are the relevant distances for KPFM experiments, the spectra are almost identical.
The rather large scattering of the spectra *GB 1-GB 3* (noise level $\approx$ 5% of $\Delta\Phi$), compared with the spectrum of *step 1*, is mainly caused by a reduced signal-to-noise ratio. While the NPD at *step 1* exhibits an absolute work function dip of about -320meV, based on the results from Fig. 5.13, the NPDs at *GB 1-GB 3* only exhibit a work function signal

[14]The difference spectra were deducted from the spectra (NPD/background) displayed in Fig. 5.8.

between ≈ -200meV and -270meV.

Within this section the influence of surface topography on the work function signal of nanoscale potential distributions detected in Kelvin probe force microscopy was investigated. No significant influence of valley-like surface topographies was observed by means of both Kelvin probe force spectroscopy simulations and experiments.

5.4 Conclusions

The averaging effect of work function signals of nanoscale potential distributions (NPDs) in Kelvin probe force microscopy was studied by means of Kelvin probe force spectroscopy in experiment and simulation. The combination of both methods made it possible to quantify the magnitude of the averaging effect in dependence of the geometry parameters of the experimental setup.

The results reveal that the averaging effect significantly decreases the detected work function signal at nanoscale potential distributions. The magnitude of the decrease depends on the geometry of the used tip, the width of the investigated NPD, and the experimental tip-sample distance.
In particular, a strong distance dependence of the averaging effect was discovered. At an effective tip-sample distance of 15nm, which is a typical distance used in cantilever-based KPFM, only about 17% of the full work function signal of a NPD could be detected in our experiments. This strong distance dependence basically prohibits any direct, quantitative comparison of KPFM experimental results obtained at different tip-sample distances, or a direct comparison with theoretical calculations.

A significant influence of surface topography on the averaging effect could be excluded. Both our experimental and simulation results did not indicate any influence of valley-like surface topographies on the averaging effect. This finding is of particular interest with respect to the KPFM study on the electronic properties of grain boundaries in polycrystalline $Cu(In,Ga)Se_2$ thin films presented in Chap. 6. GBs in this material system frequently exhibit valley-like topography features.

In summary, the results shown in this chapter clearly demonstrate that it is mandatory to consider the averaging effect, if Kelvin probe force microscopy measurements at nanoscale potential distributions are discussed quantitatively. The results reported within this chapter provide a means to estimate the magnitude of the averaging effect, if the experimental parameters of the KPFM setup are known.

Chapter 6

Electronic grain boundary properties in $Cu(In,Ga)Se_2$ thin films with various Ga-contents

By varying the Ga-content[1] x of polycrystalline $CuIn_{1-x}Ga_xSe_2$ (CIGSe) thin films one can tune the electronic band gap between 1.04eV ($x = 0$) and 1.68eV ($x = 1$) [15] (see Sec. 2.1.2). Theoretically, thin film solar cells based on CIGSe absorbers ("CIGSe solar cells") with a Ga-content of about 0.65 should reach highest energy conversion efficiencies, as their electronic band gap[2] of 1.42eV is optimally matched to the solar spectrum[3] [155]. Experimentally, however, solar cell devices with a Ga-content of about 0.30, which corresponds to an electronic band gap of 1.20eV, deliver the best performance [1, 156]. For higher Ga-contents a drop in solar cell efficiency in discrepancy with theoretical expectations is observed [84, 156].
As the record efficiencies of polycrystalline CIGSe solar cells are at least partly attributed to benign electronic properties of grain boundaries (GBs) in CIGSe [9, 11, 14, 91], one supposition is that the decrease in solar cell efficiency for Ga-contents above ≈ 0.30 is caused by a change of electronic GB properties.

Jiang et al. [84] indeed reported on a close connection between the electronic properties of GBs in CIGSe and the performance of corresponding solar cells. They investigated the potential barriers at CIGSe GBs in dependence of the Ga-content by Kelvin probe force microscopy (KPFM), as shown in Fig. 6.1 (a-I). Up to a Ga-content of 0.28 they observed potential barriers of ≈ -150mV at GBs. The potential barriers sharply dropped to 0mV between 0.28 and 0.38 Ga-content. For Ga-contents higher than 0.38 they did not detect any potential barriers anymore. Since the change of the electronic properties of GBs agrees well with the decrease of device performance, as can be seen by comparison of Fig. 6.1 (a-I) and (a-II), they concluded on a significant role of the electronic properties of GBs for CIGSe solar cell efficiency.
In another study Romero et al. [105] investigated the lateral electron transport across GBs in CIGSe in dependence of the Ga-content by "electro-assisted scanning tunneling

[1]The Gallium-content x is identical to the Ga/(In+Ga)-ratio (see Sec. 2.1).
[2]Calculated band gap (see Eq. (2.1)) [27]. A bowing coefficient of $b = 0.13$ was used [29].
[3]Under air mass 1.5.

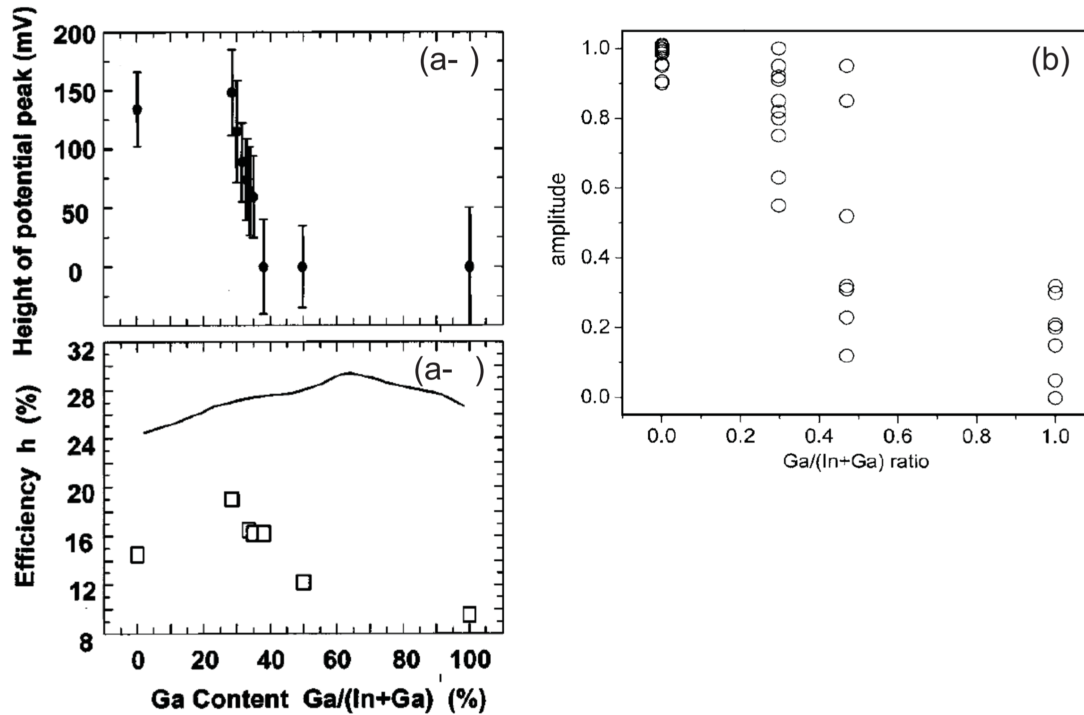

Figure 6.1: *(a-I) Experimental potential barriers at GBs in CIGSe in dependence of the Ga-content. A potential peak of ,e.g., 150mV translates to a 150meV decrease of the work function at the GB compared to the grain surface. Reprint from [84]. (a-II) Theoretical (line) and experimental (open squares) conversion efficiencies of CIGSe solar cells in dependence of the Ga-content under air mass 1.5. Reprint from [84]. (b) Influence of the Ga-content on the electronic potential barriers at GBs in CIGSe. The amplitude corresponds to the fraction of electrons diffusing across a single GB. An amplitude of zero represents a perfect barrier for electron transport across the GB, while an amplitude of unity translates to a nonexistent barrier. Reprint from [105].*

microscopy". Electrons were injected into a specific grain by the electron beam of a scanning electron microscope. The tip of a scanning tunneling microscope was placed above an adjacent grain, and the effect of the injected excess electrons on the tunneling current was monitored. As can be seen in Fig. 6.1 (b), increasing electronic potential barriers at GBs were detected with increasing Ga-content.
The two contradicting studies mentioned above illustrate that the effect of Ga addition on the electronic properties of GBs in CIGSe thin films is controversially discussed in the scientific community. Several more studies can be found in literature that investigate the change of physical properties with increasing Ga-content in CIGSe thin films in general [17, 28, 40, 156, 157] or at GBs in particular [78].

In this chapter we reconsider the problem. We present an elaborate KPFM study on the influence of the Ga-content on the electronic potential barriers at grain boundaries of polycrystalline CIGSe thin films. Untreated as well as wet-chemically cleaned thin films were investigated in an ultra high vacuum environment. We apply a new method of GB localization to assure an unbiased evaluation of electronic GB properties; this was not guaranteed in many prior KPFM studies.

6.1 $Cu(In,Ga)Se_2$ thin films with various Ga-contents

Five $CuIn_{1-x}Ga_xSe_2$ (CIGSe) thin films with Ga-contents varying from $x = 0$ to $x = 1$ were studied by means of Kelvin probe force microscopy (KPFM). They were all grown on molybdenum coated soda lime glass substrates by means of a three stage co-evaporation process [53] (see Sec. 2.2.2) inside the identical growth chamber. For all thin films growth processes as similar as possible were employed. Thereby variations of structural and electronic properties which are not related to a change in the Ga-content are minimized, and the highest possible comparability among the samples is achieved.
Reference solar cells were manufactured for all thin films by chemical bath deposition of a CdS buffer layer and subsequent sputter deposition of an i-ZnO/ZnO:Al double window layer. A Ni/Al grid was employed as front contact. No anti-reflex coating was utilized. An overview of various thin film/device parameters of the different samples/reference solar cells is provided in Tab. 6.1. The data were obtained by means of X-ray fluorescence spectroscopy (composition, thickness) and I-V curve analysis (V_{OC}, J_{SC}, fill factor, efficiency).

All samples were stored in an inert gas atmosphere after manufacturing. However, an exposure to ambient air during the transport to the inert gas conditions was unavoidable. This likely caused an oxidation of the thin film surfaces. As discussed in Sec. 2.2.3, especially In and Ga form surface oxides within a few minutes [58].
The different CIGSe thin films probably exhibit varying levels of surface oxidation, as they were exposed to ambient air for varying amounts of time. While some of the samples were introduced into the inert gas atmosphere within several minutes after manufacturing, other thin films have been exposed to ambient air for several hours.

In order to investigate the effects of oxidation on the electronic properties of grain boundaries in CIGSe, two different series of samples were analyzed in the course of this study. *As grown* samples did not receive any surface treatment. They were exposed to ambient air prior to the measurement; their surfaces are most likely partly oxidized. *Chemically treated* samples, on the other hand, were etched in 0.15M aqueous Potassium cyanide (KCN) solution for 2 minutes prior to the introduction into ultra high vacuum (UHV) conditions. The chemical treatment removes the surface oxides (see Sec. 2.2.3), and creates a defined and reproducible surface condition. It provides a high comparability of the chemical and electronic structure among the different thin films [58]. To prevent *chem-*

Table 6.1: *Overview of various thin film/device parameters of the different CIGSe thin films studied within this chapter.*

Sample	$\frac{\mathbf{Ga}}{\mathbf{Ga+In}}$	$\frac{\mathbf{Cu}}{\mathbf{Ga+In}}$	**Thickness (μm)**	**V_{OC} (mV)**	**J_{SC} (mA/cm^2)**	**Fill factor (%)**	**Efficiency (%)**
CIGSe-0	0.00	0.82	2.05	490.1±3.6	36.9±0.7	72.5±1.9	13.1±0.4
CIGSe-33	0.33	0.86	1.72	633.1±4.2	34.3±0.5	69.9±0.5	15.2±0.3
CIGSe-45	0.45	0.82	2.11	673±158	28.5±0.8	74±20	14.1±4.9
CIGSe-76	0.76	0.80	2.00	718±134	13.1±0.6	51±6	4.8±1.0
CIGSe-100	1.00	0.88	1.89	727±18	13.4±0.6	55±3	5.3±0.4

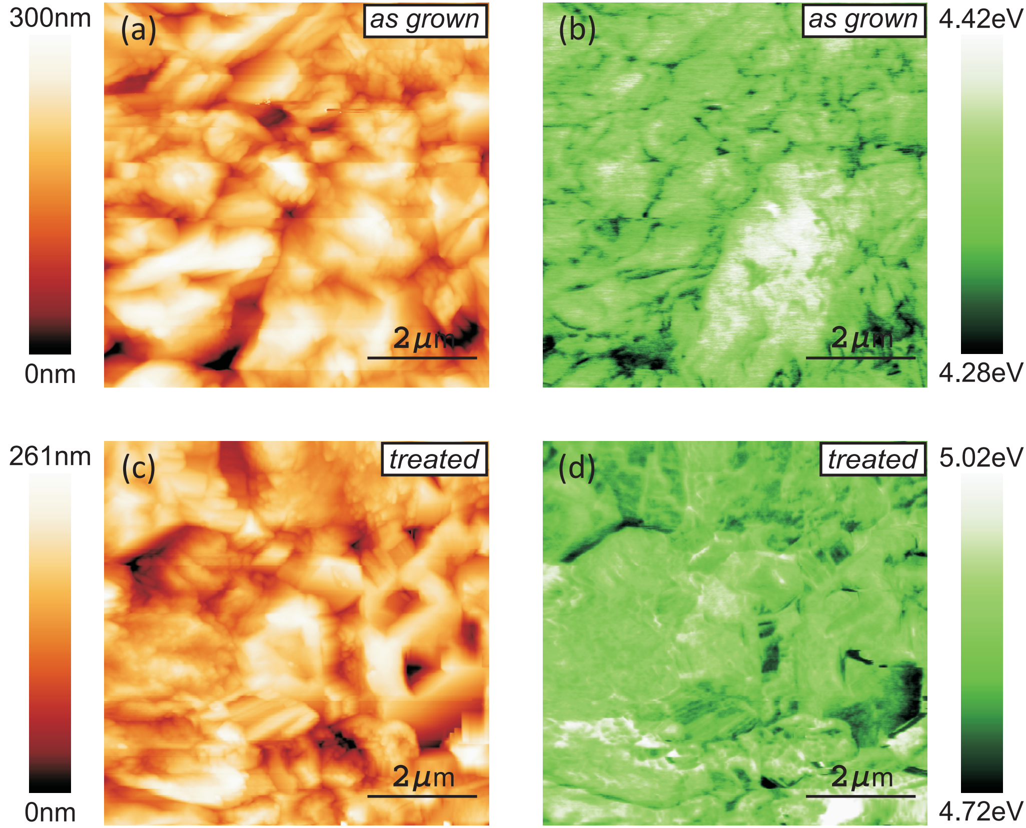

Figure 6.2: *7μm × 7μm KPFM images of the CIGSe-0 thin film (see Tab. 6.1). (a) Topography and (b) work function images of the as grown thin film. (c) Topography and (d) work function images of the chemically treated thin film.*

ically treated samples from re-oxidation, they were kept in an environment of deionized water during the transport to UHV conditions. Directly after the introduction into the UHV environment all samples (*as grown* as well as *chemically treated*) were annealed to temperatures of ≈ 130°C for about 30 minutes to remove residual water.

In Fig. 6.2 KPFM topography and work function images of both an *as grown* and a *chemically treated* CIGSe thin film are shown. No significant difference in surface topography is visible before and after the chemical treatment. This finding is in good agreement with results of prior studies [61, 158, 159], which did not detect a significant influence of short KCN treatments on the surface topography of CIGSe thin films. The work function of the *chemically treated* thin film is increased by about 600meV compared to the *as grown* thin film. This increase is caused by the removal of surface oxides, and is in good agreement with the results shown in Sec. 2.2.3 as well as with results from the literature [103]. The work function image of the *chemically treated* thin film appears to be more detailed than that of the *as grown* thin film. Even work function variations within a single grain are clearly resolved in Fig. 6.2 (d), whereas the work function image in Fig. 6.2 (b) seems less rich of details. Such an increase in lateral resolution of work function images in connection with the chemical treatment was observed several times in the course of this study. It is believed that it is an inherent consequence of the oxide removal.

In Fig. 6.3 KPFM topography and work function images of all five *chemically treated*

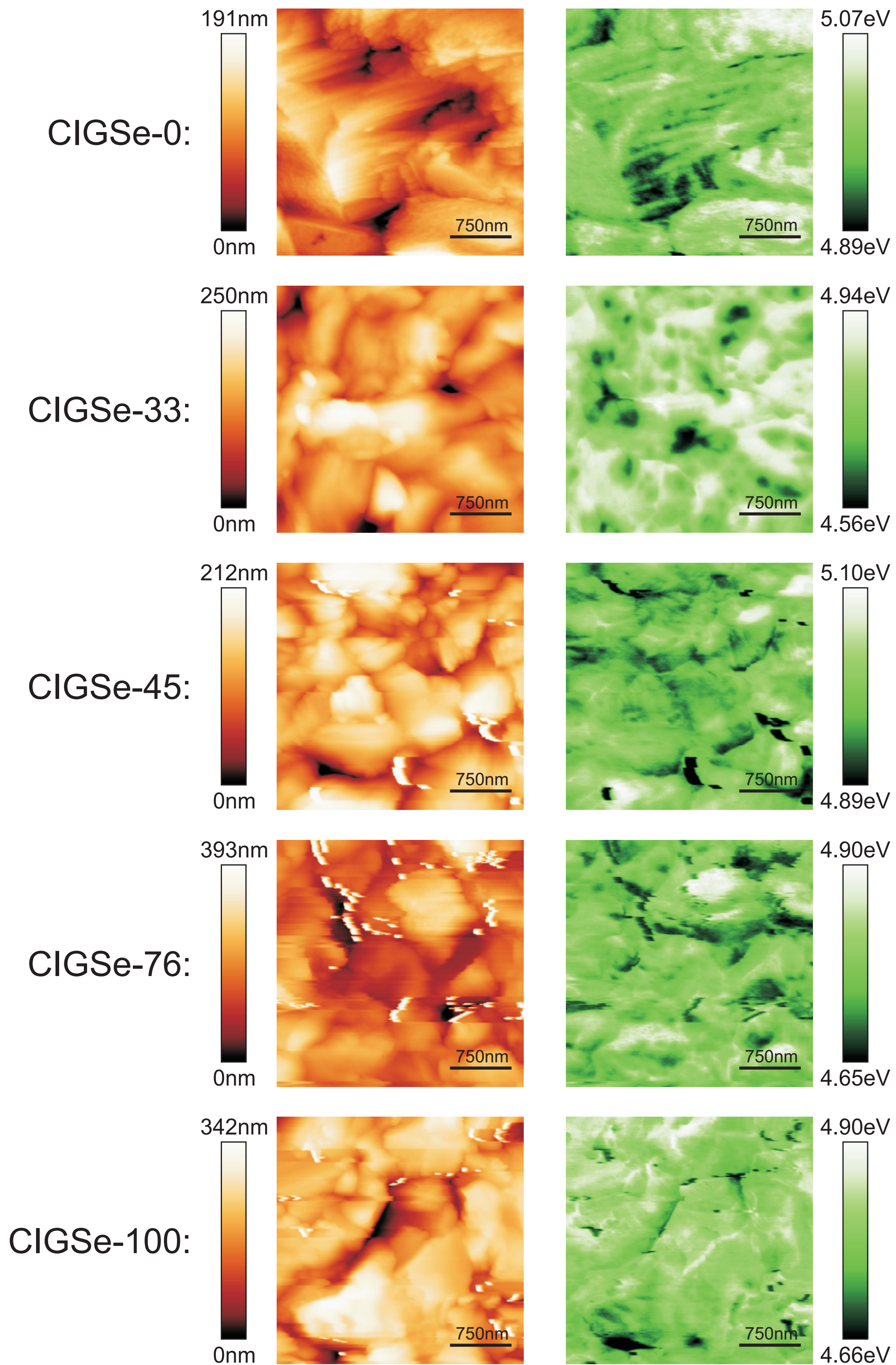

Figure 6.3: *$3\mu m \times 3\mu m$ KPFM topography (left) and work function images (right) of the CIGSe thin films from Tab. 6.1. All films shown here were chemically treated.*

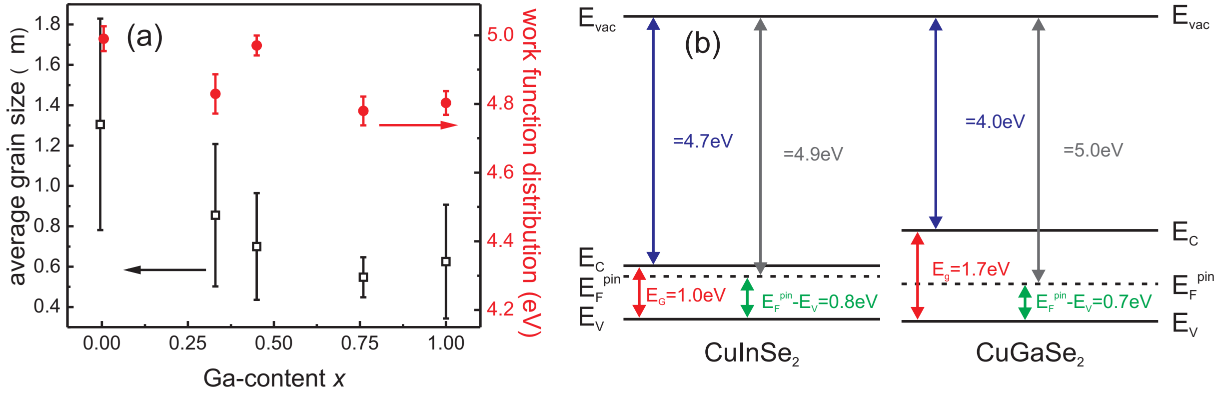

Figure 6.4: *(a) The average grain size of the CIGSe thin films from Tab. 6.1 in dependence of the Ga-content is depicted by open squares. The error bars indicate the arithmetic mean of the grain size statistics (twenty grains from various KPFM images were evaluated for each Ga-content). The work function distribution (see Sec. 4.1.3.2) of the KPFM images displayed in Fig. 6.3 is depicted by solid dots. The error bars indicate the full width half maxima of the work function distributions of the images. (b) Schematics of the band structures of $CuInSe_2$ and $CuGaSe_2$. The literature values were taken from: [15] (Band gap energy E_G), [160, 161] (Electron affinity χ), and [38, 40] ($E_F^{pin} - E_V$). The work function (Φ) values were calculated based on these literature values.*

thin films from Tab. 6.1 are shown. From the topography images one can recognize a difference in grain size between the CIGSe-0 sample and the other samples. In Fig. 6.4 (a) the average grain size[4], extracted from twenty grains from various KPFM images for each Ga-content, is plotted in dependence of the Ga-content. For a Ga-content of 0 an average grain size of about 1.3μm is observed. With increasing Ga-content the average grain size decreases to about 600nm. This dependence of the grain size on the Ga-content is in good agreement with prior results from Abou-Ras et al. [17]. They have shown that the grain size in CIGSe is governed by the lattice strain in its pseudocubic crystal structure. A maximum grain size is obtained for a Ga-content of about 0.23 (due to the limited number of investigated samples this peak is not visible in Fig. 6.4 (a)). For this Ga-content the CIGSe crystal grows in the ideal pseudocubic crystal structure with the ratio of the lattice constants $c/a = 2$. Any change in Ga-content causes a deviation from this c/a-ratio, which induces lattice strain and consequently reduces the grain size.
The increased strain in the crystal structure might also be the reason for the higher surface roughness of CIGSe-76 and CIGSe-100 thin films compared to the CIGSe thin films with lower Ga-content, which was always observed in KPFM measurements. It can be noticed best by comparison of the different z-scales in the topography images of Fig. 6.3.
The work function distributions (see Sec. 4.1.3.2) of the work function images shown in Fig. 6.3 are also plotted in Fig. 6.4 (a). No systematic dependence of the work function on the Ga-content is observed. All work function values are similar, varying between $\approx$ 4.8eV$-$5.0eV. The similar work function values can be understood by assuming a high density of donor defect states at the CIGSe surfaces. In this case the Fermi level E_F is pinned at a similar distance above the valence band maximum E_V for both $CuInSe_2$

[4] The grain shape was approximated as elliptic. The grain size was defined as the arithmetic average of the grain's minor and major semi-axis.

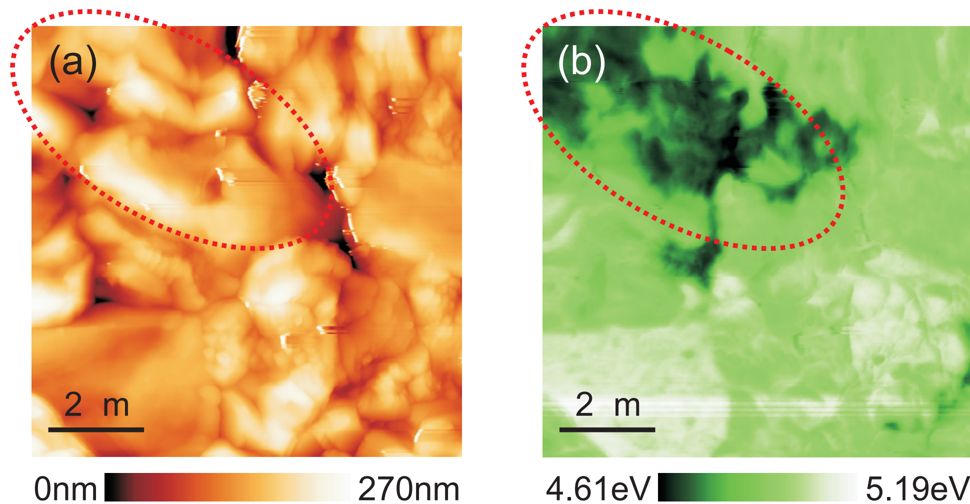

Figure 6.5: *9µm × 9µm KPFM topography and work function image of the chemically treated CIGSe-0 thin film. The area with a decreased work function value is marked by a red ellipse.*

and $CuGaSe_2$ [38, 40]. Since the valence band maxima of $CuInSe_2$ and in $CuGaSe_2$ are located at similar energy levels as well (see Sec. 2.1.2), the work functions of $CuInSe_2$ and $CuGaSe_2$ are expected to be similar. Schematics of the band structures of both $CuInSe_2$ and $CuGaSe_2$, which were composed from data available in the literature, are shown in Fig. 6.4 (b). The schematics indicate that the work function values measured by means of KPFM (see Fig. 6.3) are also in good quantitative agreement with expectations from literature.

One phenomenon that was observed several times in the course of this study is the appearance of surface areas with distinctively increased or decreased work function values. Such areas, as exemplary shown in Fig. 6.5[5], were detected for various Ga-contents and on both *as grown* and *chemically treated* surfaces. The work function variations did not seem to be localized to specific grains, but rather extended over several grains. The magnitude of the variations ranged up to hundreds of meV (≈ 300meV for the example in Fig. 6.5). Variations in the electronic properties of CIGSe thin films which are not correlated to the grain structure were already reported by Bauer et al. [162, 163]. By means of confocal microscopic photoluminescence they detected domains in the range of $3\mu m - 10\mu m$ in CIGSe thin films, which exhibited significant differences in the splitting of the quasi Fermi-levels under illumination. They proposed that the origin of these domains might be a variation in the elemental composition or the metallurgical phase in CIGSe thin films. It seems possible that the work function variations that were observed in the course of this study have a similar origin as the different domains detected by Bauer et al.. Nevertheless, further investigations which are out of the scope of this thesis are required to verify this supposition.
Within this thesis areas with a noticeably altered work function were excluded from any evaluation, to avoid possible misinterpretations of the results.

[5] This image is discussed in more detail in Chapter 7.

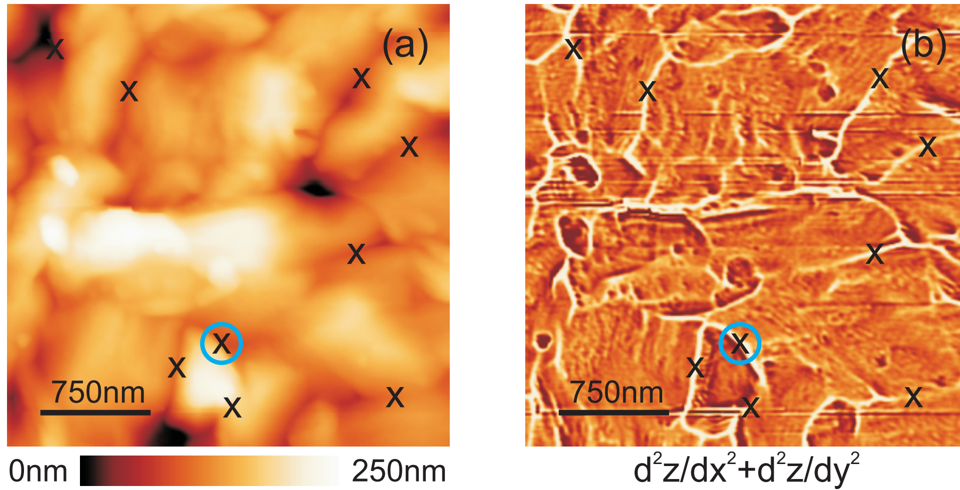

Figure 6.6: *3µm × 3µm KPFM image of the (a) topography and (b) Laplace-transformation of the topography of the chemically treated CIGSe-33 thin film. The positions of GBs, as determined based on these images, are marked by black crosses. The GB, which is analyzed in Fig. 6.7, is highlighted by a blue circle.*

6.2 Topography-based localization of grain boundaries

One major challenge in the analysis of the electronic properties of grain boundaries (GBs) in $Cu(In,Ga)Se_2$ (CIGSe) thin films by Kelvin probe force microscopy (KPFM) is the correct localization of the GBs. Previous studies frequently consulted both the KPFM topography and work function images to determine the position of a GB [10, 100]. This is not the best approach, as GBs with certain electronic properties are preferentially selected. A physically correct way to localize GBs is the combination of KPFM and electron backscatter diffraction (EBSD). In EBSD the positions of GBs are unambiguously determined by an analysis of the atomic lattice orientation. However, combined KPFM and EBSD experiments are very challenging and time-consuming. Consequently, this method is not suited for extensive studies in which multiple samples need to be investigated.

For the analysis presented in this chapter a new approach was chosen; only topography images were consulted for the determination of the GBs' positions. This approach represents a good compromise between the two methods of localization mentioned above. On the one hand it is not affected by the electronic contrast of GBs in KPFM work function images. Therefore, it facilitates the unbiased localization of GBs with various electronic properties. On the other hand it does not require any additional information not accessible by KPFM. This permits a quick evaluation of the experimental data.

The following criteria were applied to determine the position of a GB based on a KPFM topography image:

- The GB needs to exhibit a significant surface topography.
- The shape of the whole grain needs to be perceivable in the topography image.
- If there is any doubt about the origin of a surface feature, it is not considered as GB.

Fig. 6.6 (a) shows a typical KPFM topography image of a CIGSe thin film. In this image the positions of GBs localized with the help of the criteria given above are marked by black crosses. The Laplace-transformation of the topography image is depicted in Fig. 6.6 (b). Laplace-transformation images can assist in the localization of GBs, as transitions between areas with constant slope (i.e. GBs) are emphasized in such images.

One drawback of a topography-based localization of GBs is that highly symmetric $\Sigma3$ GBs have a lower probability to be detected than lower symmetric non-$\Sigma3$ GBs. More details about this issue, and a comparison of a topography-based GB localization to a physically correct localization of GBs by means of combined KPFM and EBSD measurements are provided in Sec. 7.2.

6.3 Analysis of electronic grain boundary properties

The electronic properties of grain boundaries (GBs) were extracted from Kelvin probe force microscopy (KPFM) work function images by taking line profiles perpendicular to the GBs. Ten neighboring line profiles were averaged for the analysis of a single GB, in order to reduce the noise level. In Fig. 6.7 the analysis of a typical GB is shown. In the KPFM topography image in Fig. 6.7 (a) the shape of "grain 1" is clearly perceivable. The GB between this grain and the adjacent "grain 2" is analyzed. The topography line profile in Fig. 6.7 (b) yields a step-like transition of about 100nm between the two grains. Such step-like transitions are together with valley-like transitions the most frequent surface feature observed at GBs in CIGSe. In Fig. 6.7 (c) the KPFM work function image corresponding to Fig. 6.7 (a) is shown. One can notice the bright contrast along the GB between grain 1 and grain 2. It represents an increase in work function along the GB with respect to the grain surfaces. With the help of the work function line profile in Fig. 6.7 (d) this increase can be analyzed quantitatively. Since grain 1 and grain 2 exhibit different work function values, due to different surface facets at both grains (see Sec. 2.1.3), the work function variation at the GB is defined as the average of the work function change from the center of the GB ("GB") with respect to the minimum work function values at grain 1 and grain 2, respectively (see Fig. 6.7 (d)).
With this definition one obtains an increase in work function of (82meV+60meV)/2=71meV at the GB between grain 1 and grain 2.

In the course of this thesis the electronic properties of GBs are discussed in terms of electronic potential barriers. The following sign convention is used:

- **Positive potential barrier:** A positive potential barrier represents an increase in work function at the GB with respect to the grain surface (see Fig. 6.8 (a)). Negative charge is localized at the GB, which is compensated by the accumulation of free holes (see Sec. 3.2.1.3).

- **Negative potential barrier:** A negative potential barrier represents a decrease in work function at the GB with respect to the grain surface (see Fig. 6.8 (b)). Positive charge is localized at the GB, which is compensated by the formation of a space charge region (see Sec. 3.2.1.3).

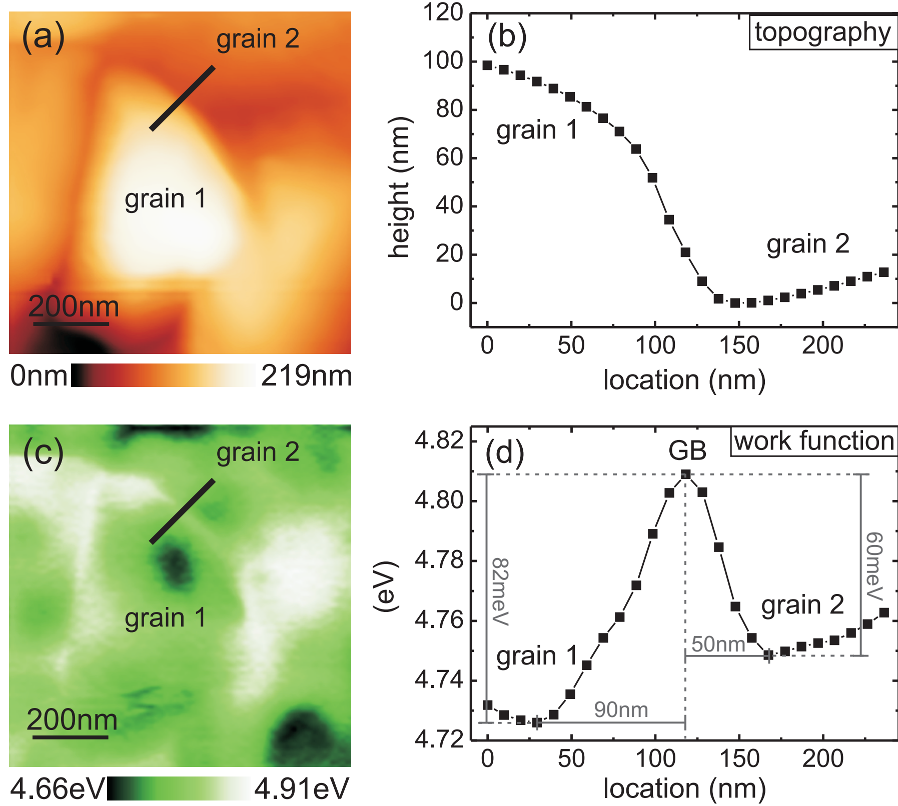

Figure 6.7: *900nm × 900nm KPFM images of the (a) topography and (b) work function (Φ) of the chemically treated CIGSe-33 thin film. Averaged line profiles (10 neighboring lines were averaged) of (c) topography and (d) work function across a GB, as indicated in (a), (b) by the black lines. The analyzed GB can also be seen in Fig. 6.6.*

- **No potential barrier:** No work function variation at the GB with respect to the grain surface is observed (see Fig. 6.8 (c)). Since localized charges are the reason for potential variations at GBs [79, 100], such GBs are frequently referred to as charge neutral [91].

According to this convention the GB analyzed in Fig. 6.7 (d) exhibits a positive potential barrier ΔV_{GB} of +71mV.

The width of the potential barrier at the GB between grain 1 and grain 2 is also obtained from the work function line profile in Fig. 6.7 (d). It is defined as the average of the lateral distances between the center of the GB and the positions of the minimum work function values at grain 1 and grain 2, respectively (see Fig. 6.7 (d))[6]. With this definition, one obtains a width of (90nm+50nm)/2=70nm for the work function variation between grain 1 and grain 2.
In accordance with the terminology of Chap. 5 the width of work function variations at GBs is referred to as nanoscale potential distribution (NPD) width w in the following.

An estimation of the measurement inaccuracies in the determination of potential barriers and NPD widths at GBs is provided in Sec. A.5.

[6]The different potential barrier width/potential barrier ratio at both sides of the GB is caused by variations in the doping density of the CIGSe material, as discussed in detail in Sec. 6.4.3.

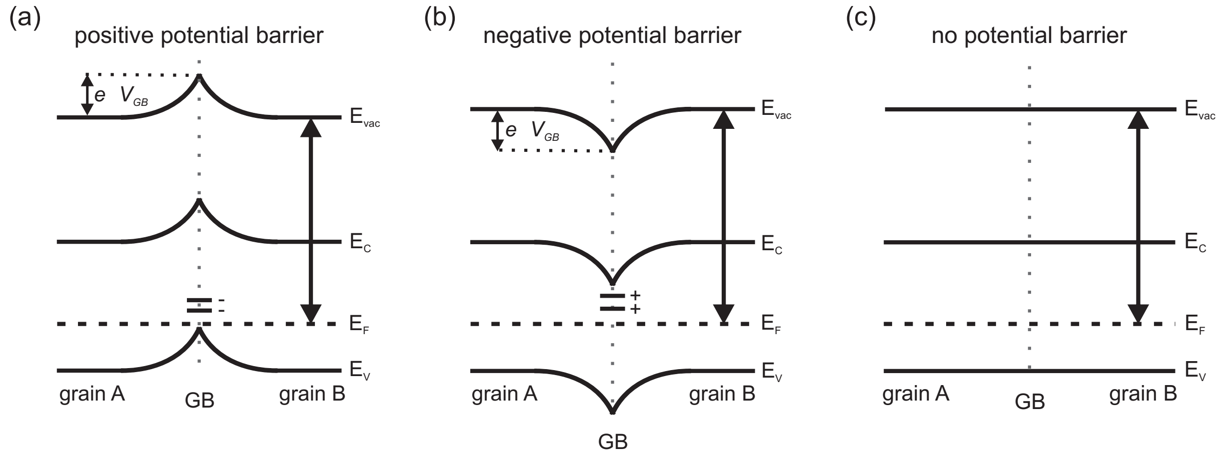

Figure 6.8: *Schematics of the electronic band structure at a GB in case of (a) a positive potential barrier, (b) negative potential barrier, and (c) no potential barrier.*

6.4 Electronic potential barriers at grain boundaries

In order to investigate the electronic properties of grain boundaries (GBs) in polycrystalline $CuIn_{1-x}Ga_xSe_2$ (CIGSe) thin films in dependence of the Ga-content x, twenty GBs were analyzed for each of the five thin films from Tab. 6.1 by means of Kelvin probe force microscopy. GBs from three macroscopically different surface positions[7] were evaluated for each Ga-content to reduce the influence of possible lateral inhomogeneities in the surfaces' electronic structure.

6.4.1 The influence of surface condition

In Fig. 6.9 the electronic potential barriers at grain boundaries (GBs), as obtained from the analysis of Kelvin probe force microscopy (KPFM) images (see Sec. 6.3), are plotted as a function of the Ga-content for both *as grown* and *chemically treated* $Cu(In,Ga)Se_2$ (CIGSe) thin films (see Sec. 2.2.3). No significant difference in the electronic GB properties between *as grown* and *chemically treated* thin films can be noticed. A similar variation of the potential barriers at GBs, in the range from ≈ -100mV to +100mV, is observed with and without the KCN etching. Only in the case of the *as grown* CIGSe-0 thin film a difference in the electronic GB properties can be noticed; in contrast to all other investigated thin films no positive potential barriers were observed. However, since both positive and negative potential barriers were detected for CIGSe-0 after the chemical treatment, this difference is attributed to a surface contamination and not further considered within the discussion. Further investigations (out of the scope of this thesis) with other methods (e.g. X-ray photoelectron spectroscopy) would be required to gain insights about this finding. Based on the results from Fig. 6.9 it is concluded that a moderate surface oxidation[8] does not alter the electronic properties of GBs in CIGSe thin films.

A slight increase in the number of GBs without potential barrier can be noticed in Fig. 6.9

[7] The particular positions were located several mm away from each other.
[8] Exposure time of the thin films to ambient air $<\approx$ 24h.

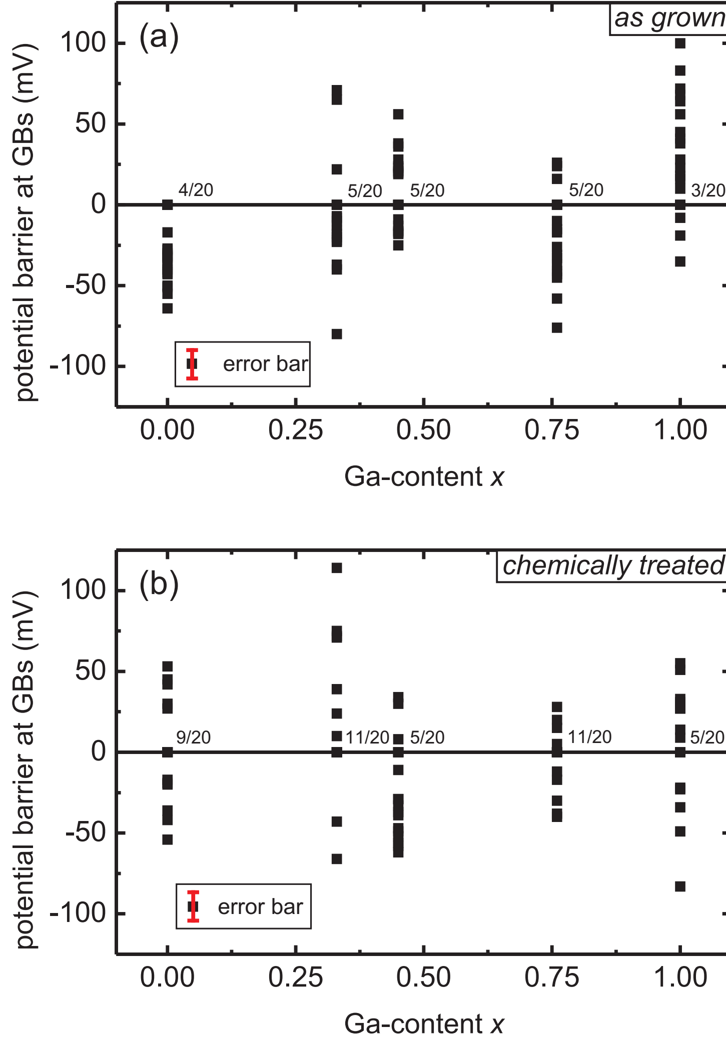

Figure 6.9: *Electronic potential barriers at GBs in dependence of the Ga-content for (a) as grown CIGSe thin films, and (b) chemically treated CIGSe thin films. A positive potential barrier represents an increase in work function at the GB with respect to the grain surface, while a negative potential barrier indicates a decreased work function at the GB with respect to the grain surface (see Sec. 6.3). 20 GBs were evaluated for each Ga-content and surface condition. The number of GBs with no potential barrier is indicated for each Ga-content by the black numbers. For information about the determination of the measurement inaccuracy, which is indicated by the error bars, see Sec. A.5.*

after the chemical treatment. This increase is attributed to the removal of electronically active defect states in connection with the chemical treatment. Donor or acceptor-like defect stats which are localized at a GBs induce a band bending towards the GB [79, 100], as depicted in Fig. 6.8 (a) and (b). The chemical treatment, in combination with the subsequent sample transport in deionized water, removes such defect states from the GBs [83]. Consequently, the electronic activity of the GBs is reduced.
A possible candidate that can induce such defect states is Na. Na is provided by the soda lime glass substrate, and diffuses through the CIGSe absorber to the surface of a CIGSe thin films [164]. There it mainly segregates at the GBs [11, 165]. It alters the work function, as it reduces the surface dipole [164], acts as a shallow acceptor (Na_{In}) [34], or

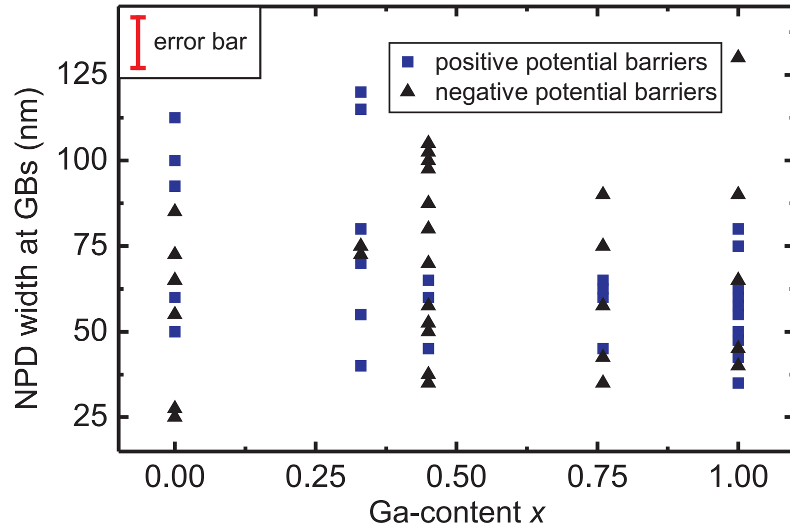

Figure 6.10: *NPD widths of the electronically active GBs from Fig. 6.9 (b) in dependence of the Ga-content. The NPD width is defined as described in Sec. 6.3. For information about the determination of the measurement inaccuracy, which is displayed by the error bar, see Sec. A.5.*

a shallow donor-like defect (Na_i) [11].

6.4.2 Absolute dimensions of the potential barriers

One critical issue about the potential barriers shown in Fig. 6.9 is the dimensions of the detected barriers. Potential barriers at grain boundaries (GBs) represent a variation in the work function which is confined to the nm-range. Consequently, Kelvin probe force microscopy (KPFM) measurements of such potential barriers are subject to the averaging effect through the tip of the cantilever, which is discussed in detail in Chap. 5.

The magnitude of the averaging effect depends on various geometry parameters of the experimental setup, namely the geometry of the used tip, the tip-sample distance, and the NPD width[9].
All cantilevers used in the course of this study exhibited a similar tip-geometry[10]. The tip-sample distance was also kept constant at $z_{eff} \approx 15$nm for all experiments. Consequently, the only geometry parameter affecting the magnitude of the averaging effect which varied in the course of this study is the width of the potential barriers.

In Fig. 6.10 the NPD widths of the electronically active GBs from Fig. 6.9 (b) are plotted as a function of the Ga-content. A variation in NPD width between $\approx$ 25nm and 125nm can be noticed, while no dependence of the NPD width on the Ga-content is observed. The variation in NPD width can be understood, if one considers the different potential barriers observed in Fig. 6.9 (b). According to Eq. (3.3) and Eq. (3.4), different potential barriers result in different NPD widths.

[9]The GB topography has a negligible influence on the experimental results, as demonstrated in Sec. 5.3.4.
[10]Si cantilevers with Pt-Ir coated tip from the same manufacturer (EFM-PPP, *www.nanoworld.com*) were used for all experiments.

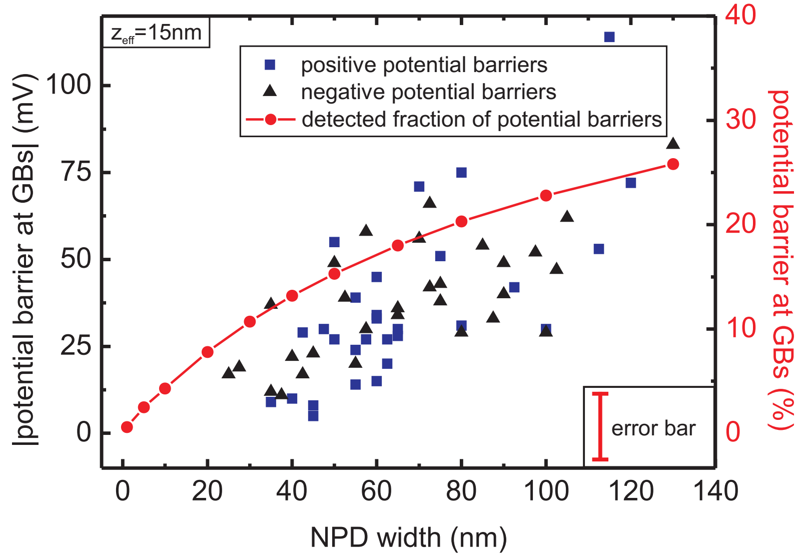

Figure 6.11: *Left y-axis: Absolute values of the potential barriers of the electronically active GBs from Fig. 6.9 (b) (black triangles, blue squares) in dependence of the NPD width. For information about the determination of the measurement inaccuracy, which is displayed by the error bar, see Sec. A.5. Right y-axis: Simulation results (red dots) representing the fraction of the potential barriers, which is detected in the KPFM experiments in dependence of the NPD width (see Sec. 5.3.2). For simulation parameters see Tab. A.1.*

The minimum NPD width of $\approx$ 25nm observed in the experiments can be explained considering the radius of the used tip ($r \approx$ 20nm, see Fig. 5.9). It has been shown in an earlier publication [142] that the radius of the tip represents a lower limit for the lateral electronic resolution of potential variations in KPFM. Smaller potential variations can still be detected by KPFM. However, their widths appear widened in KPFM images, due to the averaging effect through the tip.
An additional reason why smaller NPD widths were not observed experimentally is that they correspond to very small potential barriers, which are in the range of the noise level of the experimental setup.

In Fig. 6.11 the absolute values of the potential barriers of the electronically active GBs from Fig. 6.9 (b) are plotted against their NPD widths. Additionally, the simulation data from Fig. 5.11 (b) is depicted as well. The simulation data displays the fraction of a potential barrier which is detected in KPFM experiments in dependence of the barrier's NPD width[11]. By comparison of the experimental data with the simulation data one can find out which fraction of the full potential barrier was detected experimentally at any arbitrary GB in Fig. 6.11.
In order to incorporate the averaging effect in the analysis of the potential barriers, the simulation data from Fig. 6.11 was fitted with an analytic function (see Sec. A.4). Based on the fit function, the magnitude of the averaging effect was calculated individually for each potential barrier in Fig. 6.11. In Fig. 6.12 the potential barriers at the GBs are depicted in dependence of the Ga-content, similar to Fig. 6.9 (b). This time, however,

[11]For the simulation input parameters in accordance to the geometry of the experimental setup were used.

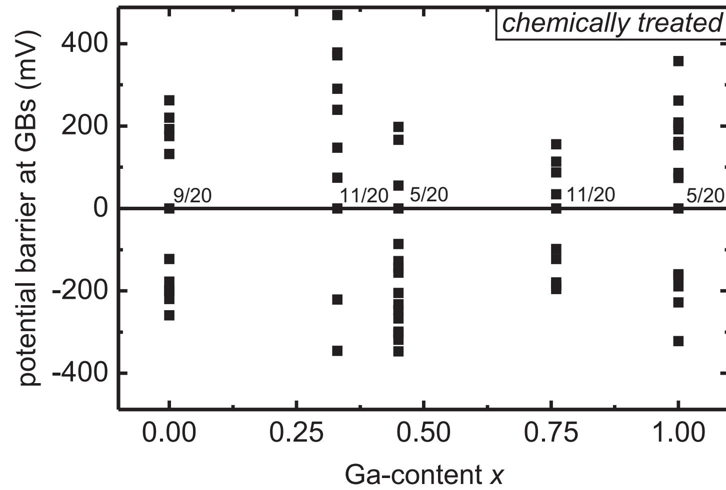

Figure 6.12: *Electronic properties of GBs in dependence of the Ga-content for chemically treated CIGSe thin films. 20 GBs were evaluated for each Ga-content. The number of GBs with no potential barrier is indicated for each Ga-content by the black numbers. The averaging effect through the tip of the KPFM cantilever was considered in the analysis.*

the averaging effect through the tip of the cantilever was considered in the analysis. No change in qualitative information can be noticed when comparing Fig. 6.9 (b) to Fig. 6.12. The main difference between both figures is the magnitude of the potential barriers. It is increased by a factor of ≈ 5, due to the incorporation of the averaging effect.

6.4.3 Doping densities and defect densities

Negative potential barriers

In the case of a negative potential barrier positive charge is localized at the grain boundary (GB) which repels free holes[12] from the near GB region. Ionized acceptor atoms are left in the vicinity of the GB. They form a space charge region (SCR) which compensates the positive charge of the GB (see Fig. 6.8 (b)).

Based on the potential distribution across the SCR (see Eq. (3.3)), one can derive a relation between the potential barrier ΔV_{GB} and the NPD width w of a GB:

$$\Delta V_{GB} = \frac{eP_{net}}{2\epsilon\epsilon_0} \cdot w^2, \tag{6.1}$$

where e is the elemental charge, P_{net} is the net doping density of the $Cu(In,Ga)Se_2$ (CIGSe) material, ϵ is the dielectric permeability of the CIGSe material, and ϵ_0 is the dielectric constant.

In Fig. 6.13 (a) the absolute values of the negative potential barriers from Fig. 6.12 are plotted as a function of the square of the corresponding NPD widths. As can be seen from

[12]Holes are the majority carriers. CIGSe is a p-type semiconductor.

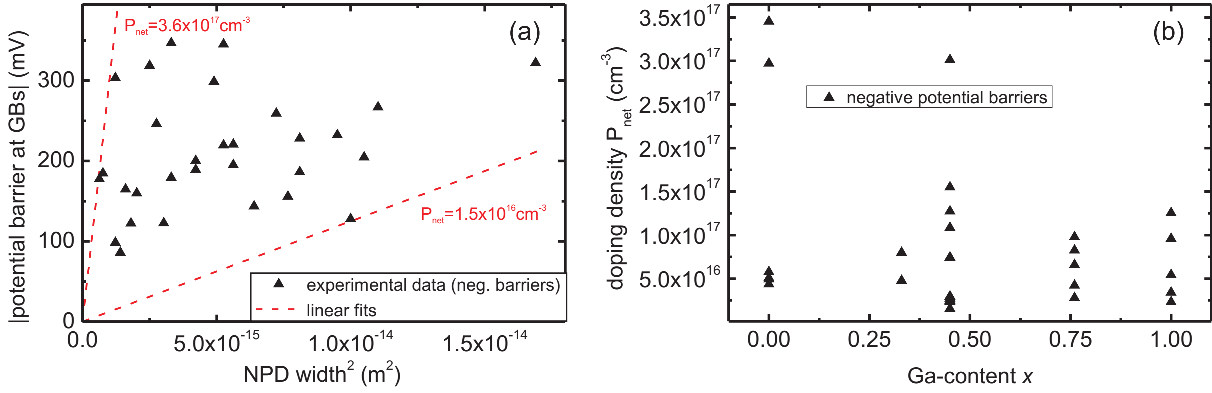

Figure 6.13: *(a) Absolute values of the negative potential barriers from Fig. 6.12 in dependence of the square of the corresponding NPD widths. The linear fits indicate maximum and minimum doping densities P_{net} of the CIGSe thin films. (b) Doping densities P_{net} of the negative potential barriers from Fig. 6.12 in dependence of the Ga-content.*

Eq. (6.1), a linear dependence between the potential barriers and the square of the NPD widths is expected from theory in the case of a constant doping density P_{net}. However, no linear dependence is observed in Fig. 6.13 (a). This finding suggests a non-constant doping density within the studied CIGSe thin films.
Based on Eq. (6.1) it is possible to roughly estimate lower and upper limits for the P_{net} of the CIGSe thin films[13]. From the linear fits depicted in Fig. 6.13 (a) one obtains variations in the doping density between $1.5 \times 10^{16}\text{cm}^{-3}$ and $3.6 \times 10^{17}\text{cm}^{-3}$. These numbers are in good agreement with doping densities of CIGSe thin films reported in the literature [15, 31–33].
In Fig. 6.13 (b) the doping densities in the vicinities of the negative GBs from Fig. 6.12 are plotted as a function of Ga-content. For this purpose, P_{net} was calculated individually for each GB via Eq. (6.1). No systematic dependence of the doping density on the Ga-content of the CIGSe thin films can be noticed in Fig. 6.13 (b).

With the help of the known doping densities in the vicinities of the GBs it is possible to calculate the charge per unit area Q_{SCR}, which is localized at the space charge regions at both sides of a GB [12]:

$$Q_{SCR} = -2eP_{net}w. \tag{6.2}$$

$|Q_{SCR}|$ must be equal to the charge per unit area Q_{GB}, which is localized at the GB. Considering the relation between Q_{GB} and the defect density P_{GB} at the GB,

$$Q_{GB} = eP_{GB}, \tag{6.3}$$

one can rewrite Eq. (6.1) as:

$$P_{GB} = \sqrt{\frac{8\epsilon\epsilon_0 P_{net}\Delta V_{GB}}{e}}. \tag{6.4}$$

[13] A dielectric permeability of $\epsilon = 11$ [88] was used for all calculations within this section.

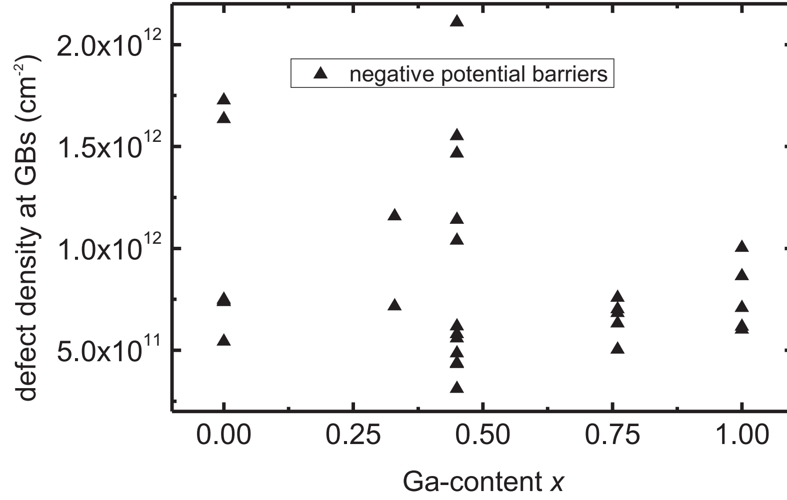

Figure 6.14: *Defect densities P_{GB} at the GBs with negative potential barriers from Fig. 6.12 in dependence of the Ga-content.*

In Fig. 6.14 the defect densities at the GBs with negative potential barriers from Fig. 6.12 are plotted in dependence of the Ga-content. For this purpose, the defect density was individually calculated for each GB via Eq. (6.4). A scattering of the defect density P_{GB} between $\approx 3.1 \times 10^{11}\text{cm}^{-2}$ and $2.1 \times 10^{12}\text{cm}^{-2}$ is observed. No systematic dependence of P_{GB} on the Ga-content can be noticed. The observed values for P_{GB} are in good agreement with defect densities at GBs of CIGSe thin films reported in the literature [31, 100].

Positive potential barriers

In the case of a positive potential barrier negative charge is localized at the GB. Free holes accumulate in the near GB region and compensate the negative charge (see Fig. 6.8 (a)). Here it is not possible to calculate the defect density P_{GB} individually for each GB, as one can not obtain the doping density P_{net} from the experimental data. However, one can give an estimate of the P_{GB} at GBs with positive potential barriers by assuming a doping density in the vicinity of the GBs similar to the one observed for negative potential barriers.

Considering the potential distribution across a GB with positive potential barrier (see Eq. (3.4)), the Poisson-equation (see Eq. (3.2)) can be rewritten as:

$$\frac{\Delta V_{GB}}{L_{Db}^2} \cdot \mathrm{e}^{-\frac{|l|}{L_{Db}}} = -\frac{\rho(l)}{\epsilon\epsilon_0}, \tag{6.5}$$

where $L_{Db} = \sqrt{\frac{\epsilon\epsilon_0 k_B T}{e^2 P_{net}}}$ is the Debye-length, $\rho(l)$ is the charge density of the holes accumulated in the vicinity of the GB, k_B is the Boltzmann-constant, and T is the absolute temperature.

Solving Eq. (6.5) for $\rho(l)$ and integrating the result from $l = 0$ to $l = \infty$ provides an expression for the charge per unit area Q_{Ac} , which is accumulated in the vicinity of a

GB:

$$Q_{Ac} = 2 \cdot \frac{\epsilon\epsilon_0 \Delta V_{GB}}{L_{Db}} = eP_{GB}. \tag{6.6}$$

The factor 2 accounts for the fact that the potential barrier extends to both sides of the GB.
Assuming an average potential barrier of +200mV (see Fig. 6.12), and an average doping density P_{net} of $5 \times 10^{16}\text{cm}^{-3}$ (see Fig. 6.13 (b)), one can estimate the defect density at positive potential barriers via Eq. (6.6) as:

$$P_{GB} \approx 1.4 \times 10^{12}\text{cm}^{-2}.$$

This defect density is in good agreement with defect densities observed at GBs with negative potential barriers, as shown in Fig. 6.14. Therefore, it is concluded that similar defect densities P_{GB} can be expected at GBs of CIGSe thin films in the case of both positive and negative potential barriers.

6.4.4 Electronic potential barriers at grain boundaries and solar cell performance

In Fig. 6.12 the potential barriers at grain boundaries (GBs) of the *chemically treated* $Cu(In,Ga)Se_2$ (CIGSe) thin films from Tab. 6.1 are plotted as a function of the Ga-content. No systematic dependence of the electronic GB properties on the Ga-content can be observed. A similar variation of potential barriers in the range from ≈ -350mV to $\approx +450$mV is found for all five thin films. Additionally, the appearance of GBs without a potential barrier also seems not to be correlated with the Ga-content. In Fig. 6.14 the defect densities P_{GB} at the GBs with negative potential barriers from Fig. 6.12 are depicted in dependence of the Ga-content. Again, no interrelation between P_{GB} and the Ga-content can be noticed.
Based on these results it is concluded that there is no correlation between the electronic properties of GBs and the Ga-content of CIGSe thin films. Consequently, it is not possible to explain the drop in device efficiency that is observed for CIGSe thin film solar cells with high Ga-content (see Tab. 6.1) by a change of the electronic properties of GBs in CIGSe thin films.

The similar frequency of occurrence of both positive and negative potential barriers at GBs (see Fig. 6.12) generally raises doubts about the validity of the "electronic barrier model" (see Sec. 3.2.1.3). Due to the downward band bending (see Fig. 6.8 (b)), GBs with negative potential barriers repel positive charge carriers (holes), while they attract negative charge carriers (electrons). This leads, according to the "electronic barrier model", to the development of conduction pathways for electrons (minority carriers) along the GBs to the n-type buffer/window layers, wherein the electrons are protected from recombination [84]. The appearance of positive potential barriers alongside of such a conduction pathway should repel the electrons from the GB into the grain interior, and consequently interrupt the conduction pathway. In the KPFM image of Fig. 6.15 one can see that both positive and negative potential barriers indeed occur side by side to each other. Hence, it

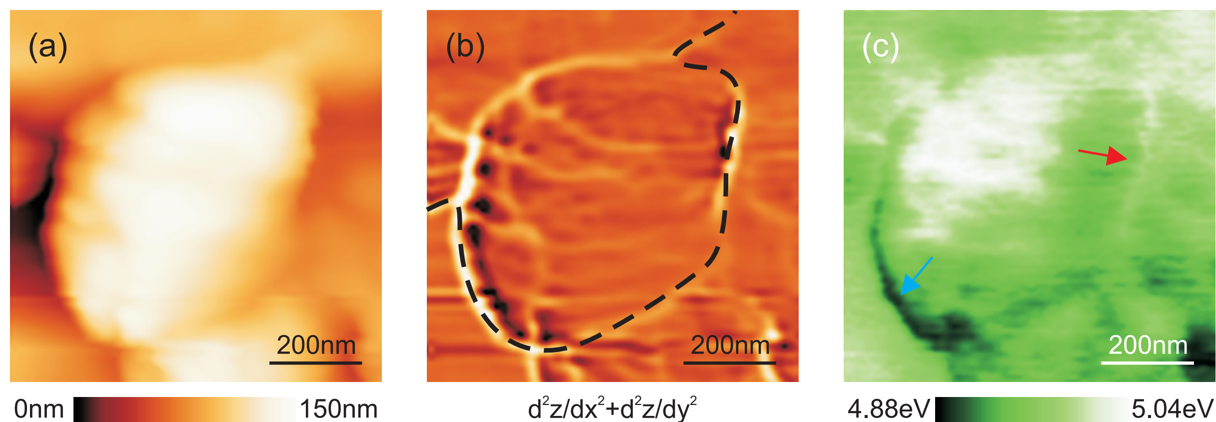

Figure 6.15: *800nm × 800nm KPFM image of the (a) topography, (b) Laplace-transformation of the topography, and (c) work function of a chemically treated CIGSe-45 thin film. A hypothetical conduction pathway for electrons is is indicated in (b) by black dashed lines. GBs with negative (positive) potential barriers are highlighted in (c) by a blue (red) arrow.*

seems unclear how our experimental findings can be aligned with the "electronic barrier model".

Numerical device simulations additionally challenge the validity of the "electronic barrier model". While Taretto et al. [92, 94] did not find any improvement of cell efficiency as a result of negative potential barriers at all, Gloeckler et al. [95] revealed that type inversion at GBs with negative potential barriers is necessary in order to observe a small positive effect of such GBs for solar cell efficiency. In any case, the simulations do not support the "electronic barrier model", as our results do not suggest that type inversion is prevalent at GBs of CIGSe thin films. As can be seen in Fig. 6.12, maximum negative potential barriers of ≈ -350mV are observed at GBs. However, type inversion requires negative potential barriers larger than ≈ -400mV, according to Refs. [94, 95].

In summery, it seems not plausible that the remarkable energy conversion efficiencies of CIGSe thin film solar cells are solely based on the existence of electronic potential barriers at the GBs of CIGSe thin films. Nevertheless, since CIGSe thin film solar cells undeniably reach remarkable efficiencies despite the frequent appearance of GBs, detrimental effects of the GBs, as observed for many materials used in solar cells (e.g. Si, GaAs [63–68]), seem rather unlikely. It might be possible to explain the properties of the GBs in CIGSe with one of the other GB models introduced in Sec. 3.2.1. However, the validity of these models could not be probed within this study.

As a final remark it should be pointed out that all experiments reported within this section were performed on the surface of CIGSe thin film absorbers. It is well known that the surface properties of CIGSe thin films differ from the bulk properties [44, 166, 167]. Consequently, it is conceivable that the electronic GB properties at the surface also differ from the GB properties in the bulk. However, it has not been possible up to now to correlate the electronic GB properties at the surface with those in the bulk, mainly because of the specific limitations of the various experimental techniques which need to be utilized to access such complementary information [99].

Nevertheless, even if it eventually turns out that the GB properties in the bulk differ from

those at the surface, the latter would still be of particular relevance, as the CIGSe surface forms the junction to the n-type buffer/window layer in CIGSe solar cells. This being said, a chemical modification of the electronic GB properties in the near surface region in the course of solar cell production seems also possible [168, 169].

6.5 Conclusions

The experiments reported within this chapter demonstrate that a moderate surface oxidation does not alter the electronic properties of grain boundaries (GBs) in $Cu(In,Ga)Se_2$ (CIGSe) thin films. By means of Kelvin probe force microscopy (KPFM) similar potential barriers at GBs were observed for both *as grown* and *chemically treated* (KCN etched) thin films. A slight increase in the frequency of occurrence of GBs without electronic potential barrier was detected after the chemical treatment. This finding is attributed to the removal of electronically active defect states in the course of the chemical treatment.

In general, a significant variation of potential barriers at GBs was observed. However, no systematic dependence of the potential barriers on the Ga-content was revealed. Under consideration of the averaging effect through the tip of the cantilever, which reduces the magnitude of potential barriers detected in KPFM measurements (see Chap. 5), the investigated GBs exhibited potential barriers in the range between ≈ -350mV and $\approx +450$mV. The results do not suggest that type inversion is prevalent at GBs with negative potential barriers.
The defect densities at the GBs of CIGSe thin films were determined based on our experimental results. Variations in the defect densities between $\approx 3.1 \times 10^{11}$cm^{-2} and $\approx 2.1 \times 10^{12}$cm^{-2} were found. Again, no dependence of the defect densities at GBs on the Ga-content was observed.
In summary, it is concluded that there is no correlation between the electronic properties of GBs and the Ga-content of CIGSe thin films. Consequently, it is not possible to explain the drop in device efficiency that is observed for CIGSe thin film solar cells with high Ga-content (see Tab. 6.1) by a change of the electronic properties of GBs in CIGSe thin films.

Based on the results presented within this chapter it generally appears unlikely that the remarkable energy conversion efficiencies of CIGSe thin film solar cells are solely based on the existence of potential barriers at the GBs of CIGSe thin films.

Chapter 7

Symmetry-dependence of electronic grain boundary properties in $Cu(In,Ga)Se_2$ thin films

The aspect of grain boundary (GB) symmetry (see Sec. 3.1) is frequently neglected in a discussion about the electronic properties of GBs in $Cu(In,Ga)Se_2$ (CIGSe) thin films [14, 84, 100, 105]. This mainly results from the fact that a consideration of GB symmetry is non-trivial. Theoretical investigations face the problem that there are no atomic models available for GBs in CIGSe[1]. Experimentally, on the other hand, it is very challenging to obtain complementary information about structural and electronic properties of GBs, as this generally requires the combination of various experimental methods on a microscopic scale.
Nevertheless, is seems important to consider the symmetry of GBs in the discussions, as there is evidence that it influences the GBs electronic properties. A difference in carrier recombination between highly symmetric $\Sigma 3$ GBs[2] and lower symmetric non-$\Sigma 3$ GBs was revealed by means of electron beam induced current measurements, as reported by Kawamura et al. [98] and Sadewasser et al. [99]. In Kelvin probe force microscopy (KPFM) studies Siebentritt et al. [91] did not detect any charged potential barrier at a $\Sigma 3$ GB in $CuGaSe_2$, while Hafemeister et al. [13] reported on a charged potential barrier of about -90mV at a $\Sigma 9$ GB of the same material. However, the latter two KPFM studies were conducted on epitaxially grown material, and the validity of the results for polycrystalline CIGSe is yet to be confirmed.

This chapter presents combined measurements of the structural and electronic properties of polycrystalline CIGSe thin films. Scanning electron microscopy, electron backscatter diffraction, and Kelvin probe force microscopy are employed to gather complementary information on a microscopic scale. Based on this information the locations of GBs in CIGSe are determined in a physically correct way. The chapter compares the obtained results to results of a GB localization solely based on the topography of KPFM images

[1]In order to incorporate grain boundaries in the calculations theorists rely on assumptions, for example the similarities between GBs and surface structures [9, 78], or GB models from materials with a similar crystal structure (e.g. CdTe) [11].
[2]See Sec. 3.1 for a definition of the Σ-value.

(see Sec. 6.2), and evaluates the correctness and selectivity[3] of the topography-based localization of GBs.
Furthermore, this chapter investigates the electronic properties of GBs in dependence of their symmetry. It examines the validity of the assumption that highly symmetric Σ3 GBs have a lower probability to exhibit charged potential barriers (see Sec. 6.3) than lower symmetric non-Σ3 GBs in CIGSe thin films.

7.1 Complementary information about structural and electronic properties on a microscopic scale

The experiments were performed on the CIGSe-0 thin film, which was introduced in Tab. 6.1. This sample was chosen, as it exhibits the largest grain size (≈ 1.3μm, see Fig. 6.4) of all thin films investigated within Chap. 6. The large grain size simplifies locating of the identical surface position by means of Kelvin probe force microscopy (KPFM), scanning electron microscopy (SEM), and electron backscatter diffraction (EBSD).

Prior to the KPFM measurements, which were conducted at first, the CIGSe-0 sample was etched in 0.15M aqueous Potassium cyanide (KCN) solution to remove surface oxides (see Sec. 2.2.3). Upon completion of the chemical treatment and during transport to the ultra high vacuum (UHV) conditions of the KPFM setup, the sample was kept in an environment of deionized water to avoid any surface oxidation. Subsequent to the introduction into the UHV environment, the sample was annealed at a temperature of ≈ 130°C for about 30 minutes to remove residual water.
After the KPFM experiments were completed the sample was introduced into the SEM setup which was used for both the SEM and EBSD experiments[4]. There, the identical surface area of the KPFM measurement was localized, and both SEM and EBSD measurements were performed.
A detailed description of how the locating of the identical surface area was achieved by means of the different experimental methods is provided in Sec. A.6.

In Fig. 7.1 KPFM topography and work function images (see Sec. 4.1), EBSD orientation distribution and pattern quality maps (see Sec. 4.2.2), and a SEM micrograph (see Sec. 4.2.1) from an identical surface area on the CIGSe-0 film are shown. The x-y dimensions of both the KPFM images and the EBSD maps were re-calibrated based on the dimensions of the SEM micrograph, as the original images were distorted due to a non-linear expansion of the piezo (KPFM), the non-perpendicular incidence of the electron beam on the surface (EBSD), and thermal drift (KPFM and EBSD). SEM micrographs are not subject to any of these effects. The electron beam hits the surface perpendicularly, and the recording time of a micrograph is short enough (≈ 30s) to not be affected by thermal drift. Consequently, the SEM micrograph is expected to reflect the accurate image dimensions.
In the KPFM topography and work function images in Fig. 7.1 (a) and (b) the locations

[3] It is investigated if GBs with lower symmetry are preferentially selected over highly symmetric GBs by means of a topography-based localization of GBs.
[4] The transport from the KPFM setup to the SEM/EBSD setup was conducted under ambient conditions.

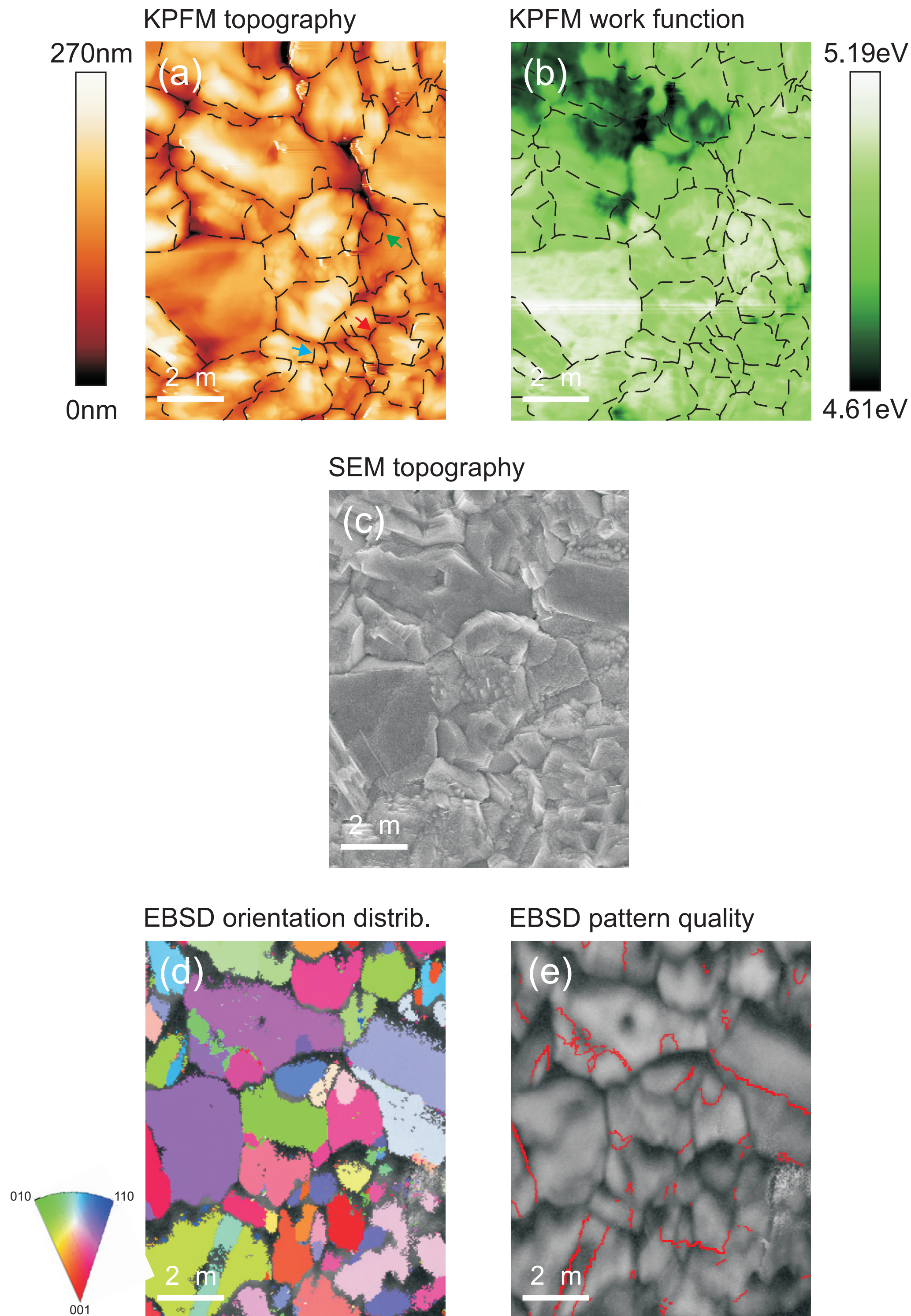

Figure 7.1: *9.0µm × 11.3µm images from an identical area on the CIGSe-0 thin film. (a) KPFM topography image, (b) KPFM work function image, (c) SEM micrograph, (d) EBSD orientation distribution map, and (e) EBSD pattern quality map. In (a) and (b) the locations of GBs are indicated by black dashed lines, as obtained through the EBSD orientation distribution map in (d). In (a) the locations of the GBs displayed in Fig. 7.2 are marked by colored arrows. In (e) Σ3 GBs are highlighted by red solid lines. Modified from [170].*

of GBs are indicated by black dashed lines. This information was obtained through the EBSD orientation distribution map depicted in Fig. 7.1 (d). Information about the symmetry of the GBs can be obtained from the EBSD pattern quality map, which is shown in Fig. 7.1 (e). There, Σ3 GBs are highlighted by red solid lines, while all other types of GBs can be noticed, because they show up as dark gray lines.

7.2 The localization of grain boundaries in Kelvin probe force microscopy

In the Kelvin probe force microscopy (KPFM) topography and work function images in Fig. 7.1 (a) and (b) the locations of grain boundaries (GBs) were determined based on the electron backscatter diffraction (EBSD) orientation distribution map depicted in Fig. 7.1 (d). This is a physically correct method of GB localization, as EBSD unambiguously determines the location of GBs by means of an analysis of the atomic lattice orientation. However, this approach is not always feasible, since combined KPFM and EBSD experiments are challenging and time-consuming; if, in first place, an EBSD setup is available at all.
An alternative approach to determine the locations of GBs is solely based on KPFM topography images. This method, which was introduced in Sec. 6.2, facilitates a quick

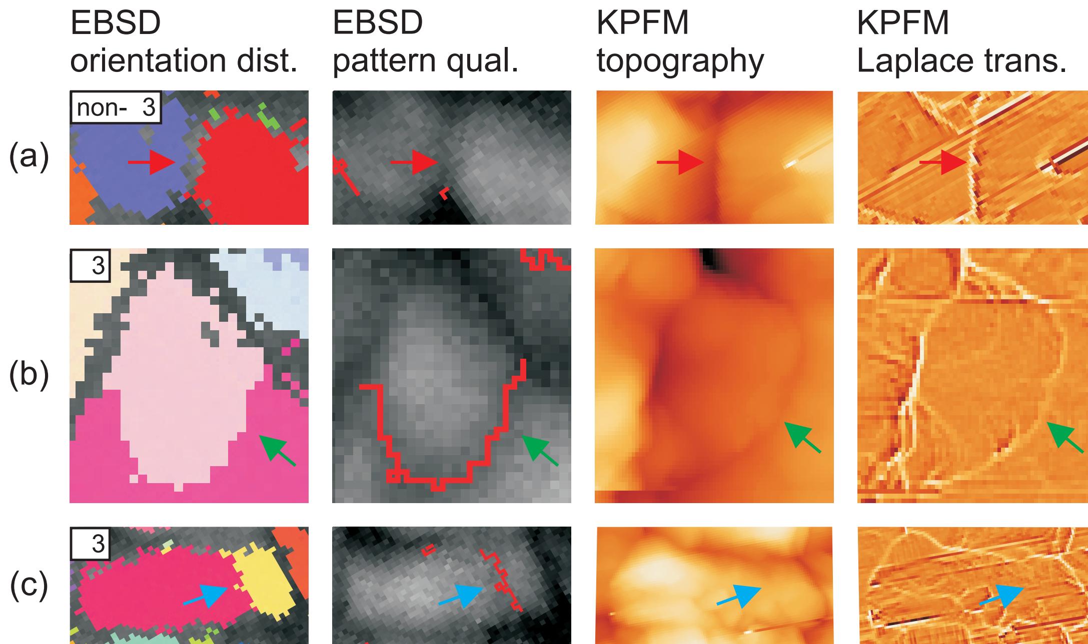

Figure 7.2: *EBSD orientation distribution and pattern quality maps as well as KPFM images of topography and Laplace transformed ($d^2z/dx^2+d^2z/dy^2$) topography of a: (a) non-Σ3 GB with topography feature, (b) Σ3 GB with topography feature, and (c) Σ3 GB without topography feature. Σ3 GBs are highlighted in the EBSD pattern quality map by solid red lines. The locations of the GBs are indicated in all images by colored arrows. The locations of the GBs can also be seen in Fig. 7.1 (a).*

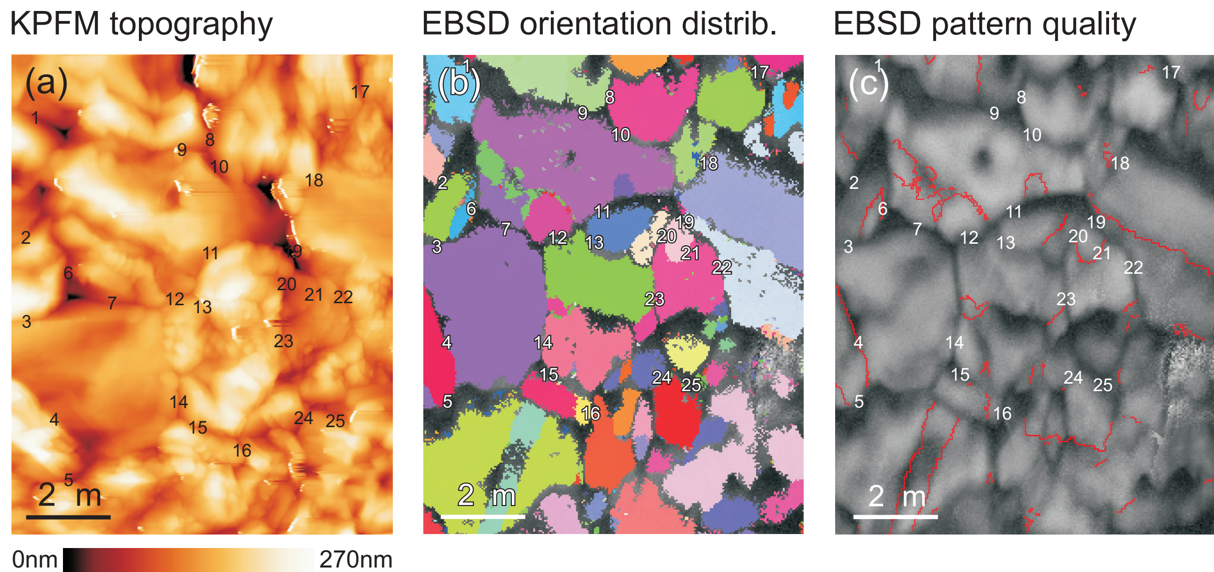

Figure 7.3: *9.0μm × 11.3 μm (a) KPFM topography image, (b) EBSD orientation distribution map, and (c) EBSD pattern quality map from an identical area on the CIGSe-0 thin film. In all images the locations of GBs, as determined solely based on the KPFM topography image in (a), are marked by numbers from 1 to 25. In (c) Σ3 GBs are highlighted by solid red lines.*

localization of GBs. Therefore, it is suited for extensive studies in which multiple samples need to be investigated (e.g. the study of Chap. 6). However, one drawback of this method is that it is not a physically precise method of GB localization. A misinterpretation of surface features as GBs, or a preferential selection of GBs with certain symmetry, can not be excluded.
In this section the two methods of GB localization mentioned above are compared to each other, in order to estimate the correctness and the selectivity of a topography-based localization of GBs.

In Fig. 7.2 cut-outs from various GBs of Fig. 7.1 are shown. The locations of these GBs are indicated in Fig. 7.1 (a) by colored arrows. Fig. 7.2 (a) displays a randomly orientated non-Σ3 GB, as can be noticed from the EBSD pattern quality map. The GB exhibits a distinct topography feature, which is clearly visible in both the KPFM topography and Laplace transformed topography image. In Fig. 7.2 (b) a highly symmetric Σ3 GB is depicted. Despite the high symmetry, the GB shows a distinct topography feature, which can be detected in the KPFM topography images. In contrast, the Σ3 GB shown in Fig. 7.2 (c) does not exhibit any topography feature. The GB cannot be noticed in the KPFM topography images.
The 3 GBs depicted in Fig. 7.2 point out that it is not possible to detect every single GB present in CIGSe thin films based on KPFM topography images. However, Fig. 7.2 also demonstrates that even Σ3 GBs can exhibit a sufficient topography feature to be localized by means of a topography-based analysis, despite their high symmetry.

In Fig. 7.3 (a) the same KPFM topography image of Fig. 7.1 is shown. This time, though, the locations of GBs were not determined based on the EBSD orientation distribution map, but on the KPFM topography image itself. For the localization of GBs the criteria

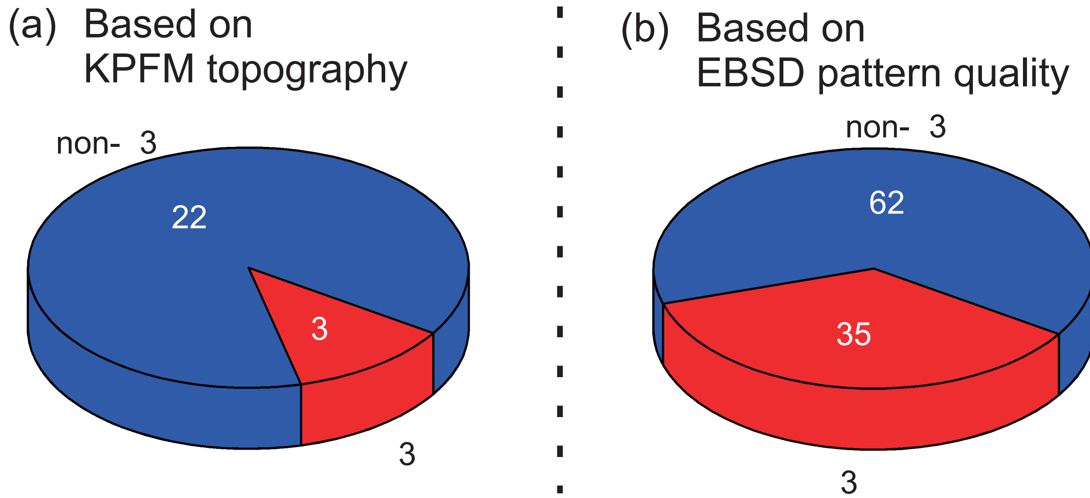

Figure 7.4: *(a) Symmetry of the 25 GBs, which were identified solely based on the KPFM topography image in Fig. 7.3 (a). Symmetry of the 97 GBs, which were determined based on the EBSD orientation distribution map in Fig. 7.1 (d). In both cases, the symmetry information was obtained through the EBSD pattern quality map in Fig. 7.3 (b).*

given in Sec. 6.2 were applied.
The identified GBs were analyzed by comparison to the EBSD maps shown in Fig. 7.3 (b) and (c). This comparison to EBSD measurements of the same area allows a classification of the identified GBs into three categories:

- $\Sigma3$ GBs.
- non-$\Sigma3$ GBs.
- Surface features wrongly misinterpreted as GBs.

Additionally, the EBSD-based localization of GBs was evaluated as well. Here, every contact of two grains in the EBSD orientation distribution map in Fig. 7.3 (b) was regarded as a GB. The GBs were classified into $\Sigma3$ GBs and non-$\Sigma3$ GBs. A misinterpretation of surface features as GBs can not occur, since EBSD is sensitive to the crystal lattice structure.

The results of the analyses are shown in Fig. 7.4. The locations of 25 GBs were determined based on the KPFM topography image in Fig. 7.3 (a), as can be seen in Fig. 7.4 (a). About 10% of the localized GBs were identified as $\Sigma3$ GBs. All other GBs exhibited a lower non-$\Sigma3$ symmetry. No surface feature was wrongly misinterpreted as GB. The result of the analysis of the EBSD based localization of GBs is displayed in Fig. 7.4 (b). By means of this physically correct evaluation method 97 GBs were detected within the identical surface area of Fig. 7.3 (a). More than 35% of the GBs exhibited a $\Sigma3$ symmetry, while all other GBs revealed a non-$\Sigma3$ symmetry.
The results shown in Fig. 7.4 illustrate that in a topography-based localization no surface feature is wrongly misinterpreted as GB, if the strict criteria of Sec. 6.2 are applied. The results also suggest that lower symmetric non-$\Sigma3$ GBs are preferentially selected over highly symmetric $\Sigma3$ GBs by means of this localization method.

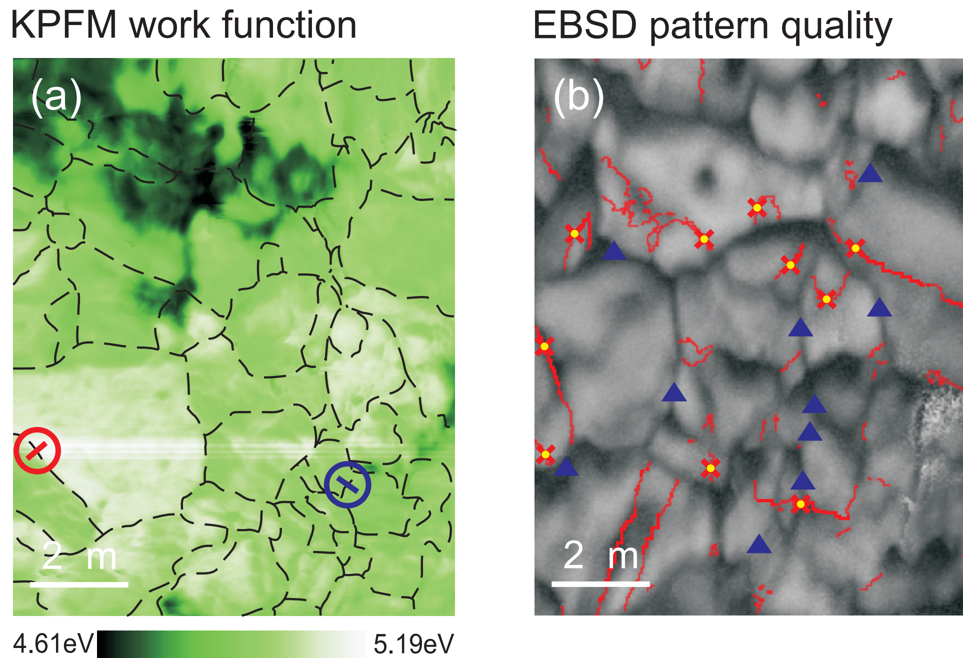

Figure 7.5: *9.0μm × 11.3 μm (a) KPFM work function image and (b) EBSD pattern quality map from an identical area on the CIGSe-0 thin film (see Tab. 6.1): In (a) the locations of GBs are indicated by black dashed lines, as obtained through the EBSD orientation distribution map in Fig. 7.1 (d). The positions of the line profiles shown in Fig. 7.6 are indicated by red (Σ3) and blue (non-Σ3) circles, respectively. In (b) Σ3 GBs are highlighted by red solid lines. The locations of the Σ3 GBs analyzed in Fig. 7.7 are indicated by red crosses with yellow dots. The locations of the non-Σ3 GBs analyzed in Fig. 7.6 are indicated by blue triangles.*

7.3 Electronic potential barriers at grain boundaries

This section presents an analysis of the electronic properties of grain boundaries (GBs) in dependence of their symmetry[5]. For the analysis, which was based on the method introduced in Sec. 6.3, the information provided in Fig. 7.5 was used.
In Fig. 7.5 (a) and (b) a Kelvin probe force microscopy (KPFM) work function image and an electron backscatter diffraction (EBSD) pattern quality map from an identical area on the CIGSe-0 thin film (see Tab. 6.1) are shown[6]. The positions of grain boundaries (GBs), as determined through the EBSD orientation distribution map in Fig. 7.1 (d), are indicated in Fig. 7.5 (a) by black dashed lines. The EBSD pattern quality map in Fig. 7.5 (b) provides complementary information about the symmetry of the GBs.

In Fig. 7.6 topography and work function line profiles across typical Σ3 and non-Σ3 GBs are shown. The positions of these GBs are indicated in Fig. 7.5 (a) by red and blue circles, respectively. The topography profile across the Σ3 GB in Fig. 7.6 (a) reveals a step of ≈ 100nm directly at the GB. Such steps are together with valley-like transitions the most frequent topography feature observed at GBs in CIGSe. The corresponding work function profile in Fig. 7.6 (b) exhibits a difference of about 150meV between both grains. This

[5]A distinction is made between Σ3 GBs and non-Σ3 GBs.
[6]The identical images can be seen in Fig. 7.1.

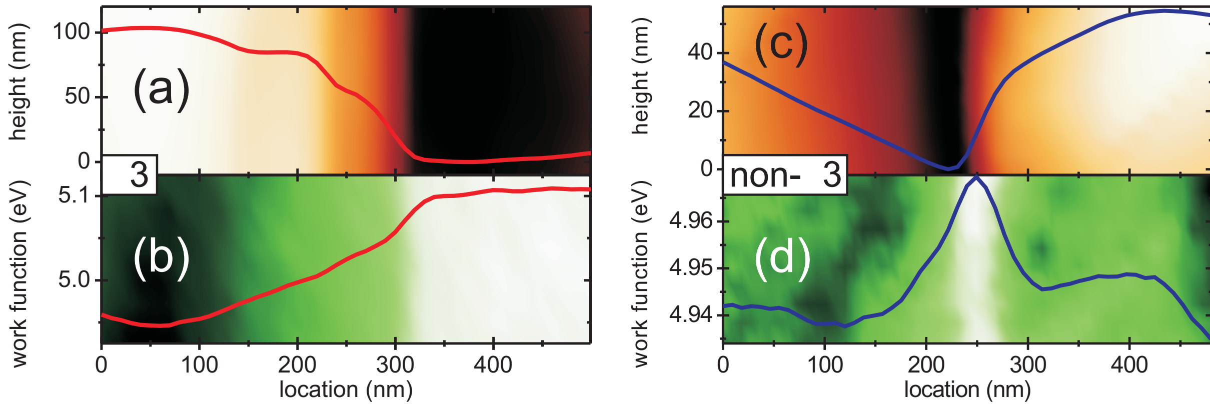

Figure 7.6: *KPFM line profiles (10 line average) of (a) topography and (b) work function across a typical Σ3 GB. KPFM line profiles of (c) topography and (d) work function across a typical non-Σ3 GB with positive potential barrier (see Fig. 6.8). The background of the averaged line profiles shows images of the corresponding surface area. The positions of the profiles are indicated in Fig. 7.1 (a) and (b) by red and blue circles, respectively. Modified from [170].*

difference is caused by different surface facets on both sides of the GB [45]. However, directly at the GB there is no evidence for the presence of a potential barrier, as it would result in an additional peak or dip in the work function profile, depending on the sign of the barrier (see Fig. 6.8). It was previously shown that KPFM is capable of resolving such additional fluctuations [91].
The topography profile across the non-Σ3 GB in Fig. 7.6 (c) yields a valley-like transition from one grain to the other. In the work function profile in Fig. 7.6 (d) a distinct peak of +30meV can be noticed right at the GB. This peak is evidence for a positive potential barrier (+30mV) caused by negative charges located at the GB [79, 100].

One difficulty with the analysis of Σ3 GBs was their exact localization in KPFM topography images. Due to their high symmetry, Σ3 GBs generally exhibit a less distinct topography feature compared to non-Σ3 GBs. While some Σ3 GBs still showed sufficient topography feature to be identified directly in the KPFM topography image (e.g. in Fig. 7.2 (b) and Fig. 7.6 (a)), some Σ3 GBs could only be evaluated indirectly by their position relative to characteristic topography features. A few Σ3 GBs could not be evaluated at all, due to a lack of precise localization.
Ultimately, it was possible to evaluate the electronic properties of 10 different Σ3 GBs. The locations of these GBs are indicated in Fig. 7.5 (b) by red crosses with yellow dots. In addition, the electronic properties of 10 non-Σ3 GBs were analyzed as well. Their locations are indicated in Fig. 7.5 (b) by blue triangles.
Fig. 7.7 displays the detected potential barriers for both the analyzed Σ3 GBs and non-Σ3 GBs. 9 out of 10 Σ3 GBs did not yield any potential barrier; only one Σ3 GB exhibited a potential barrier of −45mV. For non-Σ3 GBs, in contrast, only 4 out of 10 GBs did not reveal any evidence for potential barriers. The remaining 6 GBs exhibited both negative and positive potential barriers, in a range from −90mV to +37mV.
Altogether, Fig. 7.7 shows an obvious pattern in terms of the electronic properties of grain boundaries. While almost all Σ3 GBs did not exhibit a potential barrier, at more than 50% of the non-Σ3 GBs a potential barrier was detected. Even if the analysis does

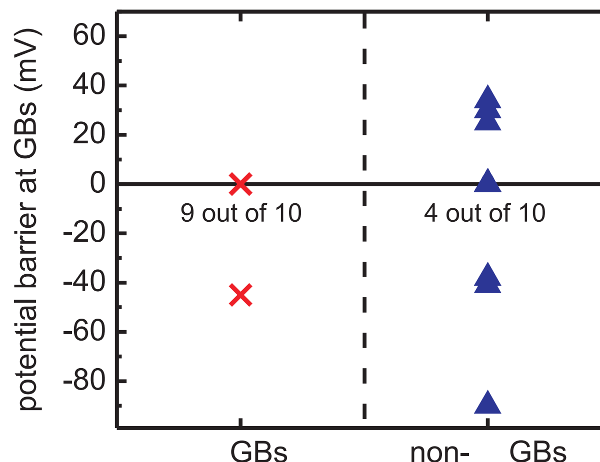

Figure 7.7: *Electronic properties of GBs in the CIGSe-0 thin film, with a distinction made between Σ3 GBs and non-Σ3 GBs. The black numbers indicate the number of GBs without any potential barrier. Modified from [170].*

not satisfy any statistical approach, it still appears obvious that Σ3 GBs have a lower probability to possess a electronic potential barrier than non-Σ3 GBs.

This result can be understood, as GBs with higher symmetry are expected to have a lower density of defects compared with lower-symmetric GBs. The defect density on the other hand is related to the potential barriers at GBs, as it is assumed that charged defect states are a main contributer to these barriers [79, 100].
The assumption of a general symmetry-dependence of the electronic properties of GBs, i.e. a correlation between the particular symmetry of a GB and its potential barrier which is also valid for GBs with symmetries lower than Σ3, can help to explain the large variations of potential barriers observed in Fig. 6.12 and Fig. 7.7 (for non-Σ3 GBs). For the analysis presented in these figures the symmetry of the GBs was not considered. It seems likely that the analyzed GBs exhibited various symmetries, which would explain the obtained results, based on the assumption mentioned above.

7.4 Conclusions

The results of this chapter represent the first combined study of Kelvin probe force microscopy, scanning electron microscopy, and electron backscatter diffraction measurements on $Cu(In,Ga)Se_2$ (CIGSe) thin films.
Based on complementary information about the structural and electronic properties on a microscopic scale, the accuracy of a topography-based localization of GBs in CIGSe thin films was investigated. It could be revealed that lower symmetric non-Σ3 GBs are preferentially selected over highly symmetric Σ3 GBs by means of this method, and that no surface feature is wrongly misinterpreted as grain boundary.
The analysis of the electronic properties of GBs in dependence of their symmetry revealed that highly symmetric Σ3 GBs have a lower probability to possess a charged potential barrier than lower symmetric non-Σ3 GBs. This symmetry-dependence can help to ex-

plain the variations of the potential barriers which are observed at GBs in polycrystalline CIGSe thin films [83, 100].

Chapter 8

Conclusions

The goal of this thesis was to improve the understanding of the electronic properties of grain boundaries (GBs) in polycrystalline $Cu(In,Ga)Se_2$ (CIGSe) thin films. A particular question of interest was the role of the electronic properties of GBs with respect to the decrease in device efficiency that is observed for CIGSe thin film solar cells with a high Ga-content. Another focus of this thesis was on the relationship between the symmetry and the electronic properties of GBs.

Kelvin probe force microscopy (KPFM) is the main experimental method used in the course of this thesis. KPFM allows it to simultaneously gather information about both the topography and electronic properties of individual GBs in CIGSe thin films. To increase the understanding of the data collected by KPFM, an extensive study about "Kelvin probe force microscopy at nanoscale potential distributions (NPDs)" (see Chap. 5) was conducted. For this purpose a Kelvin probe force spectroscopy routine was developed that allows for the study of the information value of KPFM measurements at NPDs (e.g. GBs), independent of electronic inhomogeneities of the KPFM tip or the sample surface. With the help of this routine a significant averaging effect of the work function signal of NPDs in KPFM measurement was revealed. The results of this thesis demonstrate that the magnitude of this averaging effect depends on various geometry parameter of the experimental setup, namely the tip geometry, the width of a NPD, and the tip-sample distance. An influence of the topography feature of a NPD on the averaging effect could be excluded. By means of complementary finite element method simulations it was possible to quantify the magnitude of the averaging effect in dependence of the various geometry parameters. This enables quantitative comparison among various KPFM experiments performed at NPDs and to theory.

In order to investigate the "electronic grain boundary properties in $Cu(In,Ga)Se_2$ thin films with various Ga-contents" (see Chap. 6), CIGSe thin films with various Ga-contents were grown by means of three stage co-evaporation processes. Both *as grown* as well as *chemically treated* (KCN etched) thin films were investigated by means of KPFM. The chemical treatment was employed to remove surface oxides from the CIGSe thin films. No difference in the electronic GB properties was found with or without the chemical treatment. Therefore, it is concluded that a moderate surface oxidation[1] does not alter the electronic properties of GBs. Both positive and negative potential barriers at

[1]Exposure time of the thin films to ambient air $<\approx 24h$.

GBs were observed. Under consideration of the averaging effect through the tip of the cantilever, which reduces the magnitude of potential barriers detected in KPFM measurements (see Chap. 5), the investigated GBs exhibited potential barriers in the range between ≈ -350mV to $\approx +450$mV. Additionally, a significant number of GBs did not exhibit any potential barrier. The results do not yield any systematic dependence of the potential barriers on the Ga-content. Furthermore, our experiments revealed a large variation of the defect densities at GBs between $\approx 3.1 \times 10^{11}\text{cm}^{-2}$ and $\approx 2.1 \times 10^{12}\text{cm}^{-2}$. However, no dependence between the defect densities at GBs and the Ga-content could be observed as well. Based on these results it is concluded that there is no correlation between the electronic properties of GBs and the Ga-content of CIGSe thin films. Consequently, one cannot explain the decrease in device efficiency that is observed for CIGSe thin film solar cells with a high Ga-content (see Tab. 6.1) by a change of the electronic properties of GBs in the CIGSe thin films.

The "symmetry-dependence of electronic GB properties in Cu(In,Ga)Se_2 thin films" (see Chap.7) was studied by means of combined Kelvin probe force microscopy and electron backscatter diffraction (EBSD) measurements. The combination of the two experimental methods allowed it to gather complementary information about both the structural and electronic properties of individual GBs in CIGSe thin films. With the help of this information it was possible to investigate the dependence between the symmetry of a GB and the associated potential barrier. It was revealed that highly symmetric $\Sigma3$ GBs have a lower probability to possess charged potential barriers than lower symmetric non-$\Sigma3$ GBs. The assumption of a general symmetry-dependence of the electronic properties of GBs in CIGSe, i.e. a correlation between the particular symmetry of a GB and its potential barrier that is also valid for GBs with symmetries lower than $\Sigma3$, could help to explain the large variations of potential barriers observed at GBs in polycrystalline CIGSe thin films.

In summary, the results reported in this thesis document large variations of the electronic properties of GBs in CIGSe thin films. Consequently, one should not unify the electronic properties of GBs in CIGSe thin films. One particular aspect that influences the electronic properties of GBs is their symmetry, according to the results of Chap. 7. A good way to further increase the understanding about this aspect seems the analysis of individual GBs under consideration of their atomic structure. The combination of experimental techniques with high spatial resolution (e.g. scanning probe microscopy techniques, transmission electron microscopy techniques) appears to be well suited for this challenge, but is a highly time consuming endeavor.

Appendix A

Appendix

A.1 KPFM and KPFS at nanoscale potential distributions: A comparison of methods

In Chap. 5 Kelvin probe force spectroscopy (KPFS) is applied to gather information about the averaging effect of the work function signal of nanoscale potential distributions (NPDs) in Kelvin probe force microscopy (KPFM) experiments. This study assumes that the information gathered by means of KPFS and KPFM is equivalent. In this appendix it is investigated if this assumption is valid.

A first, qualitative comparison between KPFS and KPFM can be achieved by imaging an identical NPD with both techniques. In Fig. A.1 topography and contact potential difference (CPD) images of an electronically active GB (*GB 1* from Chap. 5) are shown, imaged by means of both KPFS[1] and KPFM. Both the KPFS and KPFM topography images in Fig. A.1 (a) and (c) yield a similar valley-like transition from one grain to the other. Such a transition is a typical feature of a GB in Cu(In,Ga)Se_2. The corresponding CPD images in Fig. A.1 (b) and (d) also reveal similar information. The lower work function of the NPD is clearly resolved by both KPFS and KPFM. The shape and depth of the NPD in both images is similar as well. A small drift in x-y-direction in the KPFS images becomes apparent by comparison to the KPFM images. It is caused by the long running time ($\approx$ 15h) of the KPFS grid-spectroscopy.

However, the images of Fig. A.1 only demonstrate the similarity of KPFS and KPFM for a single tip-sample distance. To control if the distance dependent information obtained by KPFS can be transfered to KPFM experiments, the distance dependence of the work function signal ($\Delta\Phi$) of a NPD at the edge of a surface step on p-type GaAs(110) (see Fig. A.2) was investigated by means of both KPFM and KPFS. Please note that the surface step is non of the surface steps investigated in Chap. 5. Also, unlike all KPFM measurements shown in the main chapters of the thesis this experiment was not conducted with a cantilever with Pt-Ir coated Si tip, but with a cantilever with pure Si tip which was sputtered prior to the measurements.

[1] 1225 KPFS spectra were taken on a 35pts×35pts grid around the GB of interest. Images were reconstructed from the entirety of the single spectra (see Sec. 5.1 for details about KPFS).

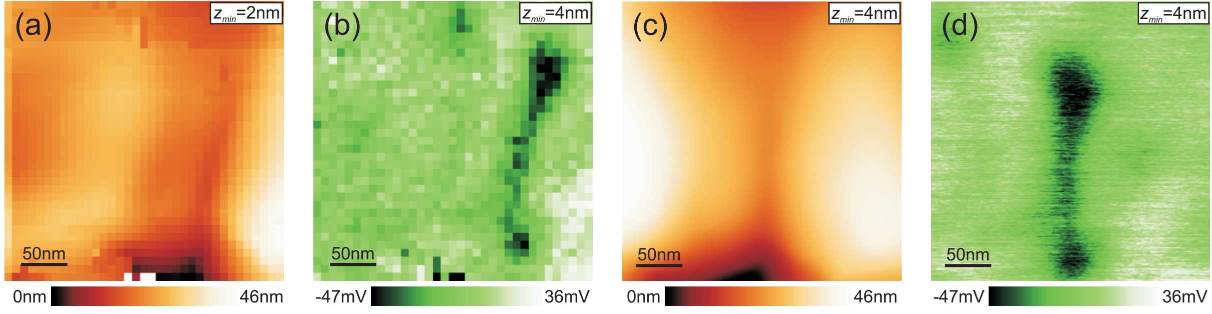

Figure A.1: *300nm × 300nm topography and contact potential difference (CPD) images at a grain boundary of a $CuIn_{0.7}Ga_{0.3}Se_2$ thin film obtained by (a), (b) KPFS and (c), (d) by KPFM. The corresponding tip-sample distances of the images are provided as insets. A "plane"-filter was applied to all CPD images for better comparison.*

To collect distance dependent information of the NPD work function signal based on KPFM measurements, 500nm KPFM line profile images (Δf, topography, work function) across the surface step were recorded. To record the line profile images shown in Fig. A.3 the KPFM's y-axis was kept constant during the measurement and the same line profile in x-direction was scanned repeatedly. While the image was recorded, the Δf setpoint (see Sec. 4.1.1) was increased from -35Hz to -0.5Hz in a stepwise manner, as can be noticed in Figs. A.3 (a) and (b). Since the frequency shift Δf is directly related to the tip-sample distance (see Fig. 5.4 (a)), it is possible to obtain the distance dependent $\Delta\Phi$ signal from the data in Fig. A.3. For this purpose 10 work function line profiles across the NPD were extracted from Fig. A.3 (d) for each Δf setpoint and averaged to reduce the noise level. From the averaged line profiles the NPD work function signal was extracted (see Sec. 6.3). In a last step the Δf setpoints were converted to absolute tip-sample distances.
The distance dependence of the NPD work function signal was also studied by means of KPFS. For the KPFS measurements the experimental routine described in Sec. 5.1.1 was applied at the identical location of Fig. A.3.

Fig. A.4 displays the distance dependence of the NPD work function signal, as obtained by means of both KPFM and KPFS. It is clearly seen that equivalent information is gathered by the two methods, as the observed distance dependence is nearly identical. Furthermore, the advantages of KPFS over KPFM which are mentioned in Sec. 5.1.1 become obvious from Fig. A.4. Both a higher density of data points and a wider range of tip-sample distances was accessible by KPFS in comparison to KPFM.

In summary, it could be shown that Kelvin probe force microscopy and Kelvin probe

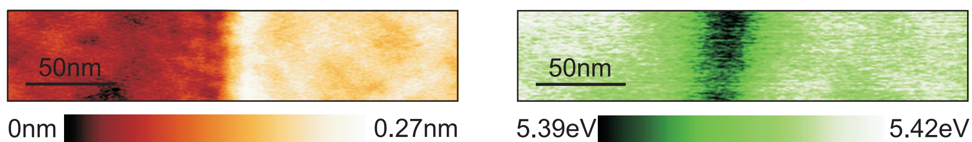

Figure A.2: *250nm × 50nm KPFM images of (a) topography and (b) work function at a p-type GaAs(110) surface step, taken at a tip-sample distance of $z_{min} = 2nm$.*

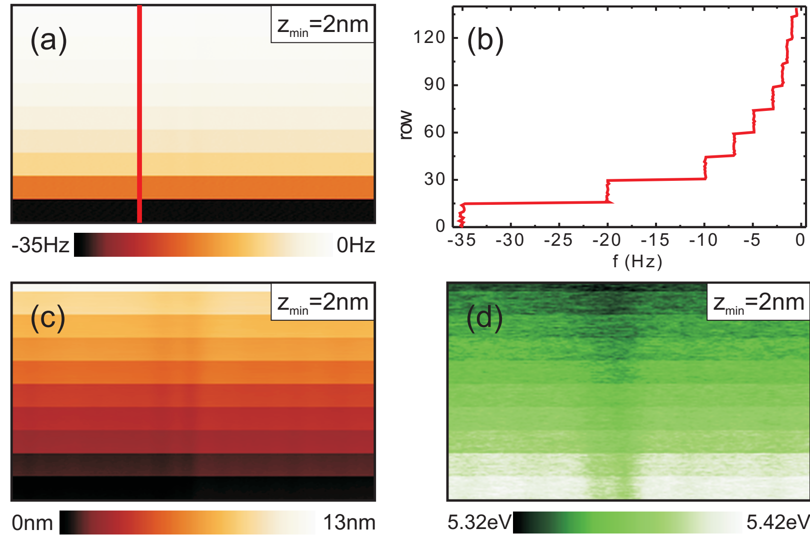

Figure A.3: *500nm KPFM line profile images of (a) Δf, (c) topography, and (d) work function across the p-type GaAs(110) surface step shown in Fig. A.2. (b) shows a line profile across the frequency shift image in (a), indicated by the red line. The tip-sample distance was increased during the measurement, starting at a minimum tip-sample distance $z_{min} = 2nm$ (at Δf=-35Hz).*

force spectroscopy gather identical information about work function signals at nanoscale potential distributions. Consequently, it is adequate to study the averaging effect of the work function signal at nanoscale potential distributions in Kelvin probe force microscopy by means of Kelvin probe force spectroscopy.

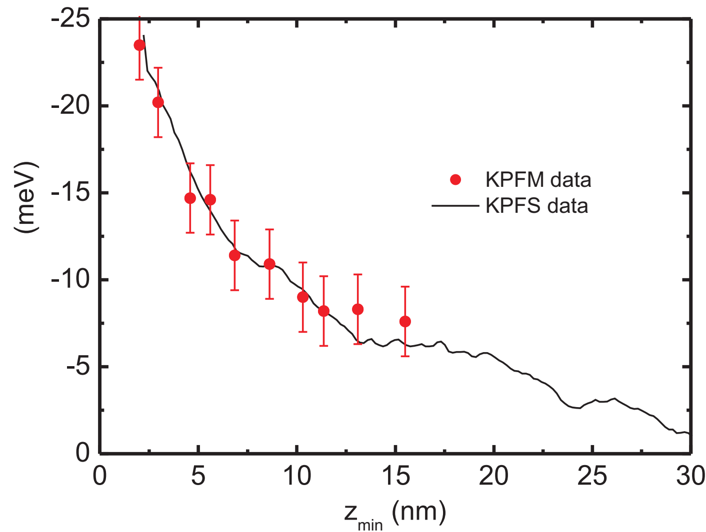

Figure A.4: *Distance dependence of the NPD work function signal ($\Delta\Phi$), recorded at the p-type GaAs(110) surface step shown in Fig. A.2. The KPFM data are displayed by red dots [171]. The KPFS difference spectrum is displayed by a black line.*

A.2 KPFS experimental parameters

The following parameters were used for the KPFS experiments described in Chap. 5:

z averaging time :	50ms	*End settling time* :	15ms
Initial settling time :	15ms	*Z control time* :	200ms
Max. slew rate :	200nm/s	*Resolution* :	1024pts
Settling time :	200μs	*Sweep distance* :	500nm
Integration time :	15ms	*Sweep time*	20.95s

Function of the individual parameters [172]:

- *z* **averaging time:** Duration over which the *z*-position is averaged. After the averaging time, the *z*-controller is set to hold and the tip is placed at the averaged position.
- **Initial settling time:** Time to wait after the tip has moved to the starting point of the sweep.
- **Max. slew rate:** Maximum rate at which the tip position changes
- **Settling time:** Time to wait between moving the tip to a new *z* level and starting to acquire data.
- **Integration time:** Time during which the data are acquired and averaged.
- **End settling time:** Time to wait after the sweep has finished and the tip has moved back to its initial position.
- *Z* **control time:** Time during which the *z* controller is enabled once a sweep has finished.
- **Resolution:** Number of measurement points acquired during a sweep.
- **Sweep distance:** Distance, at which the tip is retracted during a sweep, relative to the *feedback* distance.
- **Sweep time:** Time taken to acquire a sweep. This value only indicates the time needed for the actual sweep; *z* averaging time and *z* control time are not included.

A.3 KPFS simulation parameters

	Fig. 4.7/ Fig. 4.8	**Fig. 5.7**	**Fig. 5.10**	**Fig. 5.11/ Fig. 6.11**	**Fig. 5.13**	**Fig. 5.14**
NPD width (nm)	65	65	65	various	65	65
NPD depth (V)	-1	-1	-1	-1	-1	-1
Tip radius r (nm)	30	10	various	10	10	30
Open. angle θ (°)	10	30	various	30	30	10
Surf. topography	yes	no	no	no	no	various

Table A.1: *Parameters used for the simulations displayed in the respective figures.*

A.4 NPD width dependent averaging in KPFM: Fit function

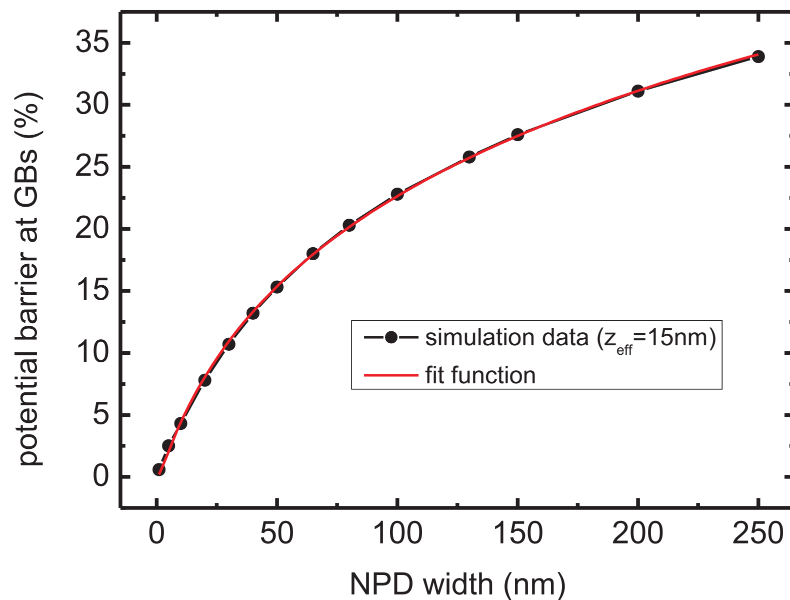

Figure A.5: *The simulation data depicted in Fig. 6.11 is shown (black dots). Additionally, the function $y = ax^{bx^{-c}}$, which was used to fit the experimental data, is depicted (red line).*
Fit parameters: $a = 123.70486$, $b = 0.00232$, $c = 0.2367$.

A.5 Measurement inaccuracy in the determination of a potential barriers at grain boundaries by KPFM

The measurement inaccuracy in the determination of potential barrier dimensions by Kelvin probe force microscopy (KPFM) is discussed with the help of the example shown in Fig. A.6.

Potential barrier

The potential barrier ΔV_{GB} is defined as:

$$\Delta V_{GB} = \frac{(\Phi(\mathrm{GB}) - \Phi(\mathrm{grain\ 1})) + (\Phi(\mathrm{GB}) - \Phi(\mathrm{grain\ 2}))}{2 \cdot e}, \tag{A.1}$$

where Φ is the work function at the specific features (grain 1+2, GB) indicated in Fig. A.6, and e is the elemental charge.
The inaccuracy in the determination of the work function at a specific feature mainly results from an inaccuracy in the determination of the feature's lateral position. The resulting inaccuracy is estimated as $\delta\Phi = \pm$ 10meV for each feature.
Consequently, the measurement inaccuracy in the determination of ΔV_{GB} is given by:

$$\delta\Delta V_{GB} = \pm\frac{\sqrt{(10\mathrm{meV})^2 + (10\mathrm{meV})^2 + (10\mathrm{meV})^2 + (10\mathrm{meV})^2}}{2 \cdot e} = \pm 10\mathrm{mV}. \tag{A.2}$$

Potential width

The potential width w is defined as:

$$w = \frac{l(\mathrm{grain\ 2}) - l(\mathrm{grain\ 1})}{2}, \tag{A.3}$$

where l is the location of the specific features (grain 1+2) indicated in Fig. A.6.
The inaccuracy in the determination of the location l of a specific feature results from the inaccuracy in the determination of its lateral position, and from the point-to-point distance between two neighboring measurement points.
The inaccuracy in the determination of the lateral position of a feature is estimated as ±10nm for each feature. The point-to-point distance in the KPFM line profiles is 10nm, which results in an inaccuracy for each measurement point of ±5nm.
Consequently, the measurement inaccuracy in the determination of the location l of a specific feature is given by:

$$\delta l = \pm\sqrt{(5\mathrm{nm})^2 + (10\mathrm{nm})^2} \tag{A.4}$$

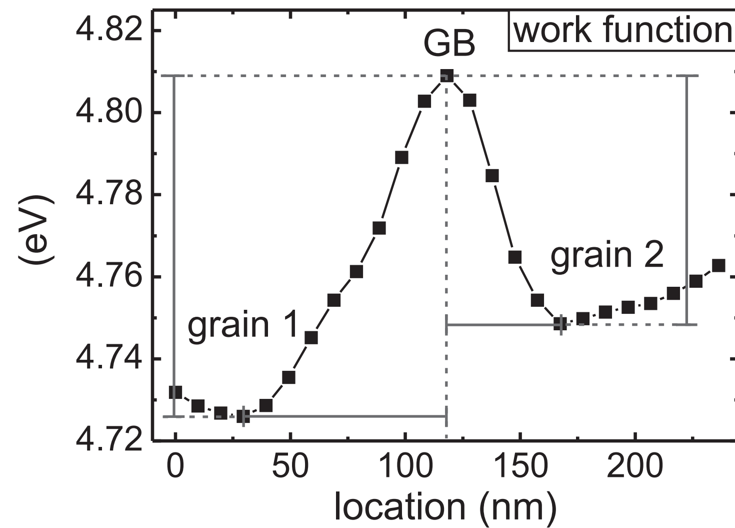

Figure A.6: *Averaged line profiles (10 neighboring lines were averaged) of the work function across the GB from Fig. 6.7. This line profile is also displayed in Fig. 6.7.*

Hence, the measurement inaccuracy in the determination of w is given by:

$$\delta w = \pm \frac{\sqrt{(\sqrt{(5\text{nm})^2 + (10\text{nm})^2})^2 + (\sqrt{(5\text{nm})^2 + (10\text{nm})^2})^2}}{2} = \pm 8\text{nm} \qquad \text{(A.5)}$$

A.6 Localization of an identical surface position in the KPFM setup and the SEM setup

The localization of an identical surface position in both the Kelvin probe force microscopy (KPFM) and the scanning electron microscopy (SEM) setup was a major challenge of the study on the symmetry-dependence of electronic grain boundary properties presented in Chap. 7. In this section details about the combined KPFM and SEM measurements are provided.

Prior to the introduction into the KPFM setup various patterns were scratched into the surface of the CIGSe-0 sample (see Tab. 6.1), as can be seen in Fig. A.7 (a) and (b). Inside the microscope the cantilever of the KPFM was positioned as close as possible to one of the patterns (in $x-y$-direction). Optical access to the sample was provided through the lense-optics of the KPFM setup. In Fig. A.7 (c) the same surface position shown in Fig. A.7 (b) is displayed, as seen through these optics; the position of the KPFM cantilever is indicated by a black line. The cantilever was approached towards the sample (in z-direction), until a predefined frequency shift Δf was established (see Sec. 4.1.1). With the feedback loop enabled the cantilever was further approached towards the pattern (in $x-y$-direction), until the edge of the pattern was reached; the edge was identified by a step in surface topography of $\approx 2\mu$m, which originates from the removal of the CIGSe layer.
For the actual KPFM measurements the cantilever was positioned $\approx 20\mu$m laterally away from the edge of the pattern, to avoid any influence of possible distortions around the edge on the experimental results. The position of the KPFM measurements is indicated in Fig. A.8 (a) by a red cross.

After the KPFM measurements were completed the cantilever was shifted another $\approx 50\mu$m laterally away from the edge of the pattern. Then, the tip of the cantilever was crashed into the sample. With tip and sample in contact several "tip crash images" were taken at an identical position. Additional bias pulses (10V, 5s) were applied between tip and

Figure A.7: *(a) Photograph of the CIGSe-0 sample. The surface pattern is clearly visible. (b) Magnified cut-out of (a). (c) The same surface area shown in (b), as observed through the lense-optics of the KPFM setup. The position of the KPFM cantilever is indicated by a black line.*

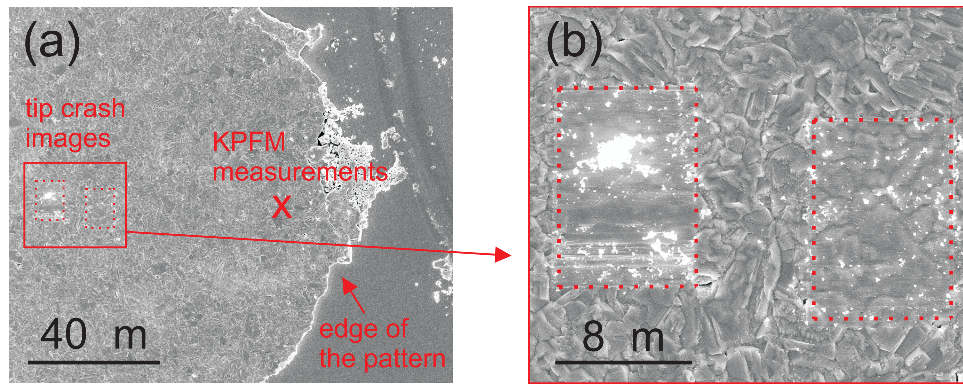

Figure A.8: *(a) SEM micrograph of the investigated surface area on the CIGSe-0 thin film (see Tab. 6.1). The positions of two different "tip crash images" are highlighted by red dashed rectangles. The position of the actual KPFM measurement is marked by a red cross. The edge of the pattern is labeled by a red arrow. (b) Magnified cut-out of from (a) with the positions of the "tip crash images" highlighted by red dashed rectangles.*

sample while the images were recorded.
By means of these tip crash images the surface structure was modified, as can be seen in Fig. A.8 (b).

Subsequent to the KPFM experiments, the CIGSe-0 sample was introduced into the SEM setup. With the help of the scratched surface pattern and the areas with modified surface structure it was possible to localize the identical position of the KPFM measurements by SEM imaging.

Both KPFM images and an SEM micrograph from the identical surface position are shown in Fig. 7.1.

List of acronyms and abbreviations

Acronyms

AFM	Atomic Force Microscopy
AM	Amplitude Modulation
BSE	Back Scattered Electrons
CIGSe	$Cu(In,Ga)Se_2$
CPD	Contact Potential Difference
CSL	Coincidence Site Lattice
DFT	Density Functional Theory
EBSD	Electron Back Scatter Diffraction
FM	Frequency Modulation
FEM	Finite Element Method
GB	Grain Boundary
HOPG	Highly Oriented Pyrolytic Graphite
KPFM	Kelvin Probe Force Microscopy
KPFS	Kelvin Probe Force Spectroscopy
nc	non contact
NPD	Nanoscale Potential Distribution
SE	Secondary Electrons
SEM	Scanning Electron Microscopy
SCR	Space Charge Region
SPM	Scanning Probe Microscopy
STM	Scanning Tunneling Microscopy
UHV	Ultra High Vacuum
XPS	X-ray Photoelectron Spectroscopy

Abbreviations

Å	[m]	unit of length; 1Å$= 1 \times 10^{-10}$m
C	[F]	capacity between cantilever and sample
d_p	[m]	spacing between atomic lattice planes
e	[As]	elemental charge; $e = 1.6022 \cdot 10^{-19}$As
$\mathbf{E}$	[V/m]	electric field intensity
E_{BSE}	[eV]	energy of backscattered electrons
E_C	[eV]	energy of the conduction band minimum
ΔE_C	[eV]	offset of the conduction band minimum
E_F	[eV]	energy of the Fermi level
E_F^{pin}	[eV]	energy of the pinned Fermi level
E_G	[eV]	band gap energy of a semiconductor
E_{ph}	[eV]	photon energy
E_{SE}	[eV]	energy of secondary electrons
E_V	[eV]	energy of the valence band maximum
ΔE_V	[eV]	offset of the valence band maximum
E_{vac}	[eV]	vacuum energy
F_{el}	[N]	electrostatic force between tip and sample
F_{ex}	[N]	external force between tip and sample
f_0	[Hz]	fundamental resonance frequency of a cantilever
f_2	[Hz]	2nd resonance frequency of a cantilever
Δf	[Hz]	frequency shift of the fundamental resonance frequency of a cantilever
ΔH	[eV]	Formation enthalpy
In_{Cu}	[-]	In-on-Cu antisite (point defect)
J_{sc}	[A/m^2]	short circuit current density
k	[N/m]	spring-constant of a cantilever
k_B	[eV/K]	Boltzmann-constant; $k_b = 8.6173 \cdot 10^{-5}$eV/K
L_{Db}	[m]	Debye-length
l	[m]	lateral location across a grain boundary
m^*	[kg]	effective mass of a cantilever
$\mathbf{n}$	[-]	normal vector
n	[-]	arbitrary integer
Na_{In}	[-]	Na on In (point defect)
Na_i	[-]	Na on Interstitial (point defect)
p_b	[bar]	base pressure
P_{GB}	[m^{-2}]	defect density at a GB
P_{net}	[m^{-3}]	net doping density

Q_{Ac}	[As/m^2]	charge per unit area accumulated in the vicinity of a pos. potential barrier
Q_{GB}	[As/m^2]	charge per unit area localized at a grain boundary
Q_{SCR}	[As/m^2]	charge per unit area localized at a space charge region
r	[m]	radius of the tip-apex
s	[eV/%]	scaling factor
T	[K]	absolute temperature
T_{Sub}	[°C]	substrate temperature
V_{ac}	[V]	ac-voltage
V_{CPD}	[V]	contact potential difference
V_{Cu}	[-]	Cu-vacancy (point defect)
V_{dc}	[V]	dc-voltage
V_{GB}	[V]	electronic potential distribution across a GB
ΔV_{GB}	[V]	electronic potential barrier at a GB
V_{oc}	[V]	open circuit voltage
V_{TS}	[V]	total potential difference between tip and sample
w	[m]	width of a nanoscale potential distribution
z_{eff}	[m]	effective tip-sample distance
z_{min}	[m]	minimum tip-sample distance
z_{rel}	[m]	relative tip-sample distance
Γ_{border}	[-]	boundary condition for the border
Γ_{sample}	[-]	boundary condition for the sample
Γ_{tip}	[-]	boundary condition for the tip
Γ_{hs}	[-]	high symmetry point
δ	[-]	absolute measurement inaccuracy
ϵ	[-]	dielectric permeability
ϵ_0	[As/Vm]	dielectric constant; $\epsilon_0 = 8.8542 \cdot 10^{-12}$As/Vm
η	[°]	Bragg angle
θ	[°]	half cone angle
λ	[m]	wave length
ρ	[As/m^3]	charge density
Φ	[eV]	absolute work function
Φ_{rel}	[eV]	relative work function (shifted with respect to the absolute work function)
$\Delta\Phi$	[eV]	work function difference
ϕ	[V]	electrostatic potential
ϕ_{sample}	[V]	electrostatic potential of the sample
ϕ_{tip}	[V]	electrostatic potential of the tip
χ	[eV]	electron affinity
ω	[rad/s]	angular frequency of an *ac*-voltage oscillation

Bibliography

[1] P. Jackson, D. Hariskos, E. Lotter, S. Paetel, R. Wuerz, R. Menner, W. Wischmann, M. Powalla, New world record efficiency for Cu(In,Ga)Se_2 thin-film solar cells beyond 20%, Prog. Photovolt: Res. Appl. 19 (2011) 894.

[2] *http://www.dresden2006.cdu.de/download/061127_parteitag_rede_merkel.pdf*.

[3] *http://www.sueddeutsche.de/politik/zitate-zur-atomdebatte-hoch-lebe-die-kernkraft-die-kernkraft-muss-weg-1.1072431*.

[4] Energiekonzept 2050-Eine Vision für ein nachhaltiges Energiekonzept auf Basis von Energieeffizienz und 100% erneuerbaren Energien, ForschungsVerbund Erneuerbare Energien (FVEE).

[5] M. A. Green, K. Emery, Y. Hishikawa, W. Warta, Solar cell efficiency tables (version 37), Prog. Photovolt: Res. Appl. 19 (1) (2011) 84.

[6] *http://www.miasole.com*.

[7] H. Leamy, G. Pike, C. Seager (Eds.), Grain Boundaries in Semiconductors, North-Holland, New York, 1982.

[8] A. P. Sutton, R. W. Balluffi, Interfaces in Crystalline Materials, Oxford University Press, USA, 1995.

[9] C. Persson, A. Zunger, Anomalous grain boundary physics in polycrystalline $CuInSe_2$: The existence of a hole barrier, Phys. Rev. Lett. 91 (26) (2003) 266401.

[10] D. Fuertes Marrón, S. Sadewasser, A. Meeder, T. Glatzel, M. C. Lux-Steiner, Electrical activity at grain boundaries of Cu(In,Ga)Se_2 thin films, Phys. Rev. B 71 (3) (2005) 033306.

[11] Y. Yan, C. S. Jiang, R. Noufi, S.-H. Wei, H. R. Moutinho, M. M. Al-Jassim, Electrically benign behavior of grain boundaries in polycrystalline $CuInSe_2$ films, Phys. Rev. Lett. 99 (23) (2007) 235504.

[12] U. Rau, K. Taretto, S. Siebentritt, Grain boundaries in Cu(In, Ga)(Se, S)2 thin-film solar cells, Appl. Phys. A 96 (1, Sp. Iss. SI) (2009) 221.

[13] M. Hafemeister, S. Siebentritt, J. Albert, M. C. Lux-Steiner, S. Sadewasser, Large neutral barrier at grain boundaries in chalcopyrite thin films, Phys. Rev. Lett. 104 (19) (2010) 196602.

[14] H. Mönig, Y. Smith, R. Caballero, C. A. Kaufmann, I. Lauermann, M. C. Lux-Steiner, S. Sadewasser, Direct evidence for a reduced density of deep level defects at grain boundaries of Cu(In, Ga)Se_2 thin films, Phys. Rev. Lett. 105 (11) (2010) 116802.

[15] L. Shay, J. Wernick, Ternary Chalcopyrite Semiconductors, Pergamon, Oxford, 1975.

[16] S. C. Abrahams, J. L. Bernstein, Piezoelectric nonlinear optic $CuGaSe_2$ and $CdGeAs_2$: Crystal structure, chalcopyrite microhardness, and sublattice distortion, J. Chem. Phys 61 (3) (1974) 1140.

[17] D. Abou-Ras, R. Caballero, C. A. Kaufmann, M. Nichterwitz, K. Sakurai, S. Schorr, T. Unold, H. W. Schock, Impact of the Ga concentration on the microstructure of $CuIn_{1-x}Ga_xSe_2$, Phys. Stat. Sol. (RRL) 2 (3) (2008) 135.

[18] C. Stephan, Structural trends in off stoichiometric chalcopyrite type compound semiconductors, Dissertation, Freie Universität Berlin (2011).

[19] J. E. Jaffe, A. Zunger, Electronic structure of the ternary chalcopyrite semiconductors $CuAlS_2$, $CuGaS_2$, $CuInS_2$, $CuAlSe_2$, $CuGaSe_2$, and $CuInSe_2$, Phys. Rev. B 28 (1983) 5822.

[20] J. E. Jaffe, A. Zunger, Anion displacements and the band-gap anomaly in ternary ABC_2 chalcopyrite semiconductors, Phys. Rev. B 27 (1983) 5176.

[21] C. Persson, Anisotropic hole-mass tensor of $CuIn_{1-x}Ga_x(S,Se)_2$: Presence of free carriers narrows the energy gap, Appl. Phys. Lett. 93 (7) (2008) 072106.

[22] J. L. Shay, B. Tell, H. M. Kasper, L. M. Schiavone, $p-d$ hybridization of the valence bands of I-III-VI_2 compounds, Phys. Rev. B 5 (1972) 5003.

[23] J. L. Shay, H. M. Kasper, Direct observation of Cu d levels in I-III-VI_2 compounds, Phys. Rev. Lett. 29 (1972) 1162.

[24] J. E. Jaffe, A. Zunger, Theory of the band-gap anomaly in ABC_2 chalcopyrite semiconductors, Phys. Rev. B 29 (1984) 1882.

[25] H. Neumann, Optical properties and electronic band structure of $CuInSe_2$, Solar Cells 16 (1986) 317 – 333.

[26] M. I. Alonso, K. Wakita, J. Pascual, M. Garriga, N. Yamamoto, Optical functions and electronic structure of $cuinse_2$, $cugase_2$, $cuins_2$, and $cugas_2$, Phys. Rev. B 63 (2001) 075203.

[27] S.-H. Wei, A. Zunger, Band offsets and optical bowings of chalcopyrites and Zn-based II-VI alloys, J. Appl. Phys. 78 (6) (1995) 3846–3856.

[28] S.-H. Wei, S. B. Zhang, A. Zunger, Effects of Ga addition to $CuInSe_2$ on its electronic, structural, and defect properties, Appl. Phys. Lett. 72 (24) (1998) 3199–3201.

[29] M. Bär, W. Bohne, J. Röhrich, E. Strub, S. Lindner, M. C. Lux-Steiner, C.-H. Fischer, T. P. Niesen, F. Karg, Determination of the band gap depth profile of the penternary $Cu(In_{(1-X)}Ga_X)(S_YSe_{(1-Y)})_2$ chalcopyrite from its composition gradient, J. App. Phys. 96 (7) (2004) 3857–3860.

[30] M. Turcu, I. M. Kötschau, U. Rau, Composition dependence of defect energies and band alignments in the $Cu(In_{1-x}Ga_x)(Se_{1-y}S_y)_2$ alloy system, J. Appl. Phys. 91 (3) (2002) 1391–1399.

[31] S. Schuler, S. Nishiwaki, J. Beckmann, N. Rega, S. Brehme, S. Siebentritt, M. C. Lux-Steiner, Charge carrier transport in polycrystalline CuGaSe2 thin films, in: Proceedings of the 29th IEEE conference, IEEE,Piscataway, 2002, p. 504.

[32] M. Gloeckler, A. J. Fahrenbruch, J. R. Sites, Numerical modeling of CIGS and CdTe solar cells: setting the baseline, Photovoltaic Energy Conversion, 2003. Proceedings of 3rd World Conference on photovoltaic energy conversion 1 (2005) 491–494.

[33] T. Eisenbarth, T. Unold, R. Caballero, C. A. Kaufmann, H.-W. Schock, Interpretation of admittance, capacitance-voltage, and current-voltage signatures in $Cu(In,Ga)Se_2$ thin film solar cells, J. App. Phys. 107 (3) (2010) 034509.

[34] S.-H. Wei, S. B. Zhang, A. Zunger, Effects of Na on the electrical and structural properties of $CuInSe_2$, J. App. Phys. 85 (10) (1999) 7214–7218.

[35] H. Möller, Structure and defect chemistry of grain boundaries in $CuInSe_2$, Solar Cells 31 (1) (1991) 77 – 100.

[36] C. Rincon, C. Bellabarba, J. Gonzalez, G. S. Perez, Optical properties and characterization of $CuInSe_2$, Solar Cells 16 (0) (1986) 335.

[37] S. B. Zhang, S.-H. Wei, A. Zunger, Stabilization of ternary compounds via ordered arrays of defect pairs, Phys. Rev. Lett. 78 (1997) 4059–4062.

[38] C. Persson, Y.-J. Zhao, S. Lany, A. Zunger, n-type doping of $CuInSe_2$ and $CuGaSe_2$, Phys. Rev. B 72 (2005) 035211.

[39] S. B. Zhang, S.-H. Wei, A. Zunger, A phenomenological model for systematization and prediction of doping limits in II–VI and I–III–VI_2compounds, J. Appl. Phys. 83 (6) (1998) 3192–3196.

[40] Y. Zhao, C. Persson, S. Lany, A. Zunger, Why can CuInSe2 be readily equilibrium-doped n-type but the wider-gap $CuGaSe_2$ cannot?, Appl. Phys. Lett. 85 (24) (2004) 5860–5862.

[41] J. E. Jaffe, A. Zunger, Defect-induced nonpolar-to-polar transition at the surface of chalcopyrite semiconductors, Phys. Rev. B 64 (2001) 241304.

[42] D. Liao, A. Rockett, Epitaxial growth of $Cu(In,Ga)Se_2$ on GaAs(110), J. App. Phys. 91 (4) (2002) 1978–1983.

[43] W. Mönch, Semiconductor Surfaces and Interfaces, Springer Series in Surface Science 26, Springer, Berlin, 1993.

[44] D. Liao, A. Rockett, Cu depletion at the $CuInSe_2$ surface, Appl. Phys. Lett. 82 (17) (2003) 2829–2831.

[45] S. Sadewasser, T. Glatzel, M. Rusu, A. Jäger-Waldau, M. C. Lux-Steiner, High-resolution work function imaging of single grains of semiconductor surfaces, Appl. Phys. Lett. 80 (16) (2002) 2979–2981.

[46] S. Theodoropoulou, D. Papadimitriou, K. Anestou, C. Cobet, N. Esser, Optical properties of CuIn $_{1-x}$ Ga$_x$ Se$_2$ quaternary alloys for solar-energy conversion, Semicond. Sci. Technol. 24 (2009) 015014.

[47] C. Kaufmann, A. Neisser, R. Klenk, R. Scheer, Transfer of $Cu(In,Ga)Se_2$ thin film solar cells to flexible substrates using an in situ process control, Thin Solid Films 480/481 (0) (2005) 515 – 519.

[48] M. Nichterwitz, private communications.

[49] T. Godecke, T. Haalboom, F. Ernst, Phase equilibria of Cu-In-SeIII. The In(2)Se(3)-Se-Cu(2)Se subsystem, Zeitschrift für Metalkunde 91 (2000) 651–662.

[50] R. A. Mickelsen, W. S. Chen, Apparatus for forming thin-film heterojunction solar cells employing materials selected from the class of I-III-VI_2 chalcopyrite compounds, US Patent 4392451 (1983).

[51] R. Klenk, T. Walter, H.-W. Schock, D. Cahen, A model for the successful growth of polycrystalline films of $CuInSe_2$ by multisource physical vacuum evaporation, Advanced Materials 5 (2) (1993) 114–119.

[52] A. M. Gabor, J. R. Tuttle, D. S. Albin, M. A. Contreras, R. Noufi, A. M. Hermann, High-efficiency $CuIn_xGa_{1-x}Se_2$ solar cells made from $(In_x,Ga_{1-x})_2Se_3$ precursor films, Appl. Phys. Lett. 65 (2) (1994) 198–200.

[53] C. A. Kaufmann, R. Caballero, T. Unold, R. Hesse, R. Klenk, S. Schorr, M. Nichterwitz, H. W. Schock, Depth profiling of Cu(In,Ga)Se_2 thin films grown at low temperatures, Solar Energy Mater. Solar Cells 93 (6-7) (2009) 859.

[54] H. Mönig, Hochenergie-Photoelektronenspektroskopie und winkelabhängige Röntgenemissionsspektroskopie zur tiefenabhängigen Untersuchung von polykristallinen Cu(In,Ga)Se_2-Schichten, Dissertation, Freie Universität Berlin (2009).

[55] R. Hesse, R. Caballero, D. Abou-Ras, T. Unold, C. A. Kaufmann, H.-W. Schock, A reliable optical method for in situ process control for deposition of Cu(In,Ga)Se_2 thin layers for photovoltaics (Proceedings Paper), SPIE: Optics+Photonics 6651 (2007).

[56] L. L. Kazmerski, O. Jamjoum, P. J. Ireland, S. K. Deb, R. A. Mickelsen, W. Chen, Initial oxidation of $CuInSe_2$, J. Vac. Sci. Technol. 19 (3) (1981) 467.

[57] U. Rau, D. Braunger, R. Herberholz, H. W. Schock, J.-F. Guillemoles, L. Kronik, D. Cahen, Oxygenation and air-annealing effects on the electronic properties of Cu(In,Ga)Se_2 films and devices, J. Appl. Phys. 86 (1) (1999) 497.

[58] J. Lehmann, Oberflächenpräparation zur Untersuchung von electrionischen Korngrenzeneigenschaften in Cu(in,Ga)Se_2, Diplomarbeit, Freie Universität Berlin (2010).

[59] D. W. Niles, K. Ramanathan, F. Hasoon, R. Noufi, B. J. Tielsch, J. E. Fulghum, Na impurity chemistry in photovoltaic CIGS thin films: Investigation with x-ray photoelectron spectroscopy, J. Vac. Sci. Technol. A 15 (6) (1997) 3044–3049.

[60] R. Hunger, T. Schulmeyer, A. Klein, W. Jaegermann, K. Sakurai, A. Yamada, P. Fons, K. Matsubara, S. Niki, An option for the surface science on Cu chalcopyrites: the selenium capping and decapping process, Surf. Sci. 557 (2004) 263 – 268.

[61] L. Weinhardt, O. Fuchs, D. Groß, E. Umbach, C. Heske, N. G. Dhere, A. A. Kadam, S. S. Kulkarni, Surface modifications of Cu(In,Ga)S_2 thin film solar cell absorbers by KCN and H_2O_2/H_2SO_4 treatments, J. App. Phys. 100 (2) (2006) 024907.

[62] R. Würz, A. Meeder, D. Fuertes Marrón, T. Schedel-Niedrig, A. Knop-Gericke, K. Lips, Native oxidation of $CuGaSe_2$ crystals and thin films studied by electron paramagnetic resonance and photoelectron spectroscopy, Phys. Rev. B 70 (2004) 205321.

[63] T. I. Kamins, Hall mobility in chemically deposited polycrystalline silicon, J. Appl. Phys. 42 (11) (1971) 4357–4365.

[64] M. E. Cowher, T. O. Sedgwick, Chemical vapor deposited polycrystalline silicon, J. Electrochem. Soc. 119 (11) (1972) 1565–1570.

[65] A. L. Fripp, L. H. Slack, Resistivity of doped polycrystalline silicon films, J. Electrochem. Soc. 120 (1) (1973) 145–146.

[66] W. Siegel, G. Kühnel, H. A. Schneider, On the determination of the carrier concentration in large-grain polycrystalline InP, GaAs, and GaP by Hall effect measurements, phys. stat. sol. (a) 87 (2) (1985) 673–681.

[67] Y. Lo, J. Hong, M. Wu, S. Wang, The transport and isolation properties of polycrystalline GaAs selectively grown by molecular beam epitaxy, Electron Device Letters, IEEE 7 (10) (1986) 586 – 588.

[68] M. K. Sharma, D. P. Joshi, Electrical conduction model for polycrystalline GaAs films, J. Appl. Phys. 102 (3) (2007) 033704.

[69] P. E. J. Flewitt, R. K. Wild, Grain Boundaries: Their microstructure and chemistry, Wiley (UK), 2001.

[70] H. Föll, Defects in crystalls, Hyperscript lecture notes, University of Kiel, Faculty of Engineering.
URL http://www.tf.uni-kiel.de/matwis/amat/def_en/index.html

[71] H. Grimmer, W. Bollmann, D. H. Warrington, Coincidence-site lattices and complete pattern-shift in cubic crystals, Acta Crystallographica Section A 30 (2) (1974) 197–207.

[72] L. K. Fionova, A. V. Artemyev, Grain boundaries in metals and semiconductors, Les editions de physique, 1993.

[73] D. Abou-Ras, K. Pantleon, The impact of twinning on the local texture of chalcopyrite-type thin films, phys. stat. sol. (RRL) 1 (5) (2007) 187–189.

[74] D. Abou-Ras, C. T. Koch, V. Kuestner, P. A. van Aken, U. Jahn, M. A. Contreras, R. Caballero, C. A. Kaufmann, R. Scheer, T. Unold, H. W. Schock, Grain-boundary types in chalcopyrite-type thin films and their correlations with film texture and electrical properties, Thin Solid Films 517 (7) (2009) 2545.

[75] Y. Yan, K. Jones, C. Jiang, X. Wu, R. Noufi, M. Al-Jassim, Understanding the defect physics in polycrystalline photovoltaic materials, Physica B: Condensed Matter 401,402 (0) (2007) 25 – 32.

[76] Y. Yan, M. M. Al-Jassim, K. M. Jones, Structure and effects of double-positioning twin boundaries in CdTe, J. Appl. Phys. 94 (5) (2003) 2976–2979.

[77] Y. Yan, M. M. Al-Jassim, K. M. Jones, Passivation of double-positioning twin boundaries in CdTe, J. Appl. Phys. 96 (1) (2004) 320–326.

[78] C. Persson, A. Zunger, Compositionally induced valence-band offset at the grain boundary of polycrystalline chalcopyrites creates a hole barrier, Appl. Phys. Lett. 87 (21) (2005) 211904.

[79] J. Seto, Electrical properties of polycrystalline silicon thin films, J. Appl. Phys. 46 (12) (1975) 5247.

[80] I. Visoly-Fisher, S. R. Cohen, D. Cahen, Direct evidence for grain-boundary depletion in polycrystalline CdTe from nanoscale-resolved measurements, Applied Physics Letters 82 (4) (2003) 556–558.

[81] I. Visoly-Fisher, S. R. Cohen, A. Ruzin, D. Cahen, How Polycrystalline Devices Can Outperform Single-Crystal Ones: Thin Film CdTe/CdS Solar Cells, Advanced Materials 16 (11) (2004) 879–883.

[82] M. J. Romero, K. Ramanathan, M. A. Contreras, M. M. Al-Jassim, R. Noufi, P. Sheldon, Cathodoluminescence of Cu(In,Ga)Se_2 thin films used in high-efficiency solar cells, Applied Physics Letters 83 (23) (2003) 4770–4772.

[83] C.-S. Jiang, R. Noufi, J. AbuShama, K. Ramanathan, H. Moutinho, J. Pankow, M. Al-Jassim, Local built-in potential on grain boundary of Cu(In,Ga)Se_2 thin films, Appl. Phys. Lett. 84 (18) (2004) 3477.

[84] C.-S. Jiang, R. Noufi, K. Ramanathan, J. AbuShama, H. Moutinho, M. Al-Jassim, Does the local built-in potential on grain boundaries of Cu(In,Ga)Se_2 thin films benefit photovoltaic performance of the device?, Appl. Phys. Lett. 85 (113) (2004) 2625.

[85] H. Föll, Semiconductors 1, Hyperscript lecture notes, University of Kiel, Faculty of Engineering.
URL http://www.tf.uni-kiel.de/matwis/amat/semi_en/index.html

[86] L. Kronik, Y. Shapira, Surface photovoltage phenomena: theory, experiment, and applications, Surf. Sci. Rep. 37 (1-5) (1999) 1.

[87] S. S. Schmidt, Microscopic properties of grain boundaries in Cu(In,Ga)Se_2 and $CuInS_2$ thin-film solar cells studied by electron microscopy, Dissertation,Technische Universität Berlin (2011).

[88] N. Syrbu, M. Bogdanash, V. Tezlevan, I. Mushcutariu, Lattice vibrations in $CuIn_{1-x}Ga_xSe_2$ crystals, Physica B: Condensed Matter 229 (2) (1997) 199 – 212.

[89] D. Azulay, O. Millo, I. Balberg, H.-W. Schock, I. Visoly-Fisher, D. Cahen, Current routes in polycrystalline $CuInSe_2$ and Cu(In,Ga)Se_2 films, Sol. Energy Mater. Sol. Cells 91 (1) (2007) 85 – 90.

[90] S. Siebentritt, M. Igalson, C. Persson, S. Lany, The electronic structure of chalcopyrites; bands, point defects and grain boundaries, Progress in Photovoltaics: Research and Applications 18 (6) (2010) 390–410.

[91] S. Siebentritt, S. Sadewasser, M. Wimmer, C. Leendertz, T. Eisenbarth, M. C. Lux-Steiner, Evidence for a neutral grain-boundary barrier in chalcopyrites, Phys. Rev. Lett. 97 (14) (2006) 146601.

[92] K. Taretto, U. Rau, J. Werner, Numerical simulation of grain boundary effects in Cu(In,Ga)Se_2 thin-film solar cells, Thin Solid Films 480-481 (2005) 8 – 12.

[93] K. Taretto, U. Rau, Can grain boundaries improve the performance of Cu(In,Ga)Se_2 solar cells?, in: Thin-film compund semiconductor photovoltaics, Vol. 1012 of Material research society symposium proceedings, Mat Res Soc, 2007, pp. 309–314.

[94] K. Taretto, U. Rau, Numerical simulation of carrier collection and recombination at grain boundaries in Cu(In,Ga)Se_2 solar cells, J. App. Phys. 103 (9) (2008) 094523.

[95] M. Gloeckler, J. R. Sites, W. K. Metzger, Grain-boundary recombination in Cu(In,Ga)Se_2 solar cells, J. App. Phys. 98 (11) (2005) 113704.

[96] W. K. Metzger, M. Gloeckler, The impact of charged grain boundaries on thin-film solar cells and characterization, J. App. Phys. 98 (6) (2005) 063701.

[97] f. Y. Yan, R. Noufi, M. M. Al-Jassim, Grain-boundary physics in polycrystalline CuInSe2 revisited: Experiment and theory, Phys. Rev. Lett. 96 (20) (2006) 205501.

[98] M. Kawamura, T. Yamada, N. Suyama, A. Yamada, M. Konagai, Grain Boundary Evaluation of Cu($In_{1-x}Ga_x$)Se_2 Solar Cells, Jpn. J. Appl. Phys. 49 (6) (2010) 062301.

[99] S. Sadewasser, D. Abou-Ras, D. Azulay, R. Baier, I. Balberg, D. Cahen, S. Cohen, K. Gartsman, K. Ganesan, J. Kavalakkatt, W. Li, O. Millo, T. Rissom, Y. Rosenwaks, H.-W. Schock, A. Schwarzman, T. Unold, Nanometer-scale electronic and microstructural properties of grain boundaries in Cu(In,Ga)Se_2, Thin Solid Films 519 (21) (2011) 7341 – 7346.

[100] S. Sadewasser, T. Glatzel, S. Schuler, S. Nishiwaki, R. Kaigawa, M. C. Lux-Steiner, Kelvin probe force microscopy for the nano scale characterization of chalcopyrite solar cell materials and devices, Thin Solid Films 431-432 (0) (2003) 257 – 261.

[101] D. Fuertes Marrón, A. Meeder, S. Sadewasser, R. Würz, C. A. Kaufmann, T. Glatzel, T. Schedel-Niedrig, M. C. Lux-Steiner, Lift-off process and rear-side characterization of $CuGaSe_2$ chalcopyrite thin films and solar cells, J. Appl. Phys. 97 (9) (2005) 094915.

[102] G. Hanna, T. Glatzel, S. Sadewasser, N. Ott, H. Strunk, U. Rau, J. Werner, Texture and electronic activity of grain boundaries in Cu(In,Ga)Se_2 thin films, Applied Physics A: Materials Science & Processing 82 (2006) 1–7.

[103] S. Sadewasser, Surface potential of chalcopyrite films measured by KPFM, Phys. Status Solidi A 203 (11) (2006) 2571.

[104] S. Sadewasser, Microscopic characterization of individual grain boundaries in Cu-III-VI_2 chalcopyrites, Thin Solid Films 515 (15) (2007) 6136 – 6141.

[105] M. Romero, C. Jiang, R. Noufi, M. Al-Jassim, Lateral electron transport in Cu(In,Ga)Se_2 investigated by electro-assisted scanning tunneling microscopy, Appl. Phys. Lett. 87 (17) (2005) 172106.

[106] G. Binnig, C. F. Quate, C. Gerber, Atomic force microscope, Phys. Rev. Lett. 56 (9) (1986) 930–933.

[107] J. M. R. Weaver, H. K. Wickramasinghe, Semiconductor characterization by scanning force microscope surface photovoltage microscopy, J. Vac. Sci. Technol. B 9 (3) (1991) 1562–1565.

[108] M. Nonnenmacher, M. Oboyle, H. Wickenramasinghe, Kelvin probe force microscopy, Appl. Phys. Lett. 58 (25) (1991) 2921–2923.

[109] A. Kikukawa, S. Hosaka, R. Imura, Vacuum compatible high-sensitive Kelvin probe force microscopy, Rev. Sci. Instrum. 67 (4) (1996) 1463–1467.

[110] S. Kitamura, K. Suzuki, M. Iwatsuki, High resolution imaging of contact potential difference using a novel ultrahigh vacuum non-contact atomic force microscope technique, Appl. Surf. Sci. 140 (3-4) (1999) 265–270.

[111] C. Sommerhalter, T. Glatzel, T. Matthes, A. Jäger-Waldau, M. Lux-Steiner, Kelvin probe force microscopy in ultra high vacuum using amplitude modulation detection of the electrostatic forces, Appl. Surf. Sci. 157 (4) (2000) 263–268.

[112] C.-S. Jiang, D. J. Friedman, J. F. Geisz, H. R. Moutinho, M. J. Romero, M. M. Al-Jassim, Distribution of built-in electrical potential in $GaInP_2$/GaAs tandem-junction solar cells, Appl. Phys. Lett. 83 (8) (2003) 1572–1574.

[113] Y. Rosenwaks, R. Shikler, T. Glatzel, S. Sadewasser, Kelvin probe force microscopy of semiconductor surface defects, Phys. Rev. B 70 (8) (2004) 085320.

[114] C. Barth, C. R. Henry, Surface double layer on (001) surfaces of alkali halide crystals: A scanning force microscopy study, Phys. Rev. Lett. 98 (13) (2007) 136804.

[115] F. Bocquet, L. Nony, C. Loppacher, T. Glatzel, Analytical approach to the local contact potential difference on (001) ionic surfaces: Implications for Kelvin probe force microscopy, Phys. Rev. B 78 (3) (2008) 035410.

[116] C. Loppacher, U. Zerweck, L. Eng, Kelvin probe force microscopy of alkali chloride thin films on Au(111), Nanotechnology 15 (2) (2004) S9–S13.

[117] H. Hoppe, T. Glatzel, M. Niggemann, A. Hinsch, M. Lux-Steiner, N. Sariciftci, Kelvin probe force microscopy study on conjugated polymer/fullerene bulk heterojunction organic solar cells, Nano Lett. 5 (2) (2005) 269–274.

[118] L. Gross, F. Mohn, N. Moll, P. Liljeroth, G. Meyer, The Chemical Structure of a Molecule Resolved by Atomic Force Microscopy, Science 325 (5944) (2009) 1110–1114.

[119] S. Sadewasser, M. C. Lux-Steiner, Local surface photovoltage spectroscopy of Cu-phthalocyanine clusters on different substrates, J. Vac. Sci. Technol. B 28 (3) (2010) C4D29–C4D33.

[120] G. Binnig, H. Rohrer, C. Gerber, E. Weibel, Tunneling through a controllable vacuum gap, Appl. Phys. Lett. 40 (2) (1982) 178–180.

[121] G. Binnig, H. Rohrer, C. Gerber, E. Weibel, Surface studies by scanning tunneling microscopy, Phys. Rev. Lett. 49 (1982) 57–61.

[122] G. Binnig, H. Rohrer, C. Gerber, E. Weibel, 7× 7 Reconstruction on Si(111) Resolved in Real Space, Phys. Rev. Lett. 50 (1983) 120–123.

[123] *http://www.nobelprize.org/nobel_prizes/physics/laureates/1986*.

[124] C. Gerber at the 14th international conference on non contact atomic force microscopy, Lindau 2011.

[125] G. Binnig, Atomic force microscope and method for imaging surfaces with atomic resolution, US Patent 4742318 (1986).

[126] G. Binnig, C. Gerber, E. Stoll, T. R. Albrecht, C. F. Quate, Atomic resolution with atomic force microscope, EPL (Europhysics Letters) 3 (12) (1987) 1281.

[127] T. R. Albrecht, C. F. Quate, Atomic resolution imaging of a nonconductor by atomic force microscopy, J. App. Phys. 62 (7) (1987) 2599–2602.

[128] Y. Martin, C. C. Williams, H. K. Wickramasinghe, Atomic force microscope-force mapping and profiling on a sub 100Å scale, J. App. Phys. 61 (10) (1987) 4723–4729.

[129] T. R. Albrecht, P. Grütter, D. Horne, D. Rugar, Frequency modulation detection using high-q cantilevers for enhanced force microscope sensitivity, J. Appl. Phys. 69 (2) (1991) 668–673.

[130] L. Gross, N. Moll, F. Mohn, A. Curioni, G. Meyer, F. Hanke, M. Persson, High-resolution molecular orbital imaging using a *p*-wave stm tip, Phys. Rev. Lett. 107 (2011) 086101.

[131] S. Sadewasser, M. C. Lux-Steiner, Correct height measurement in noncontact atomic force microscopy, Phys. Rev. Lett. 91 (26) (2003) 266101.

[132] C. Sommerhalter, T. Matthes, T. Glatzel, A. Jäger-Waldau, M. C. Lux-Steiner, High-sensitivity quantitative Kelvin probe microscopy by noncontact ultra-high-vacuum atomic force microscopy, Appl. Phys. Lett. 75 (2) (1999) 286–288.

[133] L. Kelvin, Contact electricity of metals, Phil. Mag 46 (1898) 82–120.

[134] Y. Martin, D. W. Abraham, H. K. Wickramasinghe, High-resolution capacitance measurement and potentiometry by force microscopy, Appl. Phys. Lett. 52 (13) (1988) 1103–1105.

[135] T. Glatzel, S. Sadewasser, M. Lux-Steiner, Amplitude or frequency modulation-detection in Kelvin probe force microscopy, Appl. Surf. Sci. 210 (1-2) (2003) 84–89.

[136] U. Zerweck, C. Loppacher, T. Otto, S. Grafström, L. Eng, Accuracy and resolution limits of Kelvin probe force microscopy, Phys. Rev. B 71 (12) (2005) 125424.

[137] M. McEllistrem, G. Haase, D. Chen, R. J. Hamers, Electrostatic sample-tip interactions in the scanning tunneling microscope, Phys. Rev. Lett. 70 (1993) 2471–2474.

[138] C. Sommerhalter, Kelvinsondenkraftmikroskopie im Ultrahochvakuum zur Charakterisierung von Halbleiter-Heterodioden aof Basis von Chalcopyriten, Dissertation, Freie Universität Berlin (1999).

[139] T. Glatzel, Kelvinsondenkraftmikroskopie im Ultrahochvakuum, Diplomarbeit, Freie Universität Berlin (2010).

[140] I. Horcas, R. Fernández, J. M. Gómez-Rodríguez, J. Colchero, J. Gómez-Herrero, A. M. Baro, Wsxm: A software for scanning probe microscopy and a tool for nanotechnology, Rev. Sci. Instrum. 78 (1) (2007) 013705.

[141] C. Leendertz, Simulation der Kelvinsondenkraftmikroskopie zur Quantifizierung von Messungen an Korngrenzen in $CuGaSe_2$-Bikristallen, Diplomarbeit, Freie Universität Berlin (2006).

[142] C. Leendertz, F. Streicher, M. C. Lux-Steiner, S. Sadewasser, Evaluation of Kelvin probe force microscopy for imaging grain boundaries in chalcopyrite thin films, Appl. Phys. Lett. 89 (11) (2006) 113120.

[143] L. Reimer, Scanning electron microscopy, physics of image formation and microanalysis, Springer series in optical science, Springer, 1985.

[144] D. Abou-Ras, T. Kirchartz, U. Rau (Eds.), Advanced characterization techniques for thin film solar cells, Wiley-VCH, 2011.

[145] M. Nichterwitz, Korrelation von Mikrostruktur und elektrischen Eigenschaften von $Cu(In,Ga)Se_2$-Absorberschichten in Dünnschichtsolarzellen, Diplomarbeit, Freie Universität Berlin (2008).

[146] Image provided by Daniel Abou-Ras.

[147] F. J. Giessibl, Forces and frequency shifts in atomic-resolution dynamic-force microscopy, Phys. Rev. B 56 (24) (1997) 16010–16015.

[148] H. O. Jacobs, P. Leuchtmann, O. J. Homan, A. Stemmer, Resolution and contrast in kelvin probe force microscopy, J. Appl. Phys. 84 (3) (1998) 1168–1173.

[149] S. Belaidi, F. Lebon, P. Girard, G. Leveque, S. Pagano, Finite element simulations of the resolution in electrostatic force microscopy, Applied Physics A: Materials Science & Processing 66 (1998) S239–S243.

[150] S. Sadewasser, T. Glatzel, R. Shikler, Y. Rosenwaks, M. Lux-Steiner, Resolution of Kelvin probe force microscopy in ultrahigh vacuum: comparison of experiment and simulation, Appl. Surf. Sci. 210 (2003) 32 –36.

[151] E. Palleau, L. Ressier, L. Borowik, T. Mélin, Numerical simulations for a quantitative analysis of afm electrostatic nanopatterning on pmma by kelvin force microscopy, Nanotechnology 21 (22) (2010) 225706.

[152] S. Sadewasser, C. Leendertz, F. Streicher, M. C. Lux-Steiner, The influence of surface topography on Kelvin probe force microscopy, Nanotechnology 20 (50) (2009) 505503.

[153] This method essentially takes the average of a certain number (20, in this case) of data points around each point in your data and replaces that point with the new average value (from Origin manual).

[154] An inaccurancy of 4meV was assumed for the experimental data based on the noise level, and for the simulation data the inaccurancy was estimated as 2%.

[155] M. Green, Solar cells, The University of New South Wales, Kensington, Australia, 1992.

[156] W. N. Shafarman, R. Klenk, B. E. McCandless, Device and material characterization of $Cu(InGa)Se_2$ solar cells with increasing band gap, J. Appl. Phys. 79 (9) (1996) 7324–7328.

[157] Z. Zhang, X. Tang, U. Lemmer, W. Witte, O. Kiowski, M. Powalla, H. Hölscher, Analysis of untreated cross sections of Cu(In,Ga)Se_2 thin-film solar cells with varying Ga content using Kelvin probe force microscopy, Appl. Phys. Lett. 99 (4) (2011) 042111.

[158] M. Weber, R. Scheer, H. J. Lewerenz, H. Jungblut, U. Störkel, Microroughness and Composition of Cyanide-Treated $CuInS_2$, J. Electrochem. Soc. 149 (1) (2002) G77–G84.

[159] I. Lauermann, C. Loreck, A. Grimm, R. Klenk, H. Mönig, M. Lux-Steiner, C.-H. Fischer, S. Visbeck, T. Niesen, Cu-accumulation at the interface between sputter-(Zn,Mg)O and Cu(In,Ga)$(S,Se)_2$- A key to understanding the need for buffer layers?, Thin Solid Films 515 (15) (2007) 6015 – 6019.

[160] T. Löher, W. Jaegermann, C. Pettenkofer, Formation and electronic properties of the CdS/$CuInSe_2$ (011) heterointerface studied by synchrotron-induced photoemission, J. Appl. Phys. 77 (2) (1995) 731–738.

[161] U. Fiedler, Rekombination und Diffusion in $CuGaSe_2$-Solarzellen, Dissertation, Freie Universität Berlin (2002).

[162] G. Bauer, L. Gütay, R. Kniese, Structural properties and quality of the photoexcited state in $Cu(In_{1-x}Ga_x)Se_2$ solar cell absorbers with lateral submicron resolution, Thin Solid Films 480-481 (0) (2005) 259 – 263.

[163] L. Gütay, G. Bauer, Lateral variations of optoelectronic quality of $Cu(In_{1-x}Ga_x)Se_{[2}$ in the submicron-scale, Thin Solid Films 487 (1-2) (2005) 8 – 13.

[164] C. Heske, R. Fink, E. Umbach, W. Riedl, F. Karg, Na-induced effects on the electronic structure and composition of Cu(In,Ga)Se_2 thin-film surfaces, Appl. Phys. Lett. 68 (24) (1996) 3431–3433.

[165] E. Cadel, N. Barreau, J. Kessler, P. Pareige, Atom probe study of sodium distribution in polycrystalline Cu(In,Ga)Se_2 thin film, Acta Mater. 58 (7) (2010) 2634 – 2637.

[166] D. Schmid, M. Ruckh, F. Grunwald, H. W. Schock, Chalcopyrite/defect chalcopyrite heterojunctions on the basis of $CuInSe_2$, J. App. Phys. 73 (6) (1993) 2902–2909.

[167] H. Mönig, C.-H. Fischer, A. Grimm, B. Johnson, C. A. Kaufmann, R. Caballero, I. Lauermann, M. C. Lux-Steiner, Surface Cu-depletion of Cu(In,Ga)Se_2 thin films: Further experimental evidence for a defect-induced surface reconstruction, J. App. Phys. 107 (11) (2010) 113540.

[168] M. Rusu, T. Glatzel, A. Neisser, C. Kaufmann, S. Sadewasser, M. C. Lux-Steiner, Formation of the physical vapor deposited CdS/Cu(In,Ga)Se_2 interface in highly efficient thin film solar cells, Appl. Phys. Lett. 88 (14) (2006) 143510.

[169] T. Glatzel, M. Rusu, S. Sadewasser, M. C. Lux-Steiner, Surface photovoltage analysis of thin CdS layers on polycrystalline chalcopyrite absorber layers by Kelvin probe force microscopy, Nanotechnology 19 (14) (2008) 145705.

[170] R. Baier, D. Abou-Ras, T. Rissom, M. C. Lux-Steiner, S. Sadewasser, Symmetry-dependence of electronic grain boundary properties in polycrystalline $CuInSe_2$ thin films, Appl. Phys. Lett. 99 (17) (2011) 172102.

[171] An inaccurancy of 2meV is assumed for the determination of $\Delta\Phi$ from the KPFM images.

[172] Manual of the Nanonis software.

List of publications and conferences

Publications

Parts of this thesis have already been published:

- S. Sadewasser, D. Abou-Ras, D. Azulay, R. Baier, I. Balberg, D. Cahen, S. Cohen, K. Gartsman, K. Ganesan, J. Kavalakkatt, W. Li, O. Millo, T. Rissom, Y. Rosenwaks, H.-W. Schock, A. Schwarzman, T. Unold, Nanometer-scale electronic and microstructural properties of grain boundaries in Cu(In,Ga)Se_2, Thin Solid Films 519 (2011) 7341-7346.
- R. Baier, D. Abou-Ras, T. Rissom, M. C. Lux-Steiner, S. Sadewasser, Symmetry-dependence of electronic grain boundary properties in polycrystalline $CuInSe_2$ thin films, Appl. Phys. Lett. 99 (2011) 172102.
- R. Baier, C. Leendertz, M. C. Lux-Steiner, S. Sadewasser, Toward quantitative Kelvin probe force microscopy of nanoscale potential distributions, Phys. Rev. B 85 (2012) 165436.
- R. Baier, J. Lehmann, S. Lehmann, T. Rissom, C. A. Kaufmann, A. Schwarzmann, Y. Rosenwaks, M. C. Lux-Steiner, S. Sadewasser, Electronic properties of grain boundaries in Cu(In,Ga)Se_2 thin films with various Ga-contents, Solar Energy Mater. Solar Cells 103 (2012) 86-92.

Further publications:

- Govind, R. Baier, W. Chen, H. Wang, T. E. Madey, Morphological instability of metallic surfaces: adsorbate induced nanoscale faceting, MRS Proceedings 1217 (2009) 1217-Y06-04.
- F. Mesa, G. Gordillo, Th. Dittrich, K. Ellmer, R. Baier, S. Sadewasser, Transient surface photovoltage of p-type Cu_3BiS_3, Appl. Phys. Lett. 96 (2010) 082113.
- Y. Tang, J. Chen, D. Greiner, L. Aè, R. Baier, J. Lehmann, S. Sadewasser, M. C. Lux-Steiner, Fast growth of high work function and high-quality ZnO nanorods from an aqueous solution, J. Phys. Chem. C 115 (2011) 5239-5243.
- F. Mesa, W. Chamorro, W. Vallejo, R. Baier, T. Dittrich, A. Grimm, M. C. Lux-Steiner, S. Sadewasser, Junction formation of Cu_3BiS_3 investigated by Kelvin probe force microscopy and surface photovoltage measurements, Beilstein J. Nanotechnol. 3 (2012) 277-284.

Conferences

Bold: Name of the presenter.

- **R. Baier**, J. Lehmann, S. Lehmann, T. Rissom, M. C. Lux-Steiner, S. Sadewasser, Kelvin probe force microscopy (KPFM) study of grain boundaries in polycrystalline $CuIn_{1-x}Ga_xSe_2$ thin films, European Materials Research Society (E-MRS) Spring Meeting 2010, Strasbourg, France, Poster.
- **S. Sadewasser**, D. Abou-Ras, R. Baier, C. A. Kaufmann, J. Kavalakkatt, T. Rissom, T. Unold, H.-W. Schock, Nanometer-scale electronic and microstructural properties of grain boundaries in $CuIn_{1-x}Ga_xSe_2$, European Materials Research Society (E-MRS) Spring Meeting 2010, Strasbourg, France, Talk.
- **S. Sadewasser**, S. Lehmann, P. Wagner, J. Albert, R. Baier, K. Sedlmeier, M. C. Lux-Steiner, Cu(In,Ga)Se_2 Quantum Dots: A route towards 3rd generation thin-film-based photovoltaics, 2010 Gordon Research Conference on Nanostructure Fabrication, Tilton, USA, Poster.
- **R. Baier**, C. Leendertz, M. C. Lux-Steiner, S. Sadewasser, Distance dependent Kelvin probe force spectroscopy (KPFS) of charges and dipoles at surface steps, 13th International Conference on Non-Contact Atomic Force Microscopy 2010, Kanazawa, Japan, Poster.
- **S. Sadewasser**, R. Baier, J. Lehmann, S. Lehmann, T. Rissom, M. C. Lux-Steiner, Electronic grain boundary properties of polycrystalline $CuIn_{1-x}Ga_xSe_2$ thin films studied by Kelvin probe force microscopy, 13th International Conference on Non-Contact Atomic Force Microscopy 2010, Kanazawa, Japan, Poster.
- R. Baier, S. Lehmann, **S. Sadewasser**, J. Albert, D. Marrón, M. C. Lux-Steiner, Kelvin probe force microscopy on polar CuInSe2 $112_{A,B}$ surfaces and different step edge atomic structures, 13th International Conference on Non-Contact Atomic Force Microscopy 2010, Kanazawa, Japan, Talk.
- **R. Baier**, C. Leendertz, M. C. Lux-Steiner, S. Sadewasser, Estimating absolute potential barrier dimensions at polycrystalline $CuIn_{1-x}Ga_xSe_2$ (CIGSe) grain boundaries, Materials Research Society (MRS) Spring Meeting 2011, San Francisco, USA, Poster.
- **S. Lehmann**, S. Sadewasser, J. Albert, R. Baier, D. Marrón, M. Bär, R. Wilks, C. Heske, S. Schmidt, M. C. Lux-Steiner, Tailoring the shape and surface properties of chalcopyrite nanostructures by intrinsic defect chemistry control, Materials Research Society (MRS) Spring Meeting 2011, San Francisco, USA, Poster.
- **S. Sadewasser**, R. Baier, S. Lehmann, J. Albert, C. Persson, M. C. Lux-Steiner, Kelvin probe force microscopy on polar CuInSe2 112-type surfaces and different step edge atomic structures, Materials Research Society (MRS) Spring Meeting 2011, San Francisco, USA, Poster.
- R. Baier, M. Hafemeister, S. Siebentritt, M. C. Lux-Steiner, **S. Sadewasser**, Electronic grain boundary properties of chalcopyrite solar cell materials, International

Workshop on Scanning Probe Microscopy for Energy Applications 2011, Mainz, Germany, invited Talk.

- **S. Sadewasser**, S. Lehmann, Ph. Wagner, J. Albert, R. Baier, and M. C. Lux-Steiner, Epitaxially grown CuInSe2 and CuGaSe2 quantum dots for photovoltaic applications, SemiCon2011: International Workshop on Epitaxial Growth and Fundamental Properties of Semiconductor Nanostructures, Traunkirchen, Austria, Poster.
- **R. Baier**, D. Abou-Ras, T. Rissom, M. C. Lux-Steiner, S. Sadewasser, Electronic grain boundary properties in Cu(In,Ga)Se_2 -An orientation-dependent Kelvin Probe Force Microscopy study, 14th International Conference on Non-Contact Atomic Force Microscopy 2011, Lindau, Germany, Poster.
- F. Mesa, R. Baier, Th. Dittrich, **S. Sadewasser**, M. C. Lux-Steiner, Junction formation of Cu_3BiS_3 investigated by Kelvin probe force microscopy and transient surface photovoltage, 14th International Conference on Non-Contact Atomic Force Microscopy 2011, Lindau, Germany, Poster.
- **S. Sadewasser**, R. Baier, M. Hafemeister, H. Mönig, D. Abou-Ras, M. C. Lux-Steiner, Electronic and structural grain boundary properties of chalcopyrite solar cell materials, Materials Research Society (MRS) Spring Meeting 2012, San Francisco, USA, invited Talk.

Curriculum vitae

In dieser Version der Arbeit ist aus Datenschutzgründen kein Lebenslauf enthalten.

Acknowledgments

Ein herzliches Dankeschön an:

- Prof. Dr. Martha Ch. Lux-Steiner für die Möglichkeit, in ihrem Institut zu arbeiten. Danke auch für die vielen konstruktiven Diskussionen im Rahmen der Erstbegutachtung dieser Arbeit.
- Prof. Dr. Jose Ignacio Pascual für die Übernahme der Zweitbegutachtung dieser Arbeit.
- Alle Mitglieder der Prüfungskommission.
- Sascha Sadewasser für die tolle Organisation der KPFM Gruppe und für all seine Hilfe und Unterstützung während meiner Zeit in der Gruppe.
- Alle Mitglieder der KPFM Gruppe, also Sebastian, Jürgen, Philipp, Jascha, Juliane, Sebastian, Alexander und unsere vielen Gäste. Auch wenn es uns jetzt nicht mehr gibt, wir waren schon n lustiger Haufen.
- Meine Bürokollegen, also die Jungs und Mädels aus der KPFM Gruppe, Martina und Sebastian für diverse Diskussionen und Hilfen. Und auch der Blödsinn ist nie zu kurz gekommen. Ein Hallo auch an die neuen Kameraden Simon, Marcel und Anja.
- Caspar Leendertz für all die Hilfen rund um die Simulationen.
- Christian Kaufmann, Thorsten Rissom und die ganze "Wachstumsgruppe" für die vielen Proben.
- Daniel Abou-Ras und Jürgen Albert für diverse SEM/EBSD Sessions.
- Carola Kelch für die immer wieder spontane Bereitschaft, verschiedenste Proben KCN zu ätzen.
- Alex Grimm für die XPS-Messungen, auch wenn sie es letztendlich leider nicht in die Arbeit geschafft haben.
- Alle Kollegen am HZB für die super Zeit hier. Ob Arbeit, Konferenzen, Fusi, Laufen oder Kaffee, es hat immer Spass gemacht.
- Meine Familie und alle meine Freunde.

Erklärung

Hiermit versichere ich, dass ich diese Arbeit selbständig verfasst und keine anderen als die angegebenen Hilfsmittel verwendet habe. Die Arbeit enthält, nach meinem besten Wissen und Gewissen, weder bereits von anderen Personen veröffentlichte Materialien noch wurden jegliche Teile dieser Arbeit bereits einer anderen Universität oder ähnlichen Bildungsstätte zur Erlangung eines Abschlusses oder Titels vorgelegt, außer entsprechendes Material ist als solches gekennzeichnet.

Berlin, den 8. Mai 2012.